Available on CMS information server

CMS AN-2007/026

The Compact Muon Solenoid Experiment

Analysis Note

The content of this note is intended for CMS internal use and distribution only

10 January 2008

Towards a Measurement of the Inclusive W–¿ev and Z–¿ee Cross Section in pp Collisions at sqrt(s) = 14 TeV

N. Adam, S.Baffioni, J.Berryhill, C.Charlot, G.Daskalakis, D.Evans, F.Ferri, D.Futyan, A.Ghezzi, P.Govoni, V.Halyo, J.Haupt, C.S.Hill, J.Jackson, G.Landsberg, M.Malberti, C.Marchica , P.Meridiani, D.Nguyen, I.Puljak, C.Rovelli, R.Salerno, C.Seez, T. Tabarelli de Fatis, M.Thomas, C.Timlin, P.Vanlaer, D.Wardrope

Abstract

We present methods for the measurement of the inclusive W and Z boson production cross section in the electron decay channel, based on 10pb-1 of pp collision data at sqrt(s)=14 TeV.

1 Introduction

Leptonic decays of W and Z bosons provide distinct signatures at hadron colliders [1]. Such events are expected to play a major role in the Physics commissioning of CMS [2], and in the understanding of leptons with the first data. The measurement of W and Z production cross sections is likely to be one of the first physics measurements to be made at LHC. The production cross section is high (about 190 nb for W's and 56 nb for Z's, to be multiplied by the leptonic BR's) and the measurement will be quickly dominated by systematic uncertainties. As the theoretical cross section is reasonably well predicted (with uncertainties in the range 5%–10% [3]) the measurement of the production rate ($\sigma \times \mathcal{L}$) provides an absolute measurement of the luminosity at LHC. On the other hand, an independent measurement of the luminosity (e.g., from the accelerator itself) allows the cross section to be measured, and to be compared with theory.

This Analysis Note is dedicated to the measurement of the W and γ^*/Z inclusive cross sections in the electron channel. The Note is focused on the methods to be used for an initial measurement, to be performed with the first 10 pb^{-1} collected by CMS. Data driven methods are employed with limited dependence on the simulation. Emphasis is given on methods, rather than on actual numerical values.

This Note is organized as follows: in Section 2 a brief overview of the theoretical W and Z production at the LHC is presented while Section 3 describes the formulas for the W, Z production cross section measurement. The data samples used in this Note are described in Section 4. Section 5 describes the trigger issues as well as the on-line and off-line reconstruction. The selection of the W and Z candidate events is described in Section 6. Section 7 describes the calculation of the geometric and kinematic acceptances of the candidate samples. The methods used to determine the efficiencies for identifying events within the detector acceptance are presented in Section 8. The estimation of the background contributions is discussed in Section 9. In Section 10 sources of systematic uncertainties are briefly discussed. In Section 11 the expectations for the $\mathrm{W} \to \mathrm{e}\nu$ and $\gamma^*/\mathrm{Z} \to \mathrm{e}^+\mathrm{e}^-$ cross section measurements are presented.

2 W and Z production at LHC

The dominant production mechanism for electroweak gauge bosons (W and Z) in pp collisions is the weak Drell-Yan production process [4], where a quark and an antiquark annihilate to form a vector boson.

The reaction pp→W is dominated by the annihilation of the $u\bar{d} \to W^+$ and $d\bar{u} \to W^-$ (Fig. 1) while the pp→Z (Fig. 2) is dominated by the annihilation of the $u\bar{u}, d\bar{d}$ →Z [5].

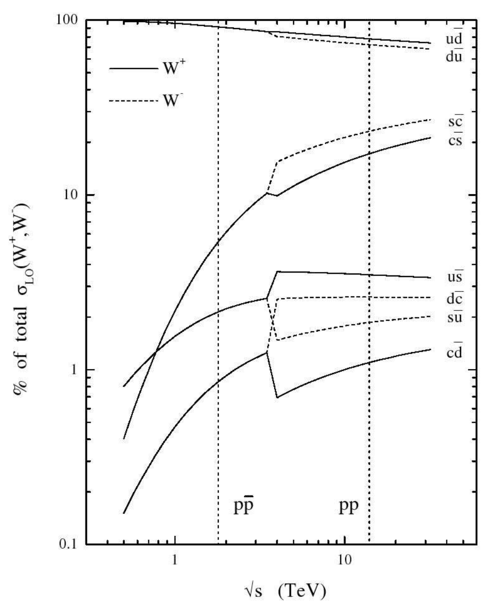

Figure 1: Parton decomposition of the W^+ and W^- total cross section in $p\bar{p}$ and pp collisions. Individual contributions are shown as a percentage of the total cross section in each case.

Calculations of the total production cross sections for W and Z bosons (Fig. 3) incorporate parton cross sections,

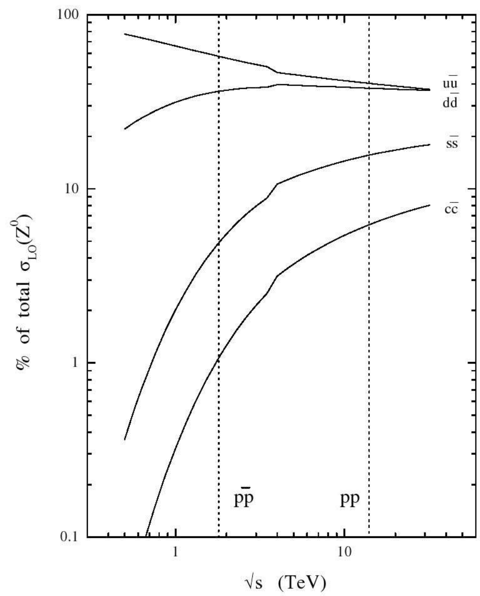

Figure 2: Parton decomposition of the Z total cross section in $p\bar{p}$ and pp collisions. Individual contributions are shown as a percentage of the total cross section in each case.

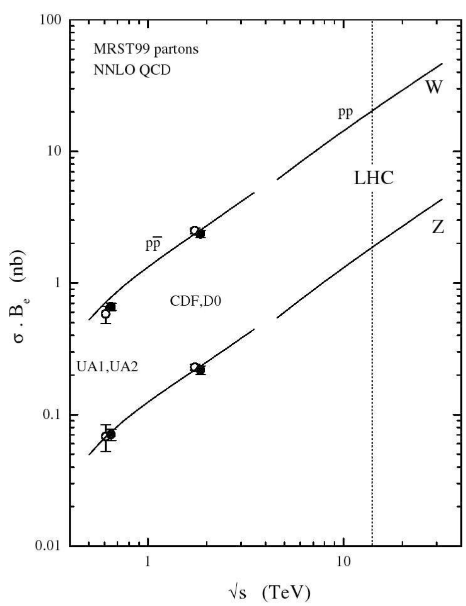

Figure 3: Prediction for the total W, Z production cross section times the leptonic branching ratio in $p\bar{p}$ and pp collisions, as a function of the collider energy $\sqrt{s}$.

parton distribution functions, higher-order QCD effects, and factors for the couplings of the different quarks and antiquarks to the W and Z bosons. Current calculations are limited by uncertainties in parton distribution functions, as well as higher-order QCD and EW radiative corrections.

The kinematic plane for LHC parton kinematics is shown in Fig. 4. The fractional momenta x_1, x_2 of the relevant partons are related to the mass ($Q^2 = M_W^2 = s \times x_1 \times x_2$) and the rapidity Y (Y = 0.5ln(x_1/x_2)) of the W and Z resonance. Thus, at central rapidity, the participating partons have small momentum fractions, x $\sim$ 0.005. Moving away from central rapidity requires one parton of lower x and one of higher x, but over the measurable rapidity range, $\mid Y \mid \leq 2.5$ (see Fig. 7, 9), x values remain in the range of $10^{-4} \leq x \leq 0.1$ [6].

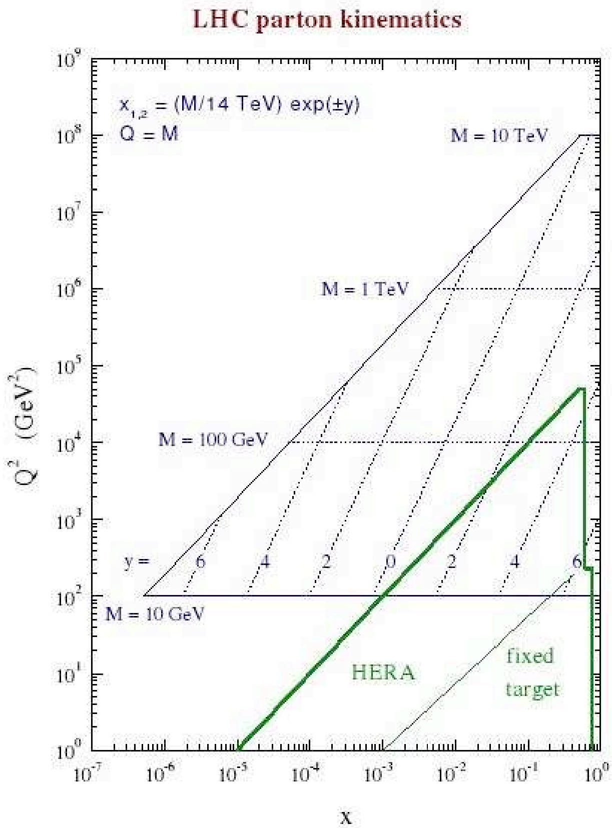

Figure 4: The LHC kinematic plane.

In contrast to the situation at the Tevatron, valence quarks are not involved much, so the scattering occurs mainly between sea quarks. Furthermore, the high scale of the process $Q^2 = M^2 \sim 10000\, GeV^2$ ensures that the gluon is the dominant parton, see Fig. 5, so that these sea quarks have mostly been generated by the flavour blind $g \rightarrow q\bar{q}$ splitting process. This means that the precision of our knowledge of W and Z cross-sections at the LHC is crucially dependent on the uncertainty on the momentum distribution of the gluon.

The predictions for the W/Z cross-sections, in the lepton decay mode, now have decreased uncertainties due to HERA data. The dramatically increased precision in the low-x gluon PDF, feeding into increased precision in the low-x sea quarks, has led to the increased precision on the predictions for W/Z production at the LHC. Theoretical calculations of the W and Z production cross sections have been carried out at next-to-leading order (NLO) and next-to-next-to-leading order (NNLO).

Fig. 6 [7] shows the CMS rapidity distribution of an on-shell Z boson at the LHC. Fig. 7 shows the geometrical acceptance of $\gamma^*/\mathrm{Z} \rightarrow \mathrm{e}^+\mathrm{e}^-$ events versus the Z rapidity. The acceptance is calculated as the fraction of the generated events in which both electrons fall within the CMS electromagnetic calorimeter fiducial region ($|\eta_{electron}|$ <2.5 with 1.4442< $|\eta_{electron}|$ <1.560 excluded). For rapidity close to zero, the acceptance is maximized but without reaching 1.0 meaning that there are some electrons expected outside the geometrical acceptance of ECAL. The acceptance drops to zero for rapidities close to 2.5.

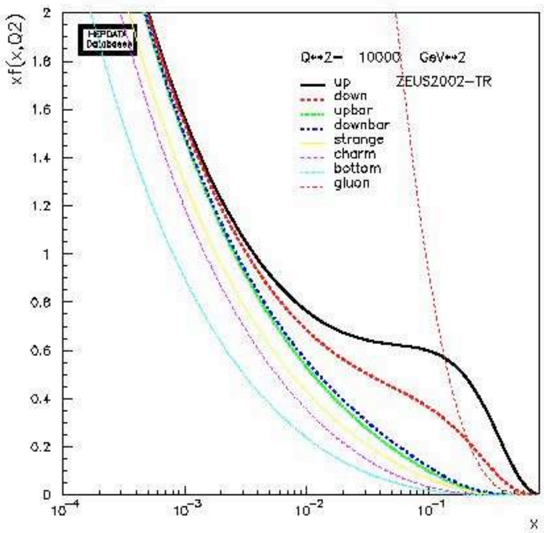

Figure 5: PDF distributions at Q^2 =10000 GeV^2.

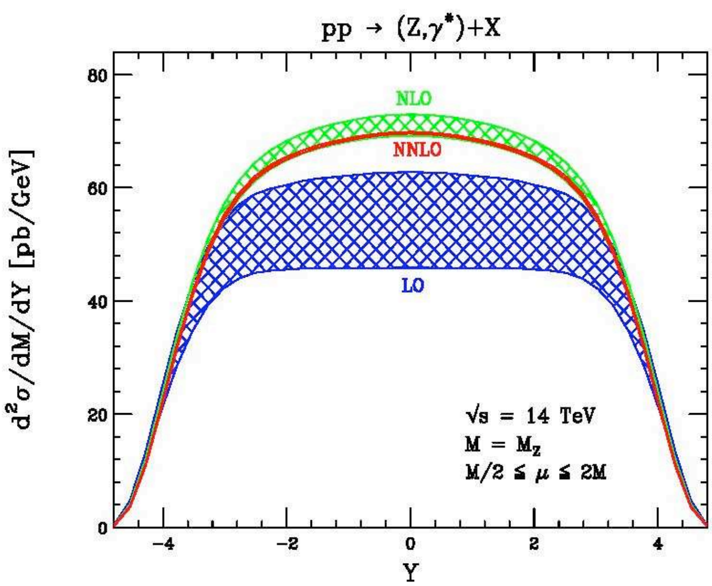

Figure 6: Rapidity distribution for $\mathrm{Z} \rightarrow \mathrm{e}^{+}\mathrm{e}^{-}$.

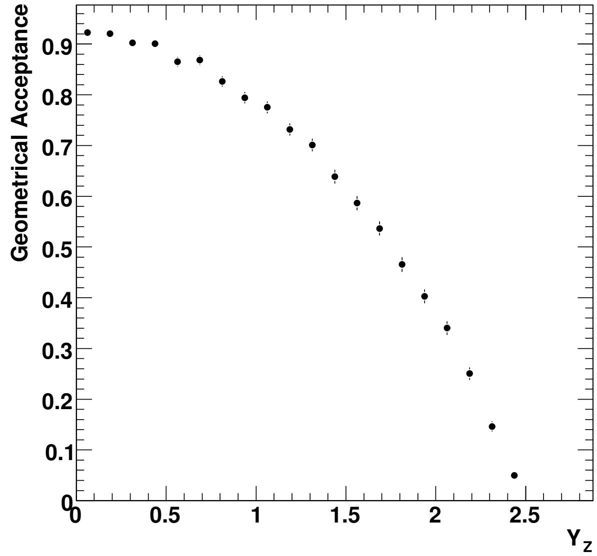

Figure 7: Geometrical acceptance for $\gamma^*/\mathrm{Z} \to \mathrm{e}^+\mathrm{e}^-$ events versus Z rapidity calculated from the fraction of the events in which both electrons fall within the CMS ECAL fiducial region.

In Fig. 8 [7] the CMS rapidity distribution of an on-shell W^- boson (left) and on-shell W^+ boson (right) at LHC can be seen. Since the distributions are symmetric in Y, only half of the distributions are shown in each case. In Fig. 9 the W^+ (black circles) and W^- (red triangles) geometrical acceptance versus the W rapidity is shown. The acceptance is calculated as the fraction of the generated W events in which the electron/positron falls within the CMS electromagnetic calorimeter fiducial region ($|\eta_{electron}|$ <2.5 with 1.4442< $|\eta_{electron}|$ <1.560 excluded). For W rapidity close to zero, the acceptance is maximized but without reaching 1.0 meaning that there are some electrons expected outside the geometrical acceptance of ECAL. The acceptance drops to zero for a $W_+(W_-)$ rapidity close to 4.5(3.5).

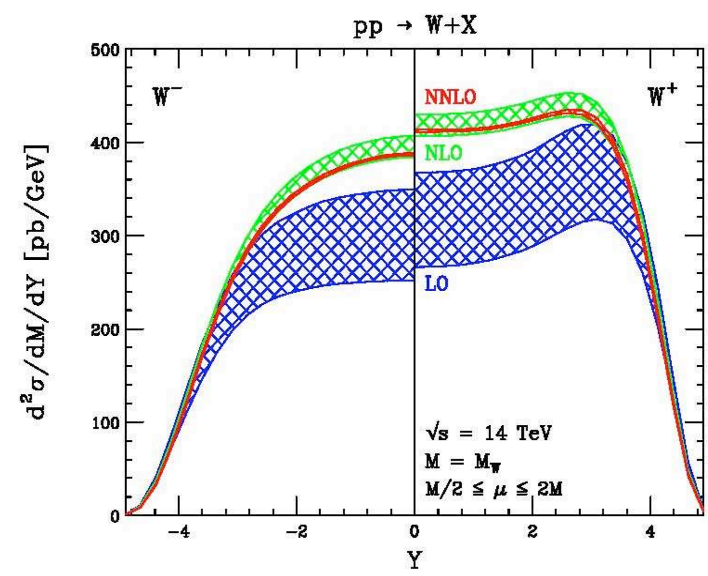

Figure 8: Rapidity distribution for W → ev.

The decay modes of the W boson are W→ $l\nu$ and W→ $q\bar{q}$ where the main modes ud, us, cs and cd have branching ratios proportional to their corresponding CKM matrix elements squared. The measured value for the branching fraction of the three leptonic modes is 10.75±0.13% (eν), 10.57±0.15% ($\mu\nu$) and 11.25±0.20% ($\tau\nu$) [8], where

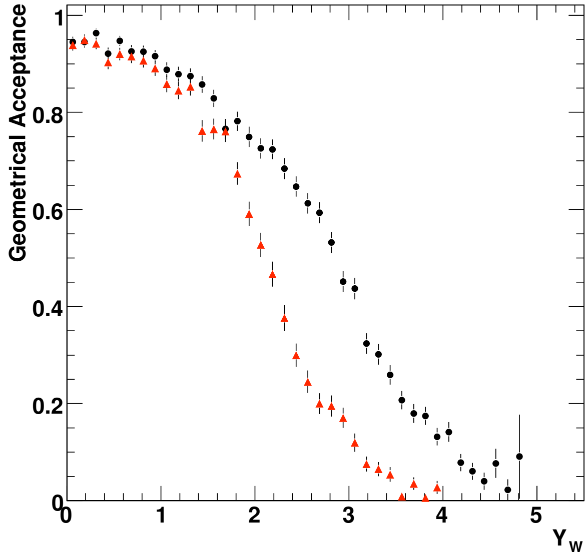

Figure 9: Geometrical acceptance for W^+ (black circles) and W^- (red triangles) versus W rapidity calculated from the ratio of the W events in which the electron/positron falls within the CMS ECAL fiducial region over all generated W events.

the remaining fraction is assigned to the hadronic decay modes.

For the Z decay modes the measured values are 3.363±0.004% (e^+e^-), 3.366±0.007% ($\mu^+\mu^-$), 3.370±0.008% ($\tau^+\tau^-$) and 20.00±0.06% (invisible) [8], where the remaining fraction is assigned to the hadronic decay modes.

3 Overview of the measurement

The signature of high transverse momentum leptons from W and Z decay is very distinctive in the environment of hadron collisions. As such, the decay of W and Z bosons into leptons provides a clean experimental measurement of their production rate. The W $\rightarrow$ ev cross section can be calculated using the following formula:

$$\sigma_W \ \times \ BR(W \rightarrow e\nu) \ = \ \frac{N_W^{pass} - N_W^{bkgd}}{A_W \ \times \ \epsilon_W \ \times \ \int Ldt} \tag{1}$$

The same formula can be used for the $\gamma^*/Z \rightarrow e^+e^-$ cross section calculation:

$$\sigma_{Z/\gamma^*} \ \times \ BR(Z/\gamma^* \rightarrow e^+e^-) \ = \ \frac{N_{Z/\gamma^*}^{pass} - N_{Z/\gamma^*}^{bkgd}}{A_{Z/\gamma^*} \ \times \ \epsilon_{Z/\gamma^*} \ \times \ \int Ldt} \tag{2}$$

where N^{pass} is the number of W $\rightarrow$ ev or $\gamma^*/Z \rightarrow e^+e^-$ candidates selected from the data. N^{bkgd} represents the expected number of background events in the W $\rightarrow$ ev or $\gamma^*/Z \rightarrow e^+e^-$ candidate samples. A_W and A_{Z/γ^*} are the acceptances for the W and Z decays defined as the fraction of these decays satisfying the geometric constraints of our detector and the kinematic constraints of the imposed selection criteria. ϵ_W and ϵ_{Z/γ^*} are the efficiencies for the identification of the W and Z decays falling within the acceptances. Finally $\int Ldt$ is the integrated luminosity of the data samples.

4 Simulated Samples

The following Standard Model data sets have been analysed: $\gamma^*/Z \rightarrow e^+e^-$, W $\rightarrow$ ev, di-jets in different $\hat{p}_t$ bins, $Z \rightarrow \tau\tau$, $t\bar{t}$, $W \rightarrow \tau\nu$ and W+jets in different $\hat{p}_t$ bins. They were produced with PYTHIA except if another generator is explicitly stated. Events were fully simulated using Geant4 and digitized without pile-up. They were reconstructed using the standard CMS reconstruction software.

In Table 1 the details for the signal and background simulated samples are collected.

Table 1: Signal and background samples

Channel	Production	Sample details	Sample size	cross section (pb)
$W \to e\nu$, PYTHIA	Spring07, CMSSW_1_3_1	$\|\eta\|$ <2.7, P_T >7.0, eff=0.6889	90000	17170 (LO)
$W^- \to e^-\nu$,MC@NLO	CSA07, CMSSW_1_6_7	$\|\eta\|$ <2.5 , eff=0.6442	39205	8395
$W^+ \to e^+\nu$,MC@NLO	CSA07, CMSSW_1_6_7	$\|\eta\|$ <2.5 , eff=0.6861	175563	11386
γ^*/Z $\to$ e$^+$e$^-$	CSA07, CMSSW_1_6_7	$M_{e,e} > 40GeV$, eff=0.648	977634	1787
$Z/\gamma^* \to \tau\tau$	CSA07, CMSSW_1_6_7	70.0< M_{Z/γ^*} <110 GeV , eff=1	109170	1586
$t\bar{t}$	Spring07/CMSSW_1_3_1	inclusive, TopRex	648918	840
$W \to \tau\nu$	CSA07, CMSSW_1_6_7	no cuts	425184	17120
$W\gamma$	CSA07, CMSSW_1_6_7	no cuts	90793	4.67
$WWee$	CSA07, CMSSW_1_6_7	no cuts	14270	1.26
WZ	CSA07, CMSSW_1_6_7	inclusive, no cuts	88000	49.9
ZZ	CSA07, CMSSW_1_6_7	inclusive, no cuts	55000	16.1
tW	CSA07, CMSSW_1_6_7	inclusive, no cuts	64000	62.0
W $\to$ ev (Trigger Tables)	RelVal CMSSW_1_6_0			
$Z \to ee$ (Trigger Tables)	RelVal CMSSW_1_6_0			
di-jet (25< $\hat{p}_t$ <50)	CSA07, CMSSW_1_6_7	em cluster E_T >15 GeV, eff=0.028	2168920	3.328E+8
di-jet (50< $\hat{p}_t$ <170)	CSA07, CMSSW_1_6_7	em cluster E_T >15 GeV, eff=0.22	1032270	2.43E+7
di-jet (170< $\hat{p}_t$)	CSA07, CMSSW_1_6_7	em cluster E_T >15 GeV, eff=0.8	342380	1.3E+5
$b\bar{b}$ (5< $\hat{p}_t$ <50)	CSA07, CMSSW_1_6_7	e P_T >5GeV , eff=0.00019	3E+6	89.5E+9
$b\bar{b}$ (50< $\hat{p}_t$ <170)	CSA07, CMSSW_1_6_7	e P_T >5GeV, eff=0.0068	3E+6	24.3E+6
$b\bar{b}$ (170< $\hat{p}_t$)	CSA07, CMSSW_1_6_7	e P_T >5GeV, eff=0.0195	2.6+6	13E+4
W+jets (0< $\hat{p}_t$ <15)	CSA07, CMSSW_1_6_7	eff = 0.1123	14886	17040
W+jets (15< $\hat{p}_t$ <20)	CSA07, CMSSW_1_6_7	eff = 1	21125	1722
W+jets (20< $\hat{p}_t$ <30)	CSA07, CMSSW_1_6_7	eff = 1	54545	1914
W+jets (30< $\hat{p}_t$ <50)	CSA07, CMSSW_1_6_7	eff = 1	54491	1541
W+jets (50< $\hat{p}_t$ <80)	CSA07, CMSSW_1_6_7	eff = 1	44537	706.2
W+jets (80< $\hat{p}_t$ <120)	CSA07, CMSSW_1_6_7	eff = 1		
W+jets (120< $\hat{p}_t$ <170)	CSA07, CMSSW_1_6_7	eff = 1	25477	70.72
W+jets (170< $\hat{p}_t$ <230)	CSA07, CMSSW_1_6_7	eff = 1	26561	20.36

For the di-jets it was required, at generator-level, that there is at least one electromagnetic cluster with E_T >15 GeV and in addition a b-flavour veto was applied. For $b\bar{b}$ was required, at generator-level, an electron with P_T >5 GeV.

For all CSA07 samples mis-calibration and mis-alignment expected for 100 pb^{-1} was applied, except the $b\bar{b}$ samples in which the applied mis-calibration and mis-alignment correspond to 10 pb^{-1}.

Some basic kinematic distributions related to the W and Z production can been seen in the following plots. Using a PYTHIA sample of W $\to$ ev events, the P_T and rapidity distributions of the W as well as the P_T, η and ϕ distributions of electrons and positrons, at generator level, can be seen in Figures 10, 11, 12 and 13. The absolute number of events is arbitrary but the relative number of electrons and positrons is the expected one.

Using the γ^*/Z $\to$ e$^+$e$^-$ sample ($M_{e,e} > 40GeV$) of Table 1, the $M_{e,e}$ is shown in Fig. 14 as well as the P_T, rapidity, η and ϕ distributions of the Z in Figures 15, 16 and 17. In Figures 18 and 19 the distributions of the P_T and η for the highest (blue line) and the lowest (red line) P_T electron are shown. For all plots, the generator level information was used.

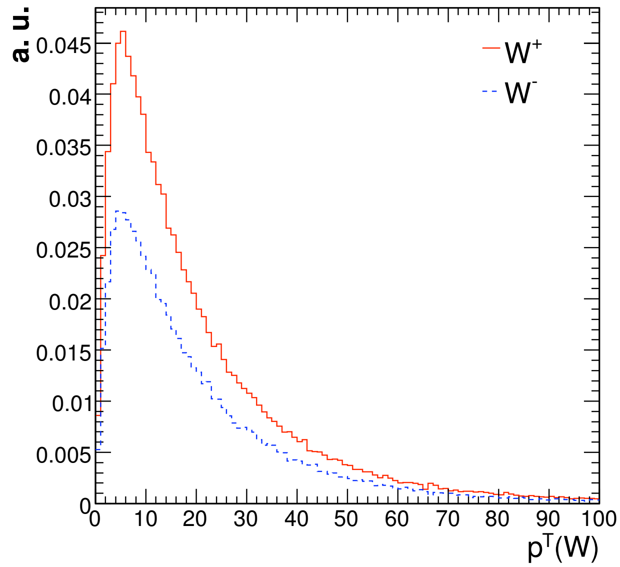

Figure 10: Distribution of W P_T, at generator level.

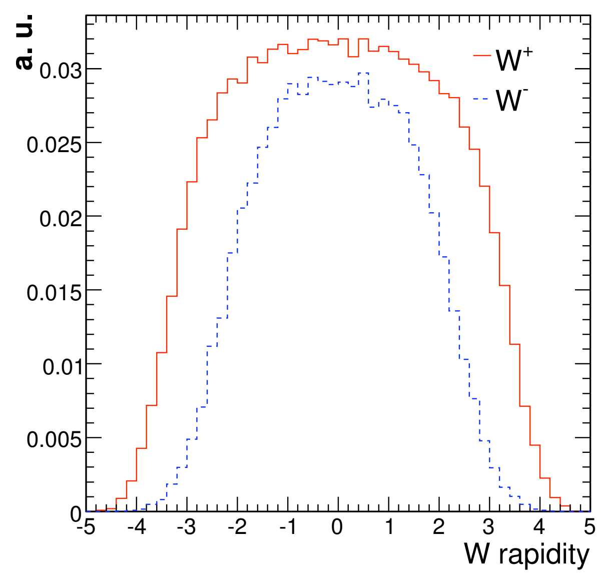

Figure 11: Distribution of W rapidity, at generator level.

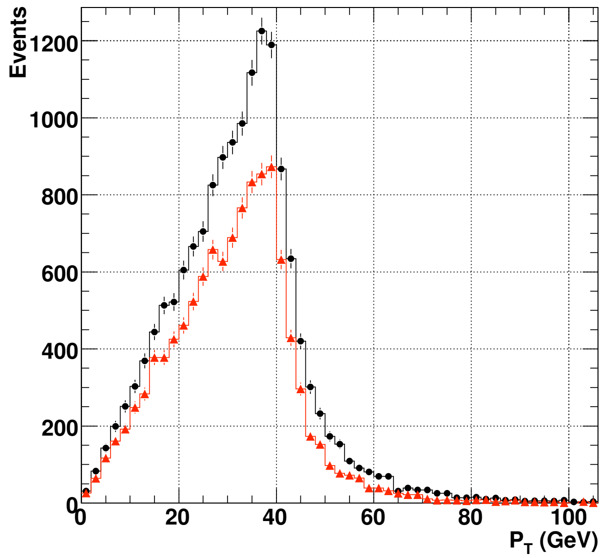

Figure 12: Distributions of electrons (red triangles) and positrons (black circles) versus their P_T, at generator level.

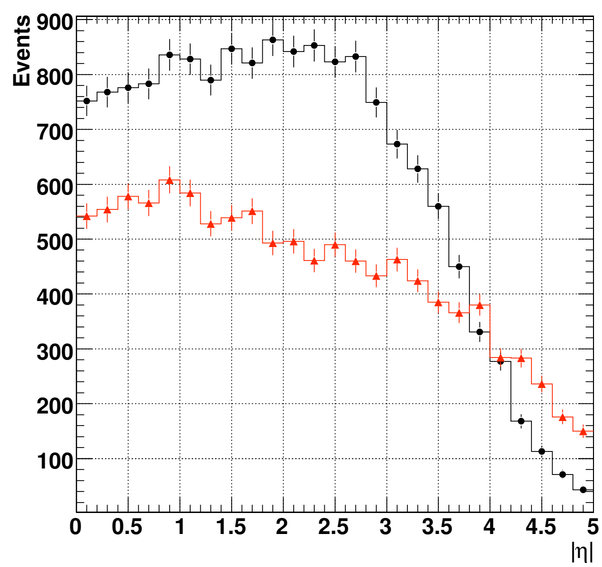

Figure 13: Distributions of electrons (red triangles) and positrons (black circles) versus their $|\eta|$, at generator level.

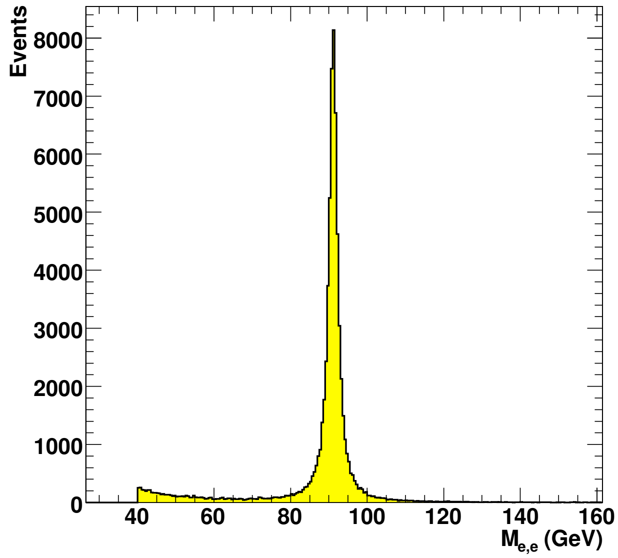

Figure 14: Distribution of $M_{e,e}$, at generator level, for events from the $\gamma^*/\mathrm{Z} \to \mathrm{e}^+\mathrm{e}^-$ ($M_{e,e} > 40GeV$) sample.

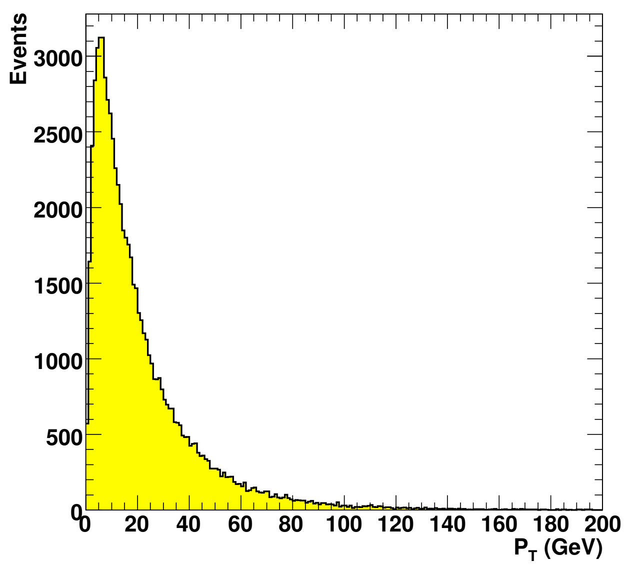

Figure 15: Distribution of Z P_T, at generator level, for events from the $\gamma^*/\mathrm{Z} \to \mathrm{e}^+\mathrm{e}^-$ ($M_{e,e} > 40GeV$) sample.

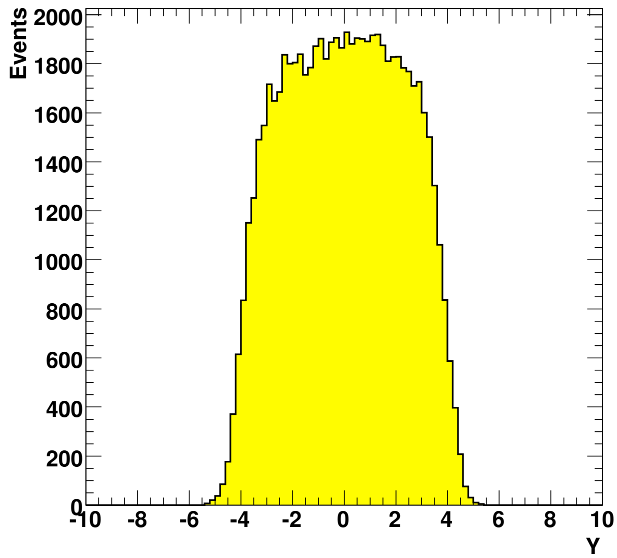

Figure 16: Distribution of Z rapidity, at generator level, for events from the $\gamma^*/\mathrm{Z} \rightarrow \mathrm{e}^+\mathrm{e}^-$ ($M_{e,e} > 40GeV$) sample.

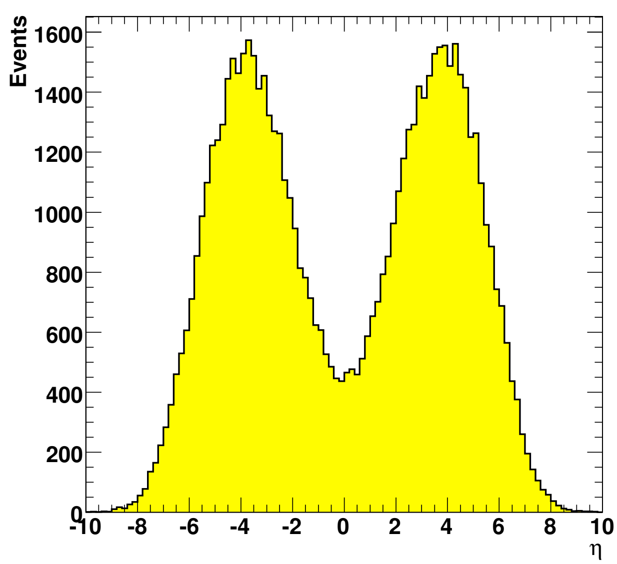

Figure 17: Distribution of Z η, at generator level, for events from the $\gamma^*/\mathrm{Z} \rightarrow \mathrm{e}^+\mathrm{e}^-$ ($M_{e,e} > 40GeV$) sample.

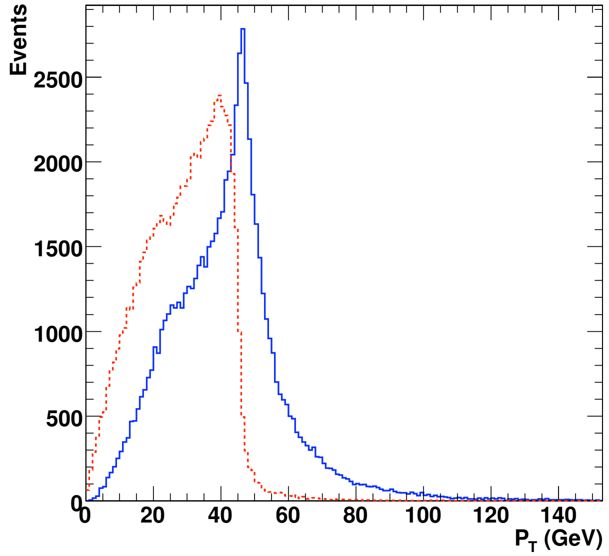

Figure 18: Distributions of P_T for the highest (blue line) and lowest (red line) P_T electrons for events from the $\gamma^*/\mathrm{Z} \rightarrow \mathrm{e}^+\mathrm{e}^-$ ($M_{e,e} > 40GeV$) sample.

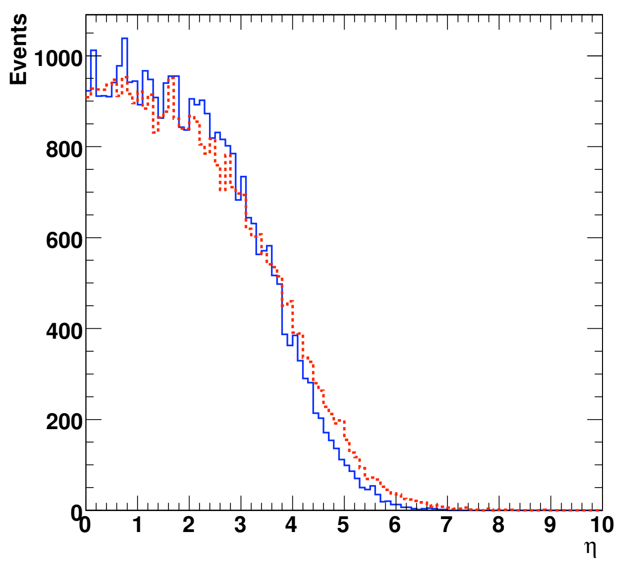

Figure 19: Distributions of $|\eta|$ for the highest (blue line) and lowest (red line) P_T electrons for events from the $\gamma^*/\mathrm{Z} \rightarrow \mathrm{e}^+\mathrm{e}^-$ ($M_{e,e} > 40GeV$) sample.

5 Detector Description / Reconstruction Issues

5.1 Online reconstruction and Trigger

The trigger system of CMS is divided into two parts: the Level-1 trigger and the High Level Trigger (HLT). The Level-1 trigger system uses custom-made hardware which analyses the detector information with a coarse granularity. The Level-1 trigger identifies different trigger objects : electrons/photons (not distinguished at that Level), jets, missing E_T and muons, and elaborates an accept/reject decision for each bunch crossing. The Level-1 electron/photon candidates can be isolated or not, according to the ECAL and HCAL energy deposition in the region around the candidate direction. For events that are accepted by the Level-1 trigger, the full detector information is available for the HLT selection process which is made on a farm of standard programmable processors. With this approach the algorithms employed for HLT selection can be complex and common to the offline reconstruction. A detailed description of the trigger system of CMS can be found in [9] and [10].

Each Level-1 trigger seeds one or several selection paths in the HLT. Currently in the HLT trigger table there are four different HLT trigger paths for the selection of electrons: the Single Isolated Electron, the Single Relaxed Electron, the Double Isolated Electron and the Double Relaxed Electron. They start from different Level-1 triggers, with the Isolated paths accepting only Level-1 isolated e/γ candidates, and the Relaxed paths accepting both Level-1 isolated and Level-1 non isolated e/γ candidates and applying the same HLT selections to both.
The details on the electron triggers are described in the 2007 HLT Exercise note [12]. The E_T thresholds for the different trigger paths are listed in Table 2, both for the Level-1 and HLT as well as the expected HLT rates for each path.

HLT path	Level-1 threshold (GeV)	HLT threshold (GeV)	HLT Rate (Hz)
Single Isolated *e*	12	15	17.1 ± 2.3
Single Relaxed *e*	15	17	9.6 ± 1.3
Double Isolated *e*	(8,8)	(10,10)	0.2 ± 0.1
Double Relaxed *e*	(10,10)	(12,12)	0.8 ± 0.1

Table 2: Level-1 and HLT E_T thresholds for the different HLT paths for electrons. Last column shows the trigger rates from the HLT exercise note [12].

The online (HLT) reconstruction of electrons follows the same schema as the offline reconstruction: as a first step an electromagnetic cluster (supercluster) is reconstructed in the electromagnetic calorimeter, then hits compatible with the supercluster are sought in the pixel detector for both charge hypotheses, and finally the full track is reconstructed starting from the hits in the pixel detector. The search regions for reconstructed hits in the pixel layers are defined along the electron trajectory, which is propagated through magnetic field from the supercluster position using its transverse momentum, as deduced from the cluster energy measured in the calorimeter and the vertex position. If the first hit is found in the innermost pixel layer within a predefined $\Delta\phi_1$ window, the second hit is required in a narrower $\Delta\phi_2$ window in the next layer.

However, given the different constraints in terms of CPU usage and prompt background rejection, some differences exist between the online and offline electron reconstruction:

- The HLT reconstruction is regional, meaning that the data unpacking and cluster reconstruction are performed only in a $\eta - \phi$ region around the electromagnetic candidates provided by the Level-1 trigger.
- While the procedure of pixel hits finding is the same for the offline and online, the search windows are different, as detailed below in the next section.
- In the online reconstruction a Kalman filter technique is used for track finding, which is faster, but less able to recognize all the hits of a radiating electron than the Gaussian Sum filter technique used in the offline reconstruction, in particular for low momentum electrons.

HCAL and track isolation criteria are applied when reconstructing the trigger electrons online in order to reduce the QCD background. For the HCAL isolation the transverse energy deposit in HCAL inside a $\eta - \phi$ cone of radius 0.15 around the supercluster direction is required to be less than a threshold that depends on the supercluster energy. For the track isolation the sum of the the p_T of the tracks in an annular $\eta - \phi$ region with $0.02 < R < 0.2$ is required to be less than a fraction of the p_T of the electron. Only the tracks with $p_T > 1.5$ GeV and with $|z_{track} - z_{electron}| < 1.0$ mm are taken into account in the sum. The thresholds applied for the isolation are less tight for the double electron paths than for the single-electron paths, as shown in table 3.

A cut on the supercluster energy divided by the track momentum ("E/p") of the electron was introduced in the single-electron path in order to select electrons with low bremsstrahlung emission. This selection has a rejection factor on the background only a little larger than on the signal (W $\rightarrow$ ev) and will be removed in the trigger paths designed for the initial low luminosity.

Isolation		Single *e*	Double Isolated *e*
HCAL	Barrel	Max(3 GeV, 0.05 E_T^{SC})	Max(9 GeV, 0.05 E_T^{SC})
HCAL	Endcap	Max(3 GeV, 0.05 E_T^{SC})	Max(9 GeV, 0.05 E_T^{SC})
Track		$\Sigma(P_T/P_T^{ele})$ <0.06	$\Sigma(P_T/P_T^{ele})$ <0.4
E/p	Barrel	1.5	-
E/p	Endcap	2.45	-

Table 3: Thresholds for the HCAL and track isolation and E/p for the single and double electron paths.

The performance of the HLT for electrons can be evaluated on fully simulated W $\rightarrow$ ev and Z $\rightarrow$ e^+e^- samples. The samples used are listed in Sec. 5 (RelVal samples from CMSSW_1_6_0), and the resulting efficiencies, both compared to generator-level and offline reconstructed electrons, are detailed below. Table 4 shows the efficiencies of the Level-1 trigger selection for W $\rightarrow$ ev and Z $\rightarrow$ e^+e^- events, after the detector acceptance cut based on generator level information, while Table 5 shows the overall efficiencies of the trigger selection for the W $\rightarrow$ ev and Z $\rightarrow$ e^+e^-samples, for events where the generator-level electrons from the W or the Z boson are matched with offline reconstructed electrons.

sample	Single Isolated *e*	Single Relaxed *e*	Double Isolated *e*	Double Relaxed *e*
$W \rightarrow e\nu$	84	87	8	7.5
$Z \rightarrow ee$	98.5	98.5	81.5	93

Table 4: Level-1 efficiency for the different HLT paths for electrons. The efficiencies are calculated on events with one (two) generator-level electron(s) with $|\eta| < 2.5$ and $p_T > 5$ GeV for the W $\rightarrow$ ev (Z $\rightarrow$ e^+e^-) sample.

sample	Single Isolated *e*	Single Relaxed *e*	Double Isolated *e*	Double Relaxed *e*
$W \rightarrow e\nu$	62	60	not considered	not considered
$Z \rightarrow ee$	89	89	71	80

Table 5: Overall efficiency (L1 $\times$ HLT) for the different HLT paths for electrons. The efficiencies are calculated on events where one (two) generator-level electron electron(s) are reconstructed offline, for the W $\rightarrow$ ev (Z $\rightarrow$ e^+e^-) sample.

5.2 Offline reconstruction

The electron momentum measurement is hampered and the electron identification made more complex, by the combined effects of the strong magnetic field and the amount of tracker material. Electrons traversing the silicon layers of the tracker radiate bremsstrahlung photons and the energy reaches the electromagnetic calorimeter (ECAL) with a significant spread in the azimuthal direction ϕ. Moreover, the bremsstrahlung emission introduces, in general, non-Gaussian contributions to the event-by-event fluctuations. Even at the intermediate P_T range of interest for W/Z, $P_T \sim M_{W,Z}/2$, this affects the electron reconstruction performance.

Using an algorithm similar to the one used at the CMS High Level Trigger (HLT), the offline electron reconstruction [11] starts with the reconstruction of superclusters in the ECAL. In contrast with the CMS HLT, a lower E_T threshold (1 GeV/c) is used to initiate cluster building together with an extended road in ϕ for a better collection of bremsstrahlung. The ECAL supercluster is used to drive the seeding of electron tracks in the tracker detector, with hits positions in the pixel layers predicted by the propagation of the energy weighted mean position of the supercluster backward through the magnetic field under both charge hypotheses. The requirements for the search of the first and second pixel hits have been loosened with respect to those of the HLT. Starting from the seed, a trajectory is created. The track building relies on the Bethe-Heitler modelling of the electron energy losses and a loose χ^2 cut is used to efficiently collect tracker hits up to the ECAL front face. A Gaussian Sum Filter (GSF) is applied for the forward and backward fits. The track momentum is taken from the most probable value of the mixture of the Gaussian distributions available for each hit position. This procedure allows efficient building of electron tracks while maintaining good momentum resolution. The relative difference between the momenta measured at both track ends, $f_{\mathrm{brem}} = (p_{\mathrm{in}} - p_{\mathrm{out}})/p_{\mathrm{in}}$ is a measure of the fraction of the electron initial energy emitted via bremsstrahlung in the tracker.

The fitted track together with the super cluster used to seed the track are then associated to form an electron if the following pre-selection requirements are satisfied:

- $0.35 < E_{\mathrm{sc}}/p_{\mathrm{in}} < 3$ $(5 \text{ in the endcaps})$, where E_{sc} is the supercluster energy and p_{in} the track momentum at the innermost track position,
- $|\Delta\eta_{\mathrm{in}}| = |\eta_{\mathrm{sc}} - \eta_{\mathrm{in}}^{\mathrm{extrap.}}| < 0.02$, where η_{sc} is the energy weighted position in η of the supercluster and $\eta_{\mathrm{in}}^{\mathrm{extrap.}}$ is the η of the track at the innermost point extrapolated to the ECAL,
- $|\Delta\phi_{\mathrm{in}}| = |\phi_{\mathrm{sc}} - \phi_{\mathrm{in}}^{\mathrm{extrap.}}| < 0.1$, where $\Delta\phi_{\mathrm{in}}$ is a similar quantity in azimuthal coordinates,
- $H/E < 0.2$, where H is the energy deposited in the HCAL towers in a cone of radius $\Delta R = 0.1$ centered on the electromagnetic super cluster position and E the energy of the electromagnetic super cluster,
- $p_T > 5$ GeV, where p_T is the track transverse momentum at the innermost track position;

The quantity f_{brem} together with other observables sensitive to the amount of bremsstrahlung radiated along the electron trajectory and to the pattern of photon emission and conversions, are used to classify electrons. Class-dependent electron energy measurement corrections are applied. The initial electron momentum direction is taken from the track. Depending on the class and on the E/p range, the ECAL corrected super cluster energy or the tracker momentum or the weighted mean of both measurements is used to estimate the initial electron momentum. Weights are evaluated using class-dependant errors available for each reconstructed electron [11].

The performances of the electron reconstruction are illustrated in Fig. 20 which presents the distribution of $E_{\mathrm{sc}}/p_{\mathrm{in}}$ for electrons from $Z \rightarrow e^+e^-$.

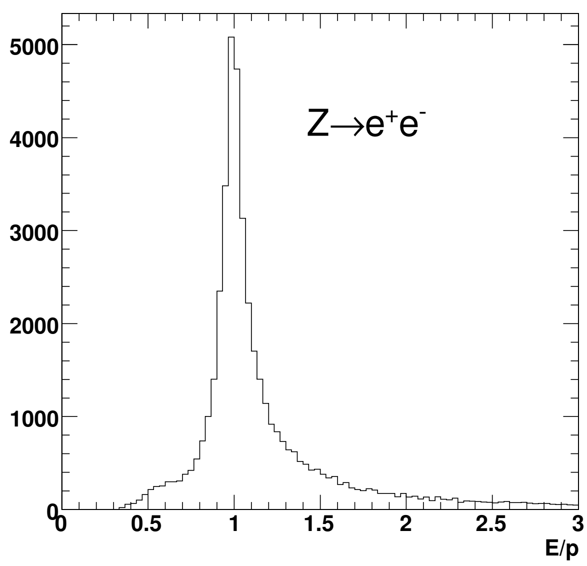

Figure 20: Distribution of $E_{\mathrm{sc}}/p_{\mathrm{in}}$ for electrons from $Z \rightarrow e^+e^-$.

6 Event Selection

6.1 Electron identification

One significant source of reducible background are events with jets, such as di-jets or W+jets where the jets are misidentified as electrons. Due to the huge cross section especially of the di-jet events, the misidentification probability must be kept as low as possible. The jet background can be discriminated by a precise matching in energy and position between the calorimeter cluster and the track and by the use of shower shape variables. Indeed, hadron showers are longer and broader, and subject to larger fluctuations, than electromagnetic showers. The bremsstrahlung, however, affects the electron identification capability. The electron shower shape, in particular in the ϕ projection, appears distorted. On the other hand, the emission of radiation in the tracker volume is a characteristic almost exclusive to electrons.

In this analysis we will use a very simple set of variables in order to perform the electron identification. Those variables are suggested by the egamma POG and are listed at Table 6. The main idea is to keep the electron efficiency high using simple selection variables that will preserve their discrimination power at the initial data collection period.

	H/E	$\sigma_{\eta\eta}$	$\Delta\phi_{in}$	$\Delta\eta_{in}$
Barrel	0.115	0.0140	0.090	0.0090
Endcap	0.150	0.0275	0.092	0.0105

Table 6: Definition of ″robust″ selection criteria.

Figures 21, 22, 23, 24 and 25 present the normalized distributions of the electron identification variables for events passing the single isolated HLT from the W $\rightarrow$ ev decay and the di-jet background. As sources of background the three di-jet samples listed in Table 1 have been considered. For both signal and backgrounds, the CMSSW_1_6_7 version of the reconstruction software was used.

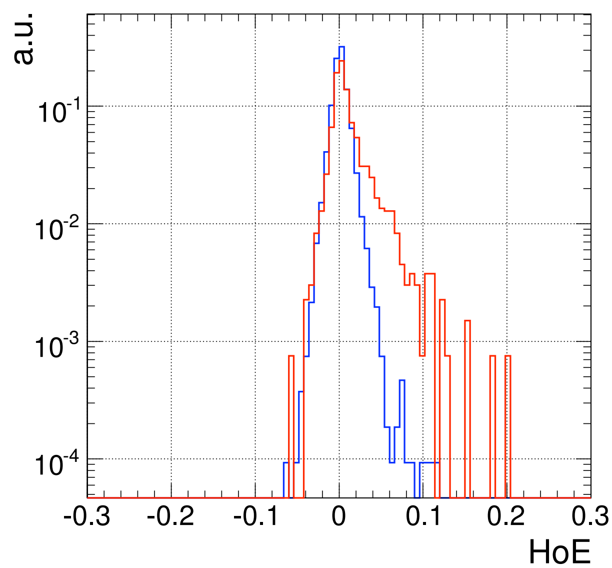

Figure 21: The H/E distribution for W $\rightarrow$ ev signal (blue line) and di-jet background (red line).

The variable H/E is the ratio of the energy deposited in the hadronic calorimeter tower behind the electromagnetic seed cluster over the energy of the electromagnetic seed cluster. The shape variable $\sigma_{\eta\eta}$ is defined as an energy weighted average of the η dispersion of the seed cluster crystals around the most energetic one. The $\Delta\phi_{in}$ and $\Delta\eta_{in}$ variables are related to the geometrical matching between the GSF track and ECAL supercluster (see Section 5.2).

As can be seen from the plots the proposed cut values listed in Table 6 are loose and further optimization might be possible.

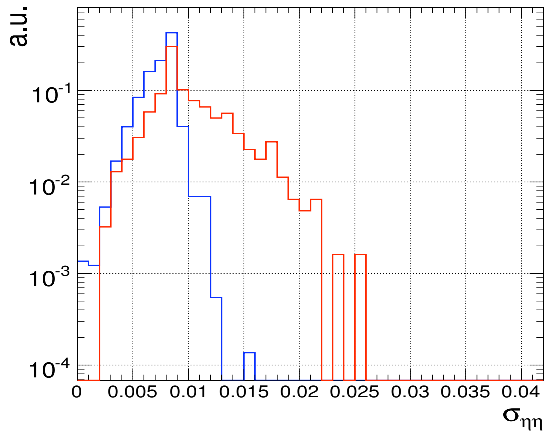

Figure 22: The $\sigma_{\eta\eta}$ distribution for electrons in the ECAL Barrel for the W $\rightarrow$ ev signal (blue line) and the di-jet background (red line).

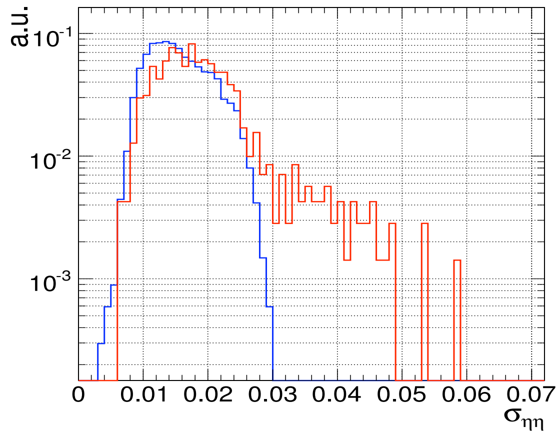

Figure 23: The $\sigma_{\eta\eta}$ distribution for electrons in the ECAL Endcaps for the W $\rightarrow$ ev signal (blue line) and the di-jet background (red line).

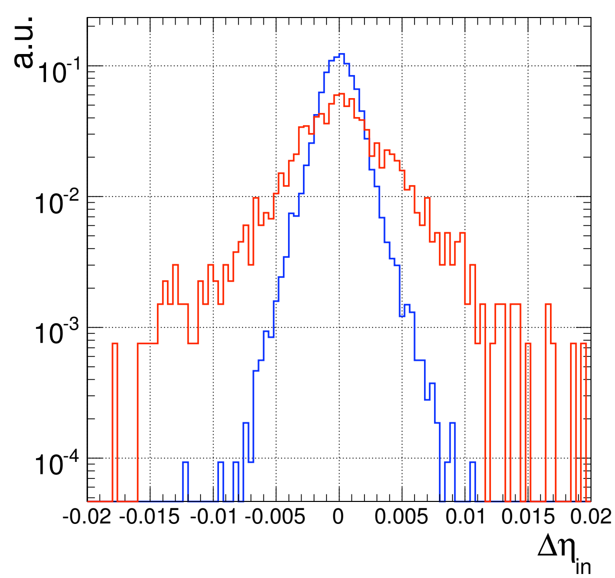

Figure 24: The $\Delta\eta_{in}$ distribution for W $\rightarrow$ ev signal (blue line) and di-jet background (red line).

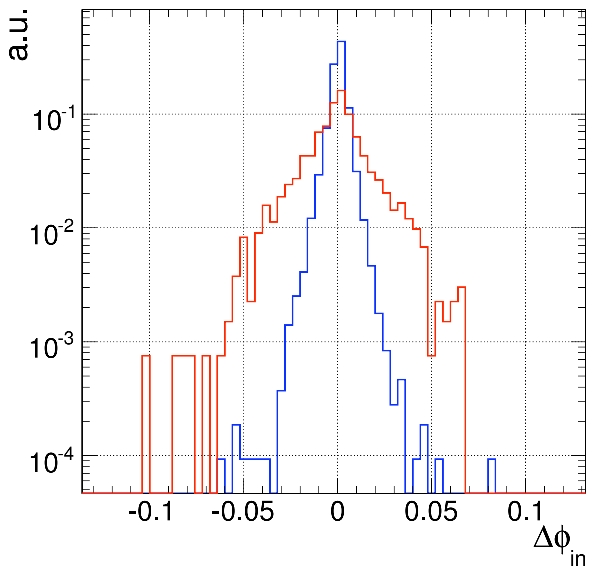

Figure 25: The $\Delta\phi_{in}$ distribution for W $\rightarrow$ ev signal (blue line) and di-jet background (red line).

6.2 $\not\!\!E_T$ reconstruction and selection

In this section we discuss various aspects of calculation and utilization of missing transverse energy ($\not\!\!E_T$) in the event, which is indicative of the presence of a neutrino in the $W \rightarrow e\nu$ decay. For more detailed studies of the $\not\!\!E_T$ performance, see Ref. [13].

The Missing Transverse Energy ($\not\!\!E_T$) is determined in the recent versions of the CMS software framework, CMSSW, as the magnitude of the transverse vector sum over energy deposits in uncorrected, projective Calorimeter Towers:

$$\vec{\not\!\!E_T} = -\sum_{\mathbf{n}}(\mathbf{E_n}\sin\theta_{\mathbf{n}}\cos\phi_{\mathbf{n}}\hat{\mathbf{i}} + \mathbf{E_n}\sin\theta_{\mathbf{n}}\sin\phi_{\mathbf{n}}\hat{\mathbf{j}}) = \not\!\!E_x\hat{\mathbf{i}} + \not\!\!E_y\hat{\mathbf{j}} \tag{3}$$

where the index n runs over all calorimeter input objects (e.g. energy deposits in towers, reconstructed hits, or generator-level particle energies). Here $\hat{\mathbf{i}}$, $\hat{\mathbf{j}}$ are the unit vectors in the direction of the x and y axis of the CMS right-handed coordinate system, where z is pointed in the direction of the beam, and x is horizontal. Note that in the absence of $\not\!\!E_T$ from physics sources in the event, $\not\!\!E_x$ and $\not\!\!E_y$ are expected to be distributed as Gaussians with the mean of zero and the standard deviation of σ, while $\not\!\!E_T$ (equation 3) has a more complicated shape described by $\frac{\sqrt{2\pi}}{\sigma}\theta(\not\!\!E_T)\not\!\!E_T \times G(\not\!\!E_T, 0, \sigma)$, where $\theta(x)$ is the θ function (i.e., 1 for $x \geq 0$ and 0 otherwise), $G(x, \mu, \sigma) = \exp(-(x-\mu)^2/2\sigma^2)/\sqrt{2\pi}\sigma$ is a Gaussian with the mean μ and standard deviation of σ. Note that σ in the Gaussian describing $\not\!\!E_T$ is the same as the standard deviation in the $\not\!\!E_T$ projection on an arbitrary axis.

$$\sigma(\not\!\!E_T) = A \oplus B\sqrt{\Sigma E_T - D} \oplus C\,(\Sigma E_T - D). \tag{4}$$

Here the A (“noise”) term represents effects due to electronic noise, pile-up, and underlying event; the B (“stochastic”) term represents the statistical sampling nature of the Calorimeter Towers; the C (“constant”) term represents residual systematic effects due to non-linearities, cracks, and dead material in the detector; and the D (“offset”) term accounts the effect of noise on $\sum E_T$. It is important to emphasize that the above parametrisation factorizes the $\not\!\!E_T$ uncertainty into independent effects A, B, C. In particular, the stochastic and constant terms do not depend on the effects due to noise, pile-up, and underlying event (to first order).

From the fits to a large QCD sample generated and reconstructed with CMSSW 1_5_2, we find the values of the parameters A, B, C, S_T^0, listed in Table 7. The $\not\!\!E_T$ resolution as a function of $\sum E_T$ is shown in Fig. 26.

There are important $\not\!\!E_T$corrections for events with large $\not\!\!E_T$(see Ref. [13]). In the case of the inclusive W production, the average $\not\!\!E_T$ is only about 40 GeV, and thus the bias in its reconstruction is small. Moreover, derivation of reliable $\not\!\!E_T$corrections from data would take some time, so they may not be available in the early data. Consequently, it has been decided not to apply any corrections to the $\not\!\!E_T$ for the purpose of this analysis.

Table 7: $\not\!\!E_T$ resolution parameters; see Eq. (4) and text for details.

A	B	C	D
1.48 ± 0.29 GeV	$1.03 \pm 0.03\ \sqrt{\text{GeV}}$	0.023 ± 0.002	82 ± 4 GeV

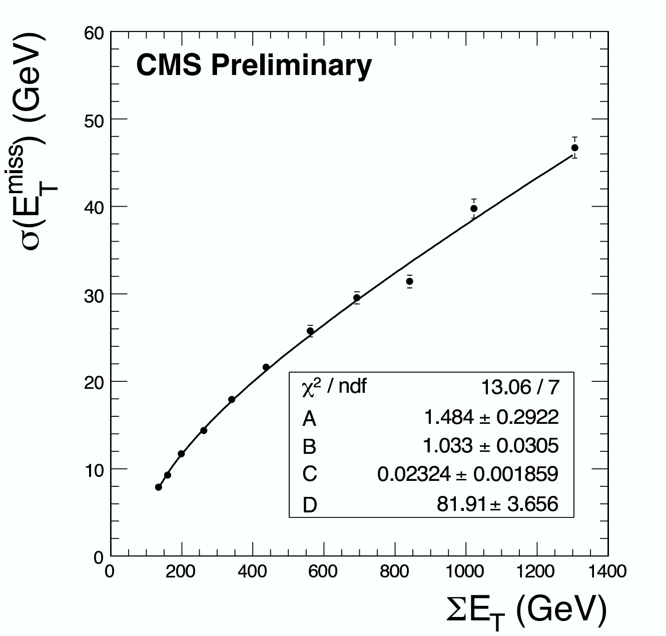

Figure 26: $\not\!\!E_T$ resolution as a function of $\sum E_T$. The line indicates the fit to the resolution function given by Eq. (4) with the parameters listed in Table 7.

6.3 $\mathrm{W} \to \mathrm{e}\nu$ selection

The $\mathrm{W} \to \mathrm{e}\nu$ events are selected from events that pass the single isolated-electron High Level Trigger. We require a high-P_T electron formed from the association of a high E_T ECAL supercluster and a high P_T GSF track in the Tracker. Since the electrons from the W decays are isolated, we demand very low track activity around the electron candidate. This criterion rejects quite efficiently electrons from jets. The isolation is defined as :

$$\sum_{track} \left(\frac{p_T^{track}}{p_T^{ele}} \right)^2 < 0.02$$

where all CTF tracks with $p_T^{track} > 1.5\,GeV$, within an $\eta - \phi$ annular isolation cone centred on the reconstructed electron are summed. The cone has limits, $0.02 < \Delta R < 0.6$ ($\Delta R = \sqrt{(\Delta\eta)^2 + (\Delta\phi)^2}$). The p_T^{ele} is the momentum of the reconstructed electron at the vertex.

An additional criterion that could help in background rejection would be to apply a vertex compatibility requirement on the tracks. It would be particularly helpful in rejecting jets from secondary vertices like b-jets and electrons from converted photons. So, a transverse impact point cut is expected to improve the selection and will be included in future studies.

Since the semileptonic W decay gives an undetectable neutrino, the W candidate events should show an imbalance of the measured momentum. Since the colliding partons have an overall $P_T \simeq 0$, we identify the missing transverse energy in the event with the neutrino P_T.

The following selection has been used for the $W \to e\nu$ cross section analysis:

- event passes the single isolated electron HLT

- PixelMatchGsfElectron in ECAL fiducial ($|\eta|$ <2.5 with 1.4442< $|\eta|$ <1.560 excluded)
- PixelMatchGsfElectron supercluster E_T > 20.0 GeV
- electron is isolated (track isolation)
- electron passes Electron ID criteria as defined in Table 6
- $\not{E}_T$> 20.0 GeV

This selection is not optimized yet due to the very late arrival of important backgrounds like the di-jets. It serves as a reference to future studies which will provide an optimized and robust selection, appropriate for the early data taking period of LHC.

The efficiencies of the selection criteria on a signal sample can be found in Table 8. For the correct interpretation of the numbers it must be taken into account that the selection was applied on a fully simulated W $\rightarrow$ ev sample without pile-up. A preselection at generation level was applied by demanding the generated electron from the W decay to have $|\eta_{electron}|$ <2.5 .

In Fig. 27 and Fig. 28 the electron supercluster E_T and the isolation variable are shown for the W $\rightarrow$ ev signal and the di-jet background. As can be seen, optimization of the E_T and isolation cuts (for the moment 20.0 GeV and 0.02 respectively) could improve the purity of the signal.

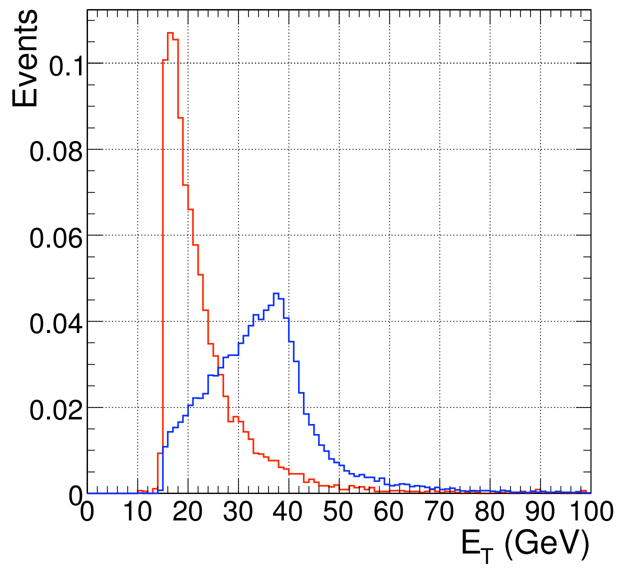

Figure 27: The supercluster E_T distribution for W $\rightarrow$ ev signal (blue line) and di-jet background (red line).

Table 8: Signal Selection for $W \rightarrow e\nu$

Selection Criterion	Efficiency for $W^+ \rightarrow e^+\nu$	Efficiency for $W^- \rightarrow e^-\nu$
single isolated electron HLT	56.7	60.2
PixelMatchGsfElectron, E_T >20.0 GeV ,in fiducial	88.3	91.4
isolated (track isolation)	97.8	98.0
passes ID criteria as defined in Table 6	99.9	99.9
$\not{E}_T$> 20.0 GeV	91.5	93.0

6.4 $\mathrm{Z} \rightarrow \mathrm{e}^+\mathrm{e}^-$ selection

The $\mathrm{Z} \rightarrow \mathrm{e}^+\mathrm{e}^-$ events are selected from events that pass the single isolated-electron High Level Trigger. We require two high-P_T electrons formed from the association of high E_T ECAL superclusters with high P_T GSF

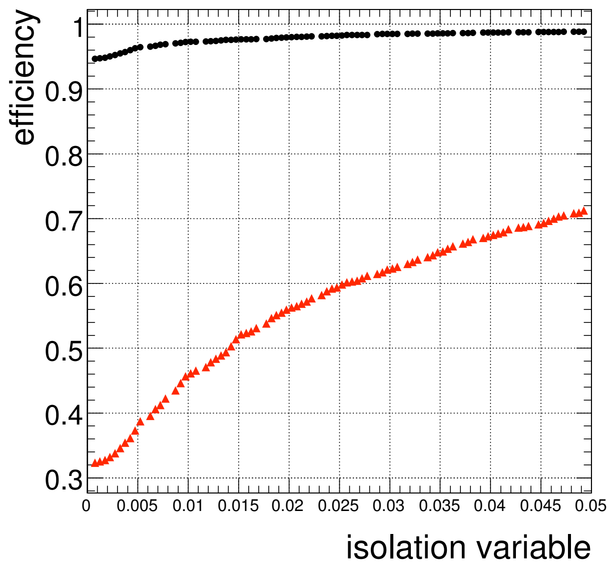

Figure 28: The isolation variable distribution for W $\rightarrow$ ev signal (blue line) and di-jet background (red line).

tracks in the Tracker. As in the W case, electrons from the Z decay are isolated, so we demand very low track activity around each electron candidate. This criterion rejects quite efficiently electrons from jets. Also, the invariant mass of the two electrons should lie between 70 and 110 GeV. Additional criteria that help in background rejection are the opposite sign charge and the common z-vertex of the electrons.

The following signal selection has been used for the Z $\rightarrow$ e$^+$e$^-$ cross section analysis:

- event passes the single isolated electron HLT
- two PixelMatchGsfElectrons in ECAL fiducial ($|\eta|$ <2.5 with 1.4442< $|\eta|$ <1.560 excluded)
- two PixelMatchGsfElectrons with supercluster E_T >20.0 GeV
- both electrons are isolated
- both electrons pass ID criteria as defined in Table 6
- 70< $M_{e,e}$ <110 GeV

As in the W $\rightarrow$ ev case, this selection was not optimized. In the future an optimization study must be performed in order to investigate if the background contamination permits further relaxation of some of the selection criteria.

The efficiencies of the basic selection stated above for a signal sample can be found in Table 9. For the correct interpretation of the numbers it must be taken into account that the selection was applied on a fully simulated $\gamma^*/$Z $\rightarrow$ e$^+$e$^-$ sample without pile-up in which events were preselected demanding $M_{\gamma^*/Z}$ >40 GeV.

Table 9: Signal Selection for $\gamma^*/$Z $\rightarrow$ e$^+$e$^-$

Selection Criterion	Efficiency
single isolated electron HLT	68.6
two PixelMatchGsfElectrons, E_T >20.0 GeV, in fiducial	59.5
both isolated (track isolation)	88.4
both pass electron ID defined in Table 6	99.1
70< $M_{e,e}$ <110 GeV	94.4

7 Acceptance

Since the data itself is inherently biased with respect to geometric acceptance, this quantity must be measured from Monte Carlo simulation. We also use Monte Carlo simulation to calculate the kinematic acceptance for electrons from $\mathrm{Z} \to \mathrm{e}^+\mathrm{e}^-$, and $\mathrm{W} \to \mathrm{e}\nu$ to have an $E_T > 20$ GeV.

7.1 Acceptance for $\gamma^*/\mathrm{Z} \to \mathrm{e}^+\mathrm{e}^-$ events

We compute a combined geometric and kinematic acceptance for $\gamma^*/\mathrm{Z} \to \mathrm{e}^+\mathrm{e}^-$ events which have both superclusters (matched to MC electrons) in the ECAL fiducial area ($|\eta|$ <2.5, 1.4442< $|\eta|$ <1.560 excluded) with $E_T > 20$ GeV and 70< $M_{e,e}$ <110GeV, divided by all simulated $\gamma^*/\mathrm{Z} \to \mathrm{e}^+\mathrm{e}^-$ events. We calculate separately the acceptances for the cases that both electrons are in the ECAL Barrel (EB,EB), both in the ECAL Endcaps (EE,EE) and one electron is in the Barrel and the other in the Endcaps (EB,EE).

The combined geometric and kinematic acceptance calculated from 70,000 simulated $\gamma^*/\mathrm{Z} \to \mathrm{e}^+\mathrm{e}^-$ events is (errors are statistical):

$$\mathcal{A}_{\mathcal{EB},\mathcal{EB}} = \frac{N_{ee}^{acc}}{N_{ee}^{tot}} = 0.1626 \pm 0.0014$$

$$\mathcal{A}_{\mathcal{EB},\mathcal{EE}} = \frac{N_{ee}^{acc}}{N_{ee}^{tot}} = 0.1197 \pm 0.0012$$

$$\mathcal{A}_{\mathcal{EE},\mathcal{EE}} = \frac{N_{ee}^{acc}}{N_{ee}^{tot}} = 0.0415 \pm 0.0008$$

So the total acceptance is:

$$\mathcal{A}_{\mathcal{TOT}} = \mathcal{A}_{\mathcal{EB},\mathcal{EB}} + \mathcal{A}_{\mathcal{EB},\mathcal{EE}} + \mathcal{A}_{\mathcal{EE},\mathcal{EE}} = 0.3239 \pm 0.0018$$

This acceptance is normalized to $\gamma^*/\mathrm{Z} \to \mathrm{e}^+\mathrm{e}^-$ events with $M_{\gamma^*/\mathrm{Z} \to \mathrm{e}^+\mathrm{e}^-}$ >40.0 GeV, generated with PYTHIA.

7.2 Acceptance for $\mathrm{W} \to \mathrm{e}\nu$ events

We compute a combined geometric and kinematic acceptance for $\mathrm{W} \to \mathrm{e}\nu$ events which have their supercluster (matched to a MC electron) in the ECAL fiducial area ($|\eta|$ <2.5, 1.4442< $|\eta|$ <1.560 excluded) with $E_T > 20$ GeV, divided by all simulated $\mathrm{W} \to \mathrm{e}\nu$ events. We also calculate separately the acceptance for the ECAL Barrel (EB) and the ECAL Endcaps (EE).

The combined EB geometric and kinematic acceptance that we calculate from 40,000 simulated $\mathrm{W} \to \mathrm{e}\nu$ events is (error are statistical):

$$\mathcal{A}_{\mathcal{EB}} = \frac{N_{e\nu}^{acc}}{N_{e\nu}^{tot}} = 0.4787 \pm 0.0026$$

The combined EE geometric and kinematic acceptance that we calculate from 40,000 simulated $\mathrm{W} \to \mathrm{e}\nu$ events is:

$$\mathcal{A}_{\mathcal{EE}} = \frac{N_{e\nu}^{acc}}{N_{e\nu}^{tot}} = 0.3037 \pm 0.0026$$

The total acceptance is:

$$\mathcal{A}_{\mathcal{TOT}} = \mathcal{A}_{\mathcal{EB}} + \mathcal{A}_{\mathcal{EE}} = 0.7824 \pm 0.0023$$

The acceptances are normalized to $\mathrm{W} \to \mathrm{e}\nu$ events generated with MC@NLO demanding the electron from the W decay to have $|\eta| < 2.5$.

7.3 Systematic Uncertainties on the Acceptance determination

Systematic errors in the determination of the geometric and kinematic acceptance arise from uncertainties in the Monte Carlo simulation used to do the calculation. Some of the most important of these are listed below:

- choice of generator - how accurately does it calculate differential cross-sections, e.g. $d\sigma/dY$ or $d\sigma/dp_T$ of the W and Z
- renormalization scale
- choice of pdf - this will also effect the rapidity distribution
- accuracy of material description in CMS simulation
- energy/momentum scale/resolution

In Section 10.1 we discuss with more details the choice of the generator, the dependencies on the renormalization scales and the choice of the pdf and we compare the Z p_T distributions from different generators. For the other possible sources of uncertainties listed above (material description and energy/momentum scale/resolution), we have not estimated their effect at this time.

8 Efficiency

In this section we will briefly discuss how we will measure from data the efficiencies for the selection criteria used in the measurement of the W and Z cross sections. For the measurement of those efficiencies the Tag and Probe method could be used. This method is already explored in CMS [14] and results from this reference will be used in our study.

8.1 Efficiency with Tag and Probe method

As can be seen from Tables 8 and 9, the selection we used in this study is based on PixelMatchGsfElectrons that pass the single isolated electron HLT, are isolated and pass electron identification criteria. As we already mentioned these selection criteria might not be optimal for the cross section measurement but will be used to demonstrate how to measure the W and Z cross sections by measuring all related selection efficiencies from data.

The method that we employ has been called the "Tag and Probe" method. This method, which has been successfully used in some form or another by both Tevatron experiments [15][16], relies upon $Z \rightarrow e^+e^-$ decays to provide an unbiased, high-purity, electron sample with which to measure the efficiency of a particular cut or trigger. In this method, a single electron trigger sample is used, from which a subset of di-electron events are selected. One of the electrons, the "tag", is required to pass stringent electron identification criteria whilst the other electron, the "probe", is only required to pass a set of identification criteria depending on the efficiency under study. The invariant mass of the tag and probe electron candidates are required to be within a window around M_Z. The tight criteria imposed on the tag coupled with the invariant mass requirement is sufficient to ensure high electron purity.

Even though the tag+invariant mass requirement generally provides a high purity di-electron sample, there will inevitably be some residual background contamination due to W+jets and/or QCD events where one or more electron has been misidentified. Methods for estimating these backgrounds have been developed and the procedure for correcting our efficiency measurements due to their presence is applied to every efficiency used in this study.

We choose to factorize the total efficiency as follows:

$$\varepsilon_{total} = \varepsilon_{offline} \times \varepsilon_{online} \tag{5}$$

We further factorize both the offline efficiency and the online efficiency:

$$\varepsilon_{offline} = \epsilon_{\text{preselection}} \times \epsilon_{\text{isolation}} \times \epsilon_{\text{elID}} \tag{6}$$

$$\varepsilon_{online} = \varepsilon_{L1} \times \varepsilon_{HLT} \tag{7}$$

where each efficiency "factor" is defined as follows:

- $\epsilon_{preselection}$ ≡ the efficiency of the preselection for PixelMatchGsfElectron objects formed from a supercluster and a GsfTrack given that a supercluster of a certain E_T has been reconstructed in the ECAL.

- $\epsilon_{isolation}$ ≡ the efficiency for the GsfElectron to be isolated. The isolation referred to here is a track isolation.

- ϵ_{elID} ≡ the efficiency for an isolated GsfElectron to pass additional electron identification criteria.

- $\varepsilon_{\mathrm{L1+HLT}}$ ≡ the efficiency to pass the HLT used in the analysis including the fact that the probe considered must have been able to pass the L1 trigger seeding that HLT.

The factorization of the offline efficiency represents the subsequent steps in the reconstruction/identification of a particle as an electron and follows the selection steps presented in Tables 8 and 9.

Correlations between the various efficiencies are taken into account by calculating the efficiency of each requirement in a specific order. The probe used to measure a specific efficiency must satisfy the selection requirements of all previous steps. In the chosen factorization scheme, online trigger efficiencies are measured with respect to the offline selection. Data taking is triggered on a single electron trigger stream and the tag electron is required to satisfy the requirements of this trigger. The order of the factorisation of efficiencies should not have an effect on the final overall efficiency measured. This is already proved in [14].

In the following figures we present the efficiencies for the different selection criteria versus the electron supercluster E_T, η, ϕ and primary vertex z-position. In Appendix D we present these efficiencies in tables of E_T, η bins.

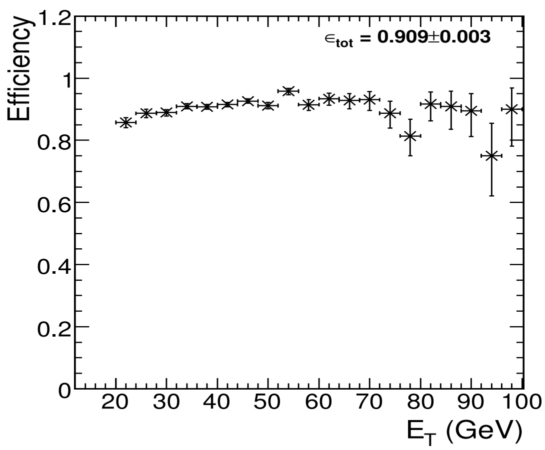

Figure 29: PixelMatchGsfElectron preselection efficiency versus supercluster E_T.

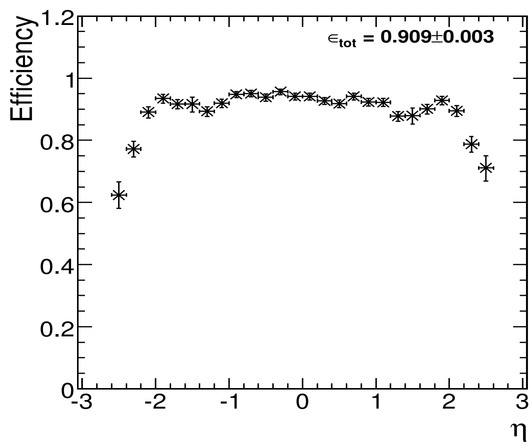

Figure 30: PixelMatchGsfElectron preselection efficiency versus supercluster η.

9 Backgrounds

Backgrounds for electroweak boson production arise from two kinds of sources: isolated leptons originating from other electroweak boson production processes, and leptons (real or misidentified) originating from QCD jet production. The former source can be reliably estimated from simulation; the latter cannot, and must be estimated via empirical methods.

9.1 Electroweak backgrounds to $\mathrm{W} \to \mathrm{e}\nu$ events

The electroweak background in the W sample consists mostly of $\gamma^*/\mathrm{Z} \to \mathrm{e}^+\mathrm{e}^-$ events with one electron escaping detection (3% of signal), and W and Z decays to τ's followed by a τ decay to an electron (2% of signal). The $\gamma^*/\mathrm{Z} \to \mathrm{e}^+\mathrm{e}^-$ background is suppressed due to the hermetic ECAL and HCAL coverage; the τ background is suppressed because the lepton spectrum is somewhat softer than direct decay to e's. Other processes have been evaluated ($W\gamma$, WW, WZ, ZZ, tW) and found to be negligible. Since these backgrounds are small, and because they arise from reliably computable electroweak cross sections, they can be estimated with adequate precision from simulation.

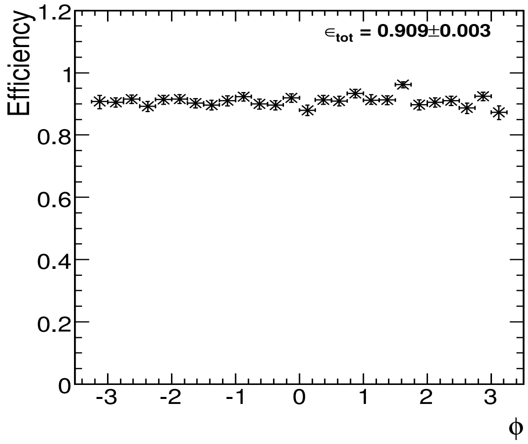

Figure 31: PixelMatchGsfElectron preselection efficiency versus supercluster ϕ

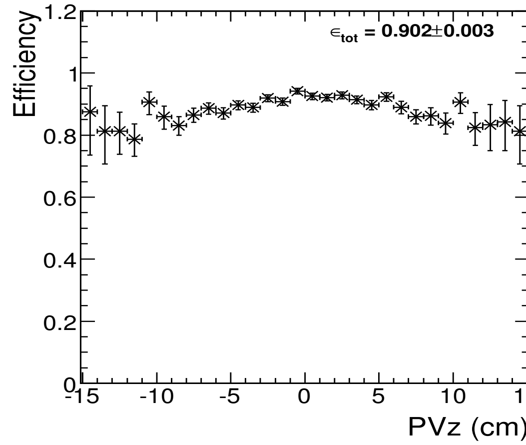

Figure 32: PixelMatchGsfElectron preselection efficiency versus vertex z-position.

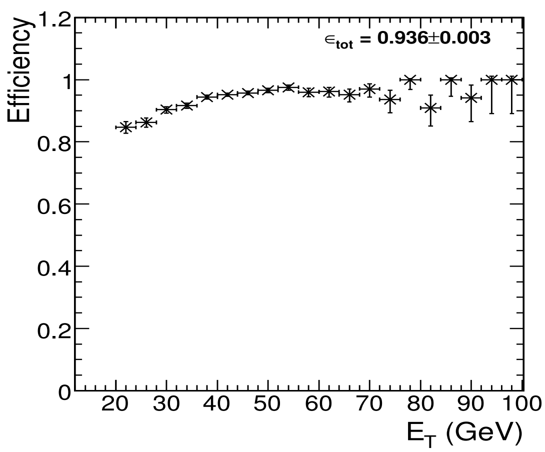

Figure 33: Isolation efficiency versus supercluster E_T.

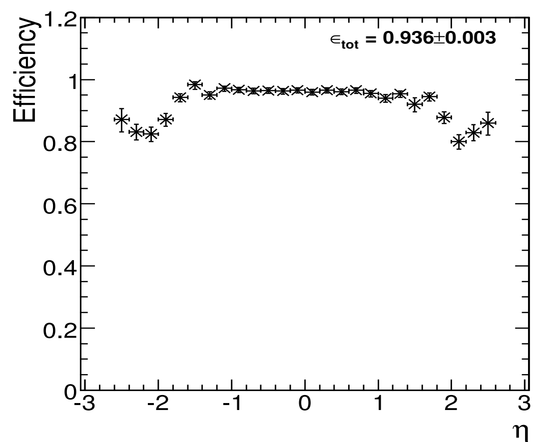

Figure 34: Isolation efficiency versus supercluster η.

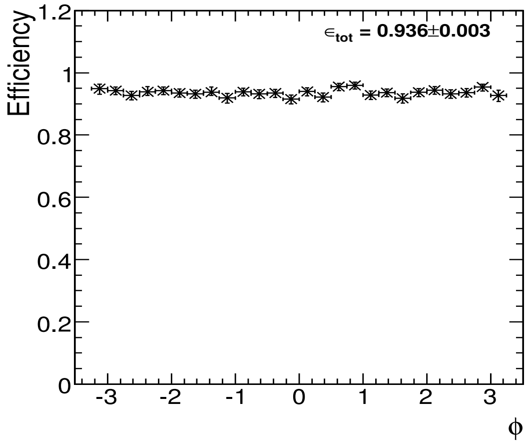

Figure 35: Isolation efficiency versus supercluster ϕ

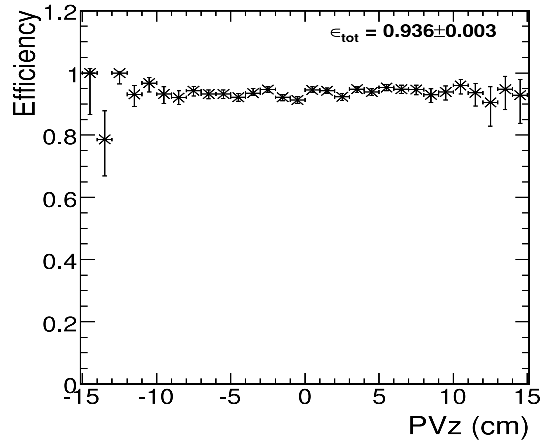

Figure 36: Isolation efficiency versus vertex z-position.

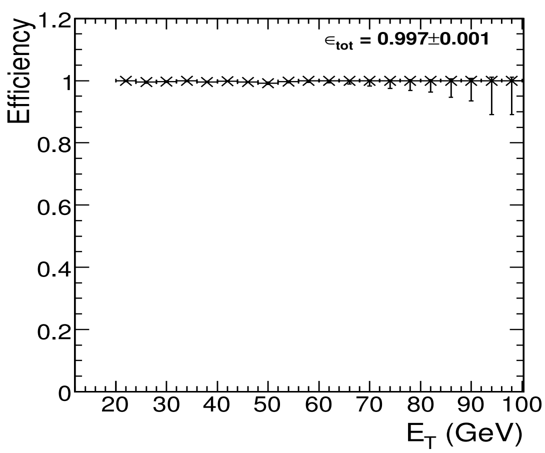

Figure 37: "Robust" electron identification efficiency versus supercluster E_T.

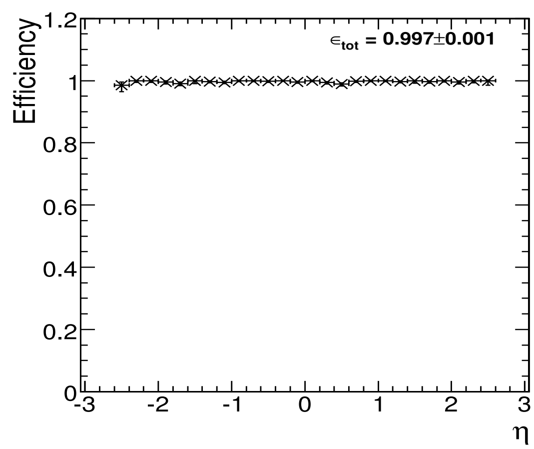

Figure 38: "Robust" electron identification efficiency versus supercluster η.

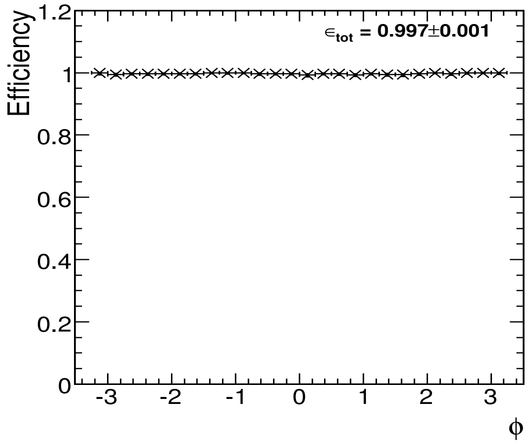

Figure 39: “Robust” electron identification efficiency versus supercluster ϕ

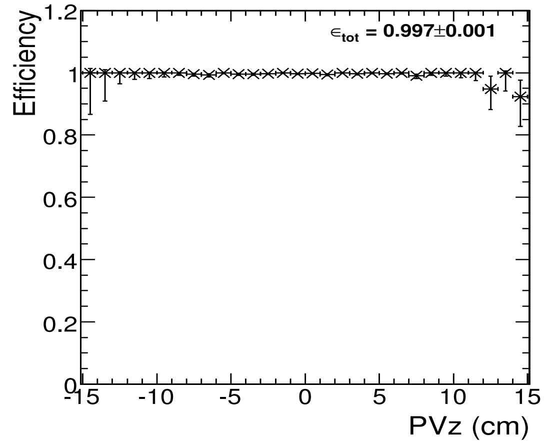

Figure 40: “Robust” electron identification efficiency versus vertex z-position.

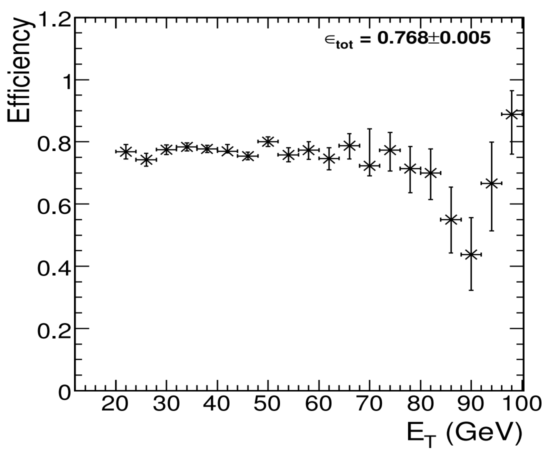

Figure 41: L1+HLT efficiency versus supercluster E_T.

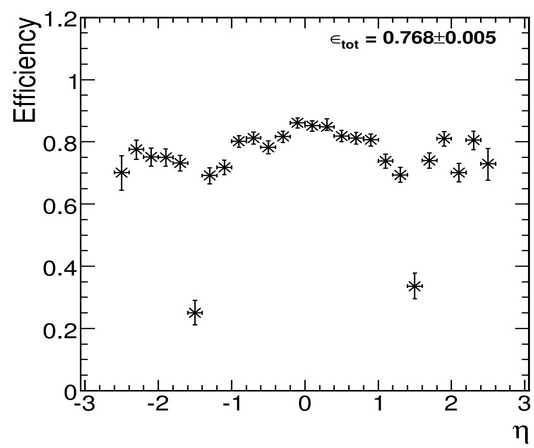

Figure 42: L1+HLT efficiency versus supercluster η.

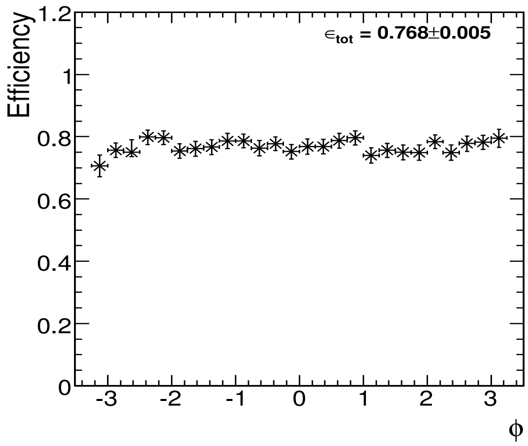

Figure 43: L1+HLT efficiency versus supercluster ϕ

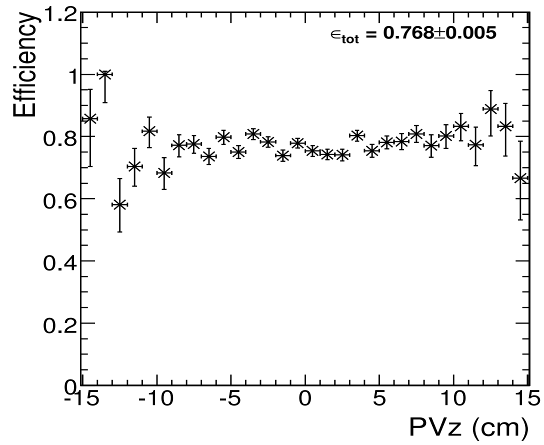

Figure 44: L1+HLT efficiency versus vertex z-position.

In Tables 10, 11 and 12 the number of events passing each selection step is shown. As can be seen the contamination of the $\mathrm{W} \rightarrow \mathrm{ev}$ from $W \rightarrow \tau\nu$, $\gamma^*/\mathrm{Z} \rightarrow \mathrm{e}^+\mathrm{e}^-$, $\gamma/Z \rightarrow \tau\tau$ and $t\bar{t}$ is at the level of 6%.

Table 10: Signal and Backgrounds for the $W \rightarrow e\nu$ selection

Selection Criterion	$W^+ \rightarrow e^+\nu$	$W^- \rightarrow e^-\nu$	$W \rightarrow \tau\nu$	$\gamma^*/\mathrm{Z} \rightarrow \mathrm{e}^+\mathrm{e}^-$
unweighted number of events	175563	39205	425184	18182
cross section (pb)	11386	8395	17120	1787
preselection Efficiency	0.6861	0.6442	1	0.648
event weight for 10 pb^{-1}	0.445	1.379	0.403	0.637
weighted number of events	78119	54081	171200	11580
single isolated electron HLT	44321	32550	3830	7939
PixelMatchGsfElectron, E_T >20.0 GeV, in fiducial	39140	29736	2332	7543
isolated (track isolation)	38266	29148	2181	7366
electron pass ID defined in Table 6	38248	29121	2107	7354
$\not{E}_T$> 20.0 GeV	34977	27085	1426	1610

9.2 Hadronic backgrounds to $\mathrm{W} \rightarrow \mathrm{ev}$ events

A contribution to the background can also be expected from dijet events, in which one jet is misidentified as an electron and the other is mismeasured, creating missing transverse energy. This background needs to be controlled carefully, as the uncertainty associated to it is larger than for the electroweak backgrounds mentioned above.

Different types of hadronic background include electron candidates arising from heavy flavor quarks, and candidates from lighter partons. Simulation studies of them have been performed separately.

In Table 13 the number of light flavor di-jet events passing each selection step is shown while in Table 14 the contamination from the $b\bar{b}$ is shown. The $b\bar{b}$ background can be reduced with an additional requirement for the electrons to have a small transverse impact parameter value. This cut was not applied in this analysis but it will be studied in the future.

The $\not{E}_T$ distribution for the $\mathrm{W} \rightarrow \mathrm{ev}$ signal and the most important backgrounds ($b\bar{b}$ in not included yet) can be seen in Figure 45.

Table 11: Signal and Backgrounds for the $W \to e\nu$ selection

Selection Criterion	$\gamma/Z \to \tau\tau$	$t\bar{t}$
unweighted number of events	482292	648918
cross section (pb)	1586	840
preselection Efficiency	1	1
event weight for 10 pb^{-1}	3.289E-2	1.295E-2
weighted number of events	15860	8400
single isolated electron HLT	872	993
PixelMatchGsfElectron, E_T >20.0 GeV, in fiducial	580	765
isolated (track isolation)	541	658
electron pass ID defined in Table 6	524	654
$\not{E}_T$> 20.0 GeV	193	581

Table 12: Signal and Backgrounds for the $W \to e\nu$ selection

Selection Criterion	Wγ	WWee	WZ	ZZ	tW
unweighted number of events	90793	14270	88000	55000	64000
cross section (pb)	4.67	1.26	49.9	16.1	62
preselection Efficiency	1	1	1	1	1
event weight for 10 pb^{-1}	5.144E-4	8.83E-4	5.67E-3	2.927E-3	9.69E-3
weighted number of events	46.7	12.6	499	161	620
single isolated electron HLT	3	8	36	8	80
PixelMatchGsfElectron, E_T >20.0 GeV, in fiducial	2	8	32	7	74
isolated (track isolation)	2	8	31	7	67
electron pass ID defined in Table 6	2	8	30	7	67
$\not{E}_T$> 20.0 GeV	2	6	24	4	59

9.2.1 Hadronic background estimate: the "matrix" method

For light parton di-jet background (EM-enriched di-jet samples) and the $b\bar{b}$ background (their sum will be called QCD background from now on), we have studied events which have passed our electron selection, with the offline track isolation requirement inverted (Figure 46). It is observed in Figure 47 that the $\not{E}_T$ distribution of the sum of the QCD events is relatively independent of whether the candidates pass or fail the isolation requirement. This suggests that $\not{E}_T$ for the isolated electrons from the QCD can be modeled by the anti-isolated electrons. As it is also shown in Appendix A, γ^*/Z $\to$ e$^+$e$^-$ candidates with one electron momentum vector removed from the $\not{E}_T$ calculation, provides a reasonable representation of the $\not{E}_T$ distribution in W $\to$ ev events.

Given these templates for W signal and QCD background it is possible to subtract the QCD background via the following algebraic method. Let $N_{<20}$ and $N_{>20}$ be the number of observed events passing the electron selection, with $\not{E}_T$ less than or greater than 20 GeV, respectively. Each N has three components: W events, QCD events, and electroweak (EWK) background events. Let f_{QCD} be the ratio, measured from the anti-isolated electrons, of QCD background events with $\not{E}_T > 20$ GeV, to similar events with $\not{E}_T < 20$ GeV. The f_{QCD} has a value of f_{QCD}=0.2413 $\pm$ 0.0019 assuming that the W and electroweak (EWK) background events are properly subtracted. If we don't subtract the EWK background then the f_{QCD} =0.2438 $\pm$ 0.0019 which is very close to the estimated f_{QCD} after the EWK subtraction showing that the contamination from the EWK background of the $\not{E}_T$ distribution after the inversion of the offline isolation is negligible. If we neglect the W events as well then the f_{QCD} =0.2600 $\pm$ 0.0020 increasing the f_{QCD} by 7.8%. We will assume that both the EWK and W events can be properly subtracted so the f_{QCD} =0.2413 $\pm$ 0.0019 will be used in this study.

Let f_Z be the same ratio for the $\not{E}_T$ distribution given by the γ^*/Z $\to$ e$^+$e$^-$ events used to model the W $\not{E}_T$ distribution. Its value was estimated to be f_Z =8.7 $\pm$ 0.5 (to be compared with the f_W =8.13 which is the value from the W $\not{E}_T$ distribution).

Then the number of QCD events with isolated electrons with $\not{E}_T > 20$ GeV, $N^{QCD}_{>20}$, and the number of W events

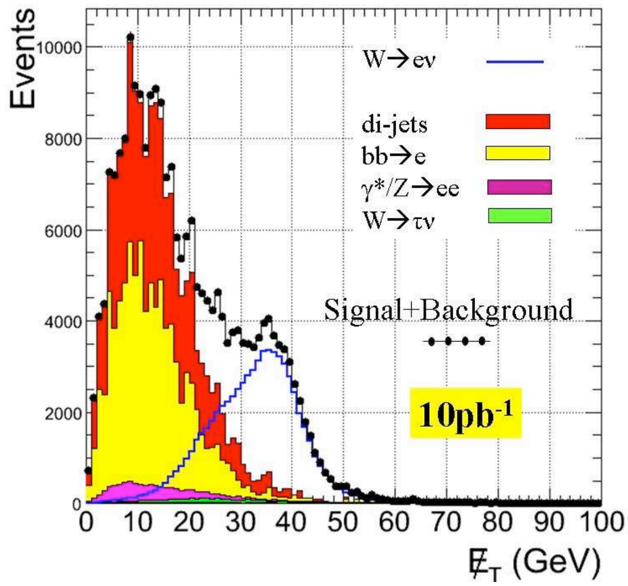

s

Figure 45: The $\not\!\!E_T$ distribution for the W $\rightarrow$ eν and the most important backgrounds after selection.

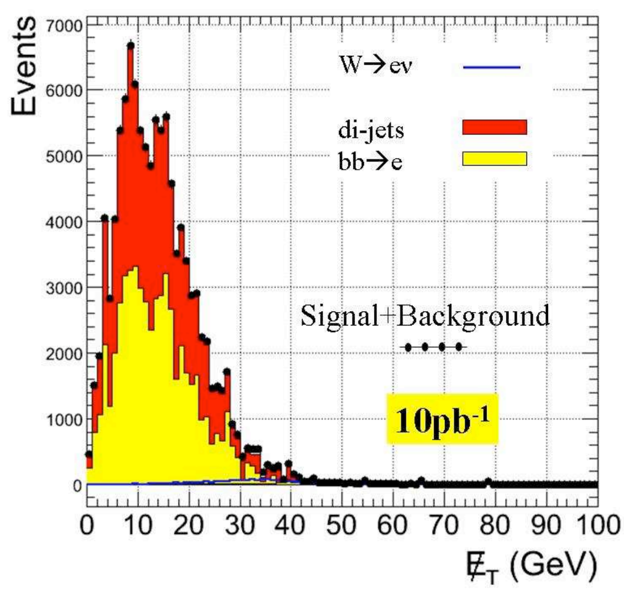

Figure 46: $\not\!\!E_T$ distribution for electron candidates from different channels which fail the isolation requirement.

Table 13: QCD Backgrounds for the $W \rightarrow e\nu$ selection

Selection Criterion	25< $\hat{p}_t$ <50	50< $\hat{p}_t$ <170	170< $\hat{p}_t$
unweighted number of events	2.16892e+06	1.03227e+06	342380
cross section (pb)	3.328e+08	2.43e+07	130000
preselection Efficiency	0.028	0.22	0.8
event weight for 10 pb^{-1}	42.9633	51.789	3.03756
weighted number of events	9.3184e+07	5.346e+07	1.04e+06
single isolated electron HLT	233376	69190	646
PixelMatchGsfElectron, E_T >20.0 GeV, in fiducial	102983	44383	416
isolated (track isolation)	61566	24340	197
electron pass ID defined in Table 6	52286	19058	151
$\not\!\!E_T$> 20.0 GeV	9237	6214	109

Table 14: bb Backgrounds for the $W \rightarrow e\nu$ selection

Selection Criterion	5< $\hat{p}_t$ <50	50< $\hat{p}_t$ <170	170< $\hat{p}_t$
unweighted number of events	3e+06	3e+06	2.6e+06
cross section (pb)	89.5e+09	24.3e+06	13.0e+04
preselection Efficiency	0.00019	0.0068	0.0195
event weight for 10 pb^{-1}	56.683	0.5508	0.00975
weighted number of events	1.7E+8	1.6524E+6	2.535E+4
single isolated electron HLT	664778	21702	125
PixelMatchGsfElectron, E_T >20.0 GeV, in fiducial	132015	10375	77
isolated (track isolation)	79470	4828	22
electron pass ID defined in Table 6	76465	4424	19
$\not\!\!E_T$> 20.0 GeV	11507	1335	14

with $\not\!\!E_T > 20$ GeV, $N^W_{>20}$, are given by

$$N^{QCD}_{>20} = f_{QCD} N^{QCD}_{<20} = f_{QCD}(N_{<20} - N^{EWK}_{<20} - \frac{1}{f_Z} N^W_{>20})$$
$$N^W_{>20} = N_{>20} - N^{EWK}_{>20} - N^{QCD}_{>20}$$

resulting in two equations with two unknowns, $N^{QCD}_{>20}$ and $N^W_{>20}$. The electroweak background yields $N^{EWK}_{<20}$ and $N^{EWK}_{>20}$ can be estimated from simulation. Solving for the two unknowns results in the equations

$$N^{QCD}_{>20} = f_{QCD}((1 + \frac{f_{QCD}}{f_Z - f_{QCD}})(N_{<20} - N^{EWK}_{<20}) - \frac{1}{f_Z - f_{QCD}}(N_{>20} - N^{EWK}_{>20}))$$
$$N^W_{>20} = \frac{f_Z}{f_Z - f_{QCD}}(N_{>20} - N^{EWK}_{>20} - f_{QCD}(N_{<20} - N^{EWK}_{<20}))$$

If we additionally correct for the efficiency of the $\not\!\!E_T$ cut, by dividing by $\epsilon(\not\!\!E_T) = f_Z/(1 + f_Z)$, then the total yield of W's is given by

$$N^W = \frac{1 + f_Z}{f_Z} N^W_{>20} = \frac{1 + f_Z}{f_Z - f_{QCD}}(N_{>20} - N^{EWK}_{>20} - f_{QCD}(N_{<20} - N^{EWK}_{<20}))$$

Table 15 lists the expected number of events in each category, for both isolated and non-isolated electrons. Applying the formula results in a measured, background-subtracted W yield of 67954 $\pm$ 674 events to be compared with the true W yield in this signal/background cocktail of 67369. Systematic uncertainties which remain to be estimated include: the accuracy of predictions for the electroweak backgrounds, the bias of estimating f_{QCD} from

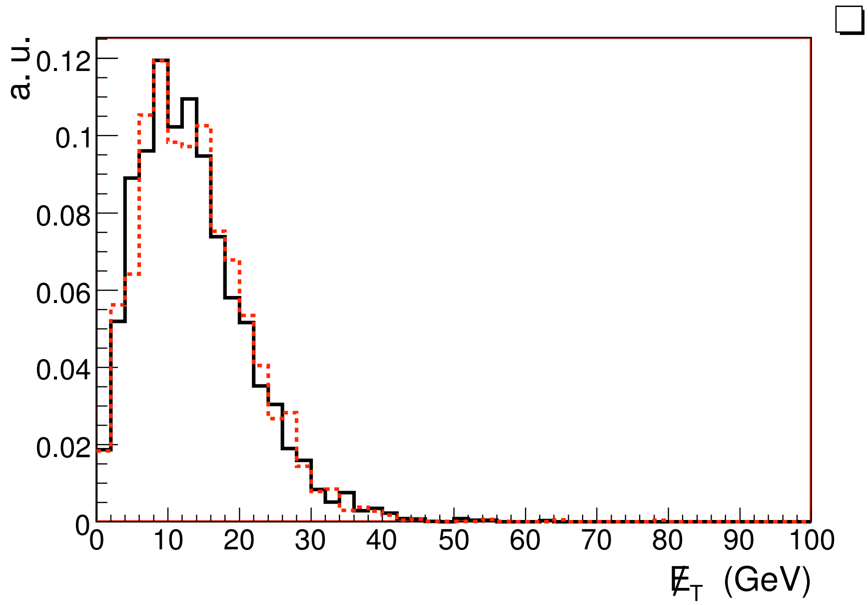

Figure 47: $\not\!\!E_T$ distribution for electron candidates in QCD dijets which pass (blue) and fail (red) the isolation requirement.

non-isolated events, and the bias of estimating $\epsilon(\not\!\!E_T)$ using f_Z. Another source of bias which has been ignored is the presence of W and EWK events in the non-isolated electron sample. This could be corrected by measuring the inefficiency of the isolation requirement from $Z \to ee$ events.

Table 15: Expected events in various categories of the algebraic method. Event yields listed are those satisfying the $\mathrm{W} \to \mathrm{e}\nu$ electron selection in 10 pb^{-1}, where they either fail ($N_{<20}$) or pass ($N_{>20}$) the requirement of $\not\!\!E_T > 20$ GeV.

Process	$N_{<20}$	$N_{>20}$
Non-isolated electrons		
EWK	223	265
QCD (udscg)	40938	9998
QCD (bb)	43525	10380
W	151	1377
Total	84837	22020
Isolated electrons		
EWK	6851	3907
QCD (udscg+bb)	122311	29510
W	6985	60969
Total	136147	94386

9.2.2 Hadronic background estimate: the "template" method

If, for some discriminating variable(s), there exist reliable pre-defined distributions with free normalization (usually called "templates" or simply "shapes") for background and signal distributions, then the signal and hadronic background yields can be estimated from a fit to that variable distribution. Such shapes could be defined by an independent data-driven method (or MC for the signal).

One such candidate variable is $\not\!\!E_T$. The signal distribution is peaked near 40 GeV, whereas hadronic background is peaked near zero, with a tail of mismeasured jet events leaking into the signal region. The hadronic background template for $\not\!\!E_T$ should come from a data sample which is unbiased in its $\not\!\!E_T$ distribution (relative to that of hadronic events passing the W selection), and which has minimal contamination from electroweak processes with real $\not\!\!E_T$. One such candidate selection is reversing the isolation requirements for electron identification. To obtain adequate statistics for this sample, it may be necessary to use a non-isolated HLT electron path. The $\not\!\!E_T$ PDF can be modeled as the product of an exponential and a polynomial,

$$P_b(\not\!\!E_T) = e^{-\alpha \not\!\!E_T} \cdot \sum_{i=0}^{n} c_i {\not\!\!E_T}^i,$$

or something similar. It then remains to demonstrate through data or MC studies whether this is an unbiased $\not\!\!E_T$ distribution and that signal contamination is low (or adequately subtractable), particularly at high $\not\!\!E_T$. Bounds on the bias or any signal contamination could be used to estimate systematic uncertainties.

Once the background template is obtained, the $W \to e\nu$ candidate sample (with no $\not\!\!E_T$ selection applied) can be fit to obtain the number of hadronic background events and signal events. There are a few variations to this procedure. The simplest is to define $\not\!\!E_T$ regions where signal and background are separately dominant (above and below $\not\!\!E_T = 20$ GeV, e.g.), obtain the background normalization by fitting the background template to the low $\not\!\!E_T$ region, and then integrate the background PDF in the signal region to estimate the hadronic background above the $\not\!\!E_T$ cut. Another method is to include also templates for the signal (and electroweak backgrounds), estimated from simulation or some other control sample, and then perform a multi-component fit over either the low $\not\!\!E_T$ region (and then extrapolate as before) or perform a multi-component fit over the entire $\not\!\!E_T$ distribution to estimate the (background-subtracted) signal yield directly. Any of these procedures will have a statistical uncertainty in the background subtraction resulting from the finite fit sample statistics. There will also be systematic uncertainties, resulting primarily from any biases or mismodelling in the background or signal templates.

9.2.3 Measurement of electron misidentification probability

The probability that, in a sample of events passing the isolated single electron HLT, a jet is misidentified as an electron can be measured from data. For this purpose, a sample consisting mainly of fake electrons has to be defined. This can be done by exploiting the topology of QCD di-jet events which are characterized by two jets balanced in the transverse plane and by low missing transverse energy. In particular, the following variables can be used to define a sample of 'pure' fake electrons among electron candidates passing the HLT:

- $\Delta\phi$, the azimuthal separation between the HLT electron supercluster and the leading jet;
- E^T_{SC}/E^T_{jet}, the ratio between the supercluster transverse energy and the leading jet transverse energy.

For fake-electrons from di-jets, the first variable is peaked at π because the two jets (one of which is the fake-electron) are back-to-back in the transverse plane; the ratio E^T_{SC}/E^T_{jet} peaks at 1 as the two jets are balanced. The distributions of these two variables are shown in figures 48, 49, 50 and 51.

A sample constituted mainly of di-jets can be thus obtained imposing, for example, $\Delta\phi > 2.5$ and an upper cut on E^T_{SC}/E^T_{jet}. Moreover the di-jets sample purity can be sensitively improved by an "anti-MET" cut, i.e. by requiring events with low missing transverse energy: this helps to reject, by definition, W $\to$ ev events where the neutrino gives missing energy and to keep di-jets which, on the contrary, are expected to be balanced. For example, a purity better than 98% is achieved requiring $E^T_{SC}/E^T_{jet} < 1.0$ and MET<20 GeV.

It can be noticed that a sample consisting mainly of real electrons from W $\to$ ev can be defined by selections on $\Delta\phi$ and E^T_{SC}/E^T_{jet} that are complementary to those applied to define the fake electrons sample (for example by requiring $\Delta\phi$ <2 and $E^T_{SC}/E^T_{jet} > 1.5$). This sample of electrons could be used to test the efficiency of the offline electron identification selections. The method assumes that the jet reconstruction is accurate enough in order both $\Delta\phi$ and E^T_{SC}/E^T_{jet} to preserve their discrimination power. This might not be true at the first data taking period.

9.3 Electroweak backgrounds to $\mathrm{Z} \to \mathrm{e}^+\mathrm{e}^-$ events

The electroweak background in the $\gamma^*/\mathrm{Z} \to \mathrm{e}^+\mathrm{e}^-$ channel is expected to be small and can be estimated adequately using simulation. In Tables 16, 17 and 18 the number of events passing each selection step for the $\gamma^*/\mathrm{Z} \to \mathrm{e}^+\mathrm{e}^-$, $\gamma Z \to \tau\tau$, $t\bar{t}$ and W+jets (in different $\hat{P}_T$ bins) channels is shown.

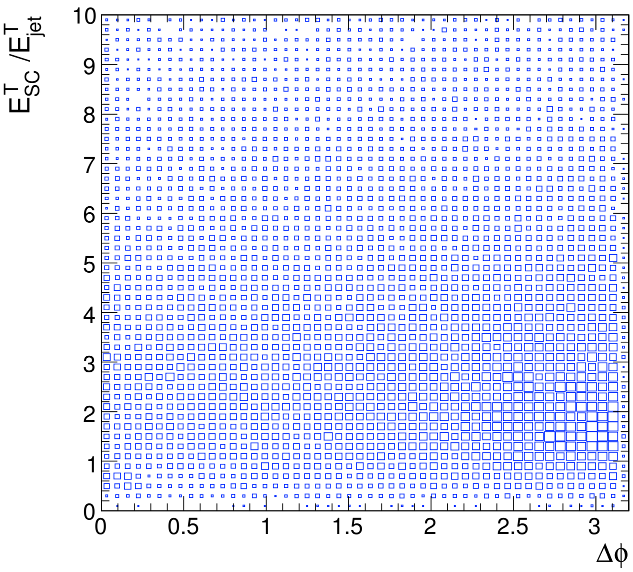

Figure 48: Scatter plot of the ratio E^T_{SC}/E^T_{jet} between the supercluster transverse energy and the leading jet transverse energy as a function of the azimuthal separation $\Delta\phi$ between the HLT electron supercluster and the leading jet for $W \to e\nu$ events.

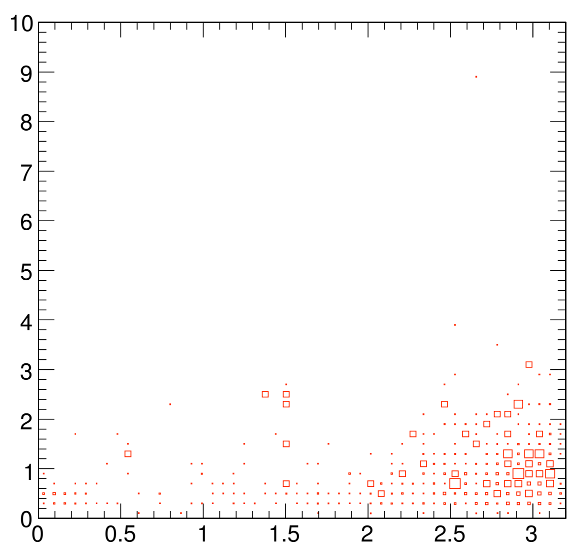

Figure 49: Scatter plot of the ratio E^T_{SC}/E^T_{jet} between the supercluster transverse energy and the leading jet transverse energy as a function of the azimuthal separation $\Delta\phi$ between the HLT electron supercluster and the leading jet for di-jet events.

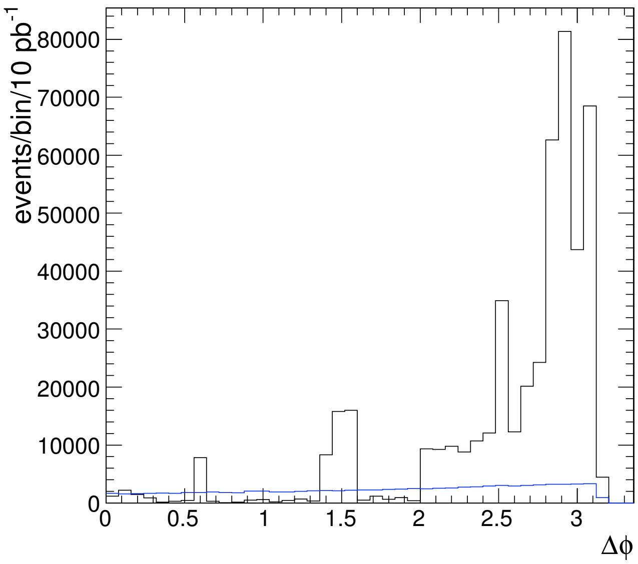

Figure 50: Distribution of the azimuthal separation $\Delta\phi$ between the HLT electron and the leading jet. The blue line represents W events, the black one refers to QCD di-jets; both of them have passed the single electron HLT selection.

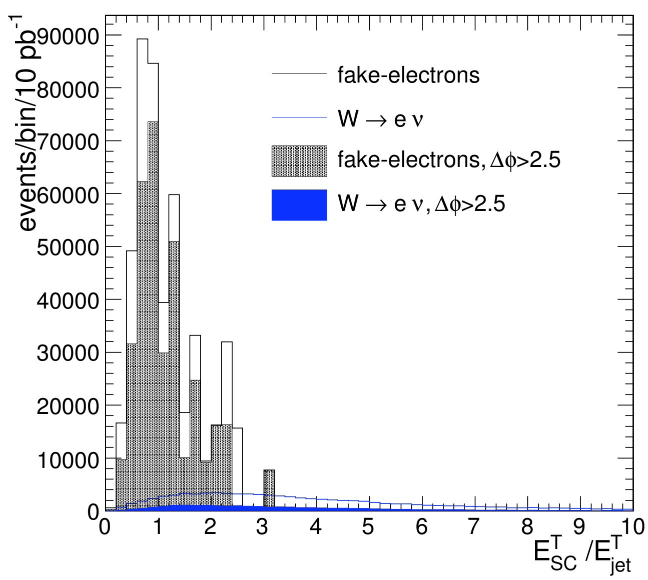

Figure 51: Distribution of the variable E_{SC}^T/E_{jet}^T, the ratio between the supercluster transverse energy and the leading jet transverse energy for events (W, blue line; QCD, black line) that have passed the single electron HLT selection.

Table 16: Signal Selection for $\gamma^*/\mathrm{Z} \rightarrow \mathrm{e}^+\mathrm{e}^-$

Selection Criterion	$\gamma^*/\mathrm{Z} \rightarrow \mathrm{e}^+\mathrm{e}^-$	$\gamma Z \rightarrow \tau\tau$	$t\bar{t}$
unweighted number of events	977634	482292	648918
cross section (pb)	1787	1586	840
preselection Efficiency	0.648	1	1
event weight for 10 pb^{-1}	1.185E-2	3.289E-2	1.295E-2
weighted number of events	11580	15860	8400
single isolated electron HLT	7939	872	993
two PixelMatchGsfElectrons, E_T >20.0 GeV, in fiducial	4724	33	158
both isolated (track isolation)	4178	18	39
both pass electron ID defined in Table 6	4139	12	36
70< $M_{e,e}$ <110 GeV	3908	0	

Table 17: W+jets Selection for $\gamma^*/\mathrm{Z} \rightarrow \mathrm{e}^+\mathrm{e}^-$

Selection Criterion	0< $\hat{P}_T$ <15	15< $\hat{P}_T$ <20	20< $\hat{P}_T$ <30	30< $\hat{P}_T$ <50
unweighted number of events	15000	26300	55000	55000
cross section (pb)	17040	1722	1914	1541
preselection Efficiency	0.1123	1	1	1
event weight for 10 pb^{-1}	1.276	0.655	0.348	0.280
weighted number of events	19136	17220	19140	15410
single isolated electron HLT	3023	6047	6995	5811
two PixelMatchGsfElectrons, E_T >20.0 GeV, in fiducial	47	2	10	60
both isolated (track isolation)	11	0	4	14
both pass electron ID defined in Table 6	6	0	3	8
70< $M_{e,e}$ <110 GeV	2	0	0	2

9.4 Hadronic backgrounds to $\mathrm{Z} \rightarrow \mathrm{e}^+\mathrm{e}^-$ events

The hadronic background results from one or both leptons originating from jets. Possible production mechanisms include $b\bar{b}$ or $c\bar{c}$ production followed by heavy quark decay to leptons, dijet production where the jet fragments are misidentified as leptons, and W, Z + jet production where one of the leptons is from electroweak boson production and the other is from a jet.

In Tables 19 and 20 the number of events passing each selection step for the di-jet and $b\bar{b}$ backgrounds is shown.

The $M_{e,e}$ distribution for the $\gamma^*/\mathrm{Z} \rightarrow \mathrm{e}^+\mathrm{e}^-$ and the most important backgrounds can be seen in Figure 52. As can be seen from the figure, the backgrounds to the $\gamma^*/\mathrm{Z} \rightarrow \mathrm{e}^+\mathrm{e}^-$ is negligible.

9.4.1 Hadronic background estimate: charge correlation method

If one assumes that the lepton pairs from hadronic background are uncorrelated in charge, the number of same sign events, which has low signal efficiency, can used as an estimator for hadronic background in the sample of opposite sign events. Same-sign lepton samples will still have a significant contamination from charge-misidentified $Z \rightarrow ee$ events (especially if showering electrons are selected), the subtraction of which must be estimated from a combination of data and simulation methods. There should also be a systematic study of simulated hadronic background sources, to demonstrate that the charge correlation of the background is negligible (see Appendix B).

9.4.2 Hadronic background estimate: template method

A candidate discriminating variable for a template-based background subtraction method is the dilepton invariant mass. This will require unbiased modelling of both background and signal distributions. The tag-and-probe efficiency measurement is also investigating this method. The signal PDF $\mathcal{P}_S$ can be modeled as the superposition of

Table 18: W+jets Selection for $\gamma^*/\mathrm{Z} \rightarrow \mathrm{e}^+\mathrm{e}^-$

Selection Criterion	50< $\hat{P_T}$ <80	80< $\hat{P_T}$ <120	120< $\hat{P_T}$ <170	170< $\hat{P_T}$ <230
unweighted number of events	53000		25800	24899
cross section (pb)	706.2		70.72	20.36
preselection Efficiency	1		1	1
event weight for 10 pb^{-1}	0.1333		0.0274	8.177E-3
weighted number of events	7062		707	204
single isolated electron HLT	2778		298	86
two PixelMatchGsfElectrons, E_T >20.0 GeV, in fiducial	138		28	8
both isolated (track isolation)	17		3	0
both pass electron ID defined in Table 6	7		1	0
70< $M_{e,e}$ <110 GeV	2		0	0

Table 19: QCD Backgrounds for the $\gamma^*/\mathrm{Z} \rightarrow \mathrm{e}^+\mathrm{e}^-$ selection

Selection Criterion	25< $\hat{p_t}$ <50	50< $\hat{p_t}$ <170	170< $\hat{p_t}$
unweighted number of events	2.16892e+06	1.03227e+06	342380
cross section (pb)	3.328e+08	2.43e+07	130000
preselection Efficiency	0.028	0.22	0.8
event weight for 10 pb^{-1}	42.9633	51.789	3.03756
weighted number of events	9.3184e+07	5.346e+07	1.04e+06
single isolated electron HLT	233376	69190	646
two PixelMatchGsfElectron, E_T >20.0 GeV, in fiducial	988	3418	78
both isolated (track isolation)	42	155	6
both pass electron ID defined in Table 6	42	0	0
70< $M_{e,e}$ <110 GeV	0	0	0

a Voigtian distribution $V(M_{ee}; M, \Gamma, \sigma)$ with a bifurcated Gaussian distribution $A(M_{ee}; M, \sigma_1, \sigma_2)$,

$$\mathcal{P}_S \propto fV + (1-f)A.$$

M is the pole mass of the Breit-Wigner, Γ is its width, and σ is the Gaussian mass resolution. A is meant to model the asymmetric tail in the mass distribution due to Bremsstrahlung, with a width σ_1 below the pole mass M and width σ_2 above the pole mass M. The background PDF $\mathcal{P}_B$ can be modeled as an exponential function,

$$\mathcal{P}_B \propto e^{-bM_{ee}}.$$

The background template could also be obtained by reversing the isolation requirements, as in the case of $W \rightarrow e\nu$.

Another template-based method would use as a discriminating variable the isolation energy distribution of one of the leptons. To remove trigger bias, the lepton studied is either one which fails HLT selection, or is chosen at random if both pass the HLT. The background template could come from a non-isolated HLT path, where electron isolation has been reversed for the triggering electron. The signal template would have to be estimated from simulation.

10 Uncertainties

The uncertainty of any estimation of the production cross section can be factored into the following (in principle) uncorrelated sources:

- **Signal yield**: The uncertainty of the estimate of the background-subtracted signal yield of selected events. In general, this includes a statistical component, due to the finite sample sizes used to estimate signal and backgrounds, and also a systematic component, arising from uncertain knowledge of the biases of the background subtraction method.

Table 20: $b\bar{b}$ backgrounds for the $\gamma^*/\mathrm{Z} \rightarrow \mathrm{e}^+\mathrm{e}^-$ selection

Selection Criterion	5< $\hat{p}_t$ <50	50< $\hat{p}_t$ <170	170< $\hat{p}_t$
unweighted number of events	3e+06	3e+06	2.6e+06
cross section (pb)	89.5e+09	24.3e+06	13.0e+04
preselection Efficiency	0.00019	0.0068	0.0195
event weight for 10 pb^{-1}	56.683	0.5508	0.00975
weighted number of events			
single isolated electron HLT	664778	21702	125
two PixelMatchGsfElectron, E_T >20.0 GeV, in fiducial	510	488	16
both isolated (track isolation)	113	6	0
both pass electron ID defined in Table 6	0	1	0
70< $M_{e,e}$ <110 GeV	0	1	0

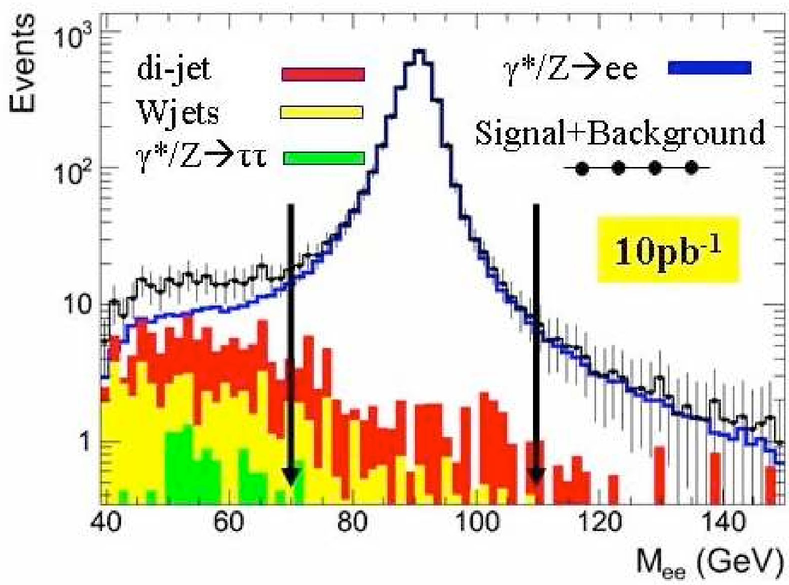

Figure 52: The $M_{e,e}$ distribution for the $\gamma^*/\mathrm{Z} \rightarrow \mathrm{e}^+\mathrm{e}^-$ and the most important backgrounds.

- **Efficiency**: The uncertainty of the estimate of the selection efficiency for selected events in the fiducial region of the analysis. Again, there will be statistical and systematic components, owing to control sample statistics and bias in the background subtraction method. This estimation is binned with respect to (at least) electron E_T and η, so there are binned uncertainties which must be correctly propagated.

- **Acceptance**: The uncertainty of the estimate of the fraction of produced events which enter the fiducial region of the analysis. Here the uncertainty is predominantly systematic and includes uncertain biases arising from an imperfect signal model, or an uncertain determination of the fiducial region (mismeasured electron energy/direction, missing energy, or pp vertex).

- **Integrated luminosity**: The uncertainty of the integrated luminosity of the data sample considered. The integrated luminosity measurement is expected to have at least 10% accuracy from an initial Van der Meer scan of the CMS beam spot size, combined with LHC measurements of integrated beam currents. With effort, this could be improved to as little as a few percent. Low-angle detectors, such as TOTEM, will also measure integrated luminosity with similar projected precision, but whether that precision will be available with 10 pb^{-1} is unknown.

As the cross section is directly (or inversely) proportional to each of these factors, the square of the total relative uncertainty of the cross section is simply the sum in quadrature of the relative uncertainties of the above factors. This simple picture is complicated somewhat by confounding factors.

In the case of $Z \to ee$, the samples used to estimate the signal yield are strongly overlapping, if not identical, to the samples used to determine efficiency. This introduces an anti-correlation between that signal yield and its efficiency, which means assuming they are uncorrelated leads to an overestimate of the cross section uncertainty. The impact of this correlation and possible solutions are discussed in Appendix C.

10.1 Theoretical Uncertainties on the Acceptance

In the following we discuss the effect of the theoretical uncertainty of the acceptance on the production cross-section systematic evaluation, and propose which MC generator and scheme needs to be implemented in order to best simulate the events.

10.1.1 Higher order Electroweak Correction and Recommended MC Generator

The importance of including higher order corrections has been well established by many authors [32, 33]. Next to Leading Order (NLO) electroweak and QCD corrections are known both for W boson production and Z boson production. However, the current state of the art MC generators do not include both sets of corrections. The generator MC@NLO [25], combines a MC event generator with NLO calculations of rates for QCD processes and uses the HERWIG event generator for the parton showering. The MC@NLO package does not include higher order electroweak corrections hence we evaluated their contribution to the systematic uncertainty on acceptance to the Z measurement production cross section measurement using HORACE [31] event generator.

HORACE [31] [1)] includes the exact 1-loop electroweak radiative corrections matched with a QED Parton Shower to take into account also higher-order QED leading effects. The objectives were first to find out whether QED final state radiations contribution is the dominant under the Z peak as expected and second to evaluate the the systematic uncertainty if we replace HORACE with PHOTOS which simulate only final state radiation. At the time of the study the exact O(α) electroweak virtual and real corrections to the neutral current process were not yet included in HORACE . We first compared the QED final state corrections in the leading log approximation with those modeled by adding PHOTOS to Herwig. We compared HORACE parton showered with Herwig (with no O(α) electroweak corrections) to Madgraph generated $pp \to Z/\gamma^* \to e^+e^-$ events parton showered with Herwig+PHOTOS. The results are shown in Figs. 53 - 55.

Even though it seems we have nice agreement as expected between the different event generators the resulting cross sections after the kinematical cuts $\sigma_{Madgraph} = 472.3 \pm 1.6$ and $\sigma_{Horace} = 484.1 \pm 1.6$ manifest significant difference in the values of the production cross sections. An update version 2 of HORACE with a bug fixed is currently available. We will have to check if the new version resolves the large difference in the pseudo rapidities of the di-leptons which yield the corresponding difference in the cross sections after the cuts. We will proceed in the following assuming that we proved that final state QED radiation is the dominant contribution under the Z peak and therefore we would use MC@NLO interfaced with PHOTOS as our primary event generator.

For completeness we also compared MC@NLO interfaced with PHOTOS with distributions from ResBos-A [30] – a MC simulation that includes final state NLO QED corrections to W/Z boson production and NNLO logarithmic resummation of soft and collinear QCD radiation. The results can be seen in Fig. 56, the invariant di-electron mass distribution and Fig. 57 the transverse momentum distribution of the Z boson. The latter exhibits the effects of the NNLO resummation at low p_T in ResBos-A [30]. The only generator level cut used in these comparison plots is the $M_{ee} > 50$ GeV/c^2. Within the $Z \to e^+e^-$ acceptance region defined by $|\eta_e| < 2.5$ with $1.4442 < |\eta| < 1.566$ excluded, $p_T > 20$ GeV/c and $85 < M_{ee} < 95$ GeV/c^2, the resultant cross-sections, $\sigma_{\mathrm{MC@NLO}} = 507 \pm 2$ and $\sigma_{\mathrm{Resbos-A}} = 516 \pm 2$, agree to within O(2%) however, it may be possible to scale the MC@NLO to better match the Resbos-A calculation.

10.1.2 Higher order QCD effects

A comparison of the central value and the acceptance due to higher order calculations is presented in Table 21. The LO and NLO calculations used CTEQ6.5 PDFs. The program used to calculate the NNLO corrections is FEWZ [34] with MRST2002 [**?**] PDF. The FEWZ computation is valid through NNLO in perturbative QCD, includes spin correlations, finite widths effects, γ-Z interference and is differential. Since the NNLO matrix element has not yet been interfaced to a shower, We can obtain the correct comparison of MC@NLO to NNLO by

[1)] Version 2

[1)] Comparison with V3 of HORACE is in progress

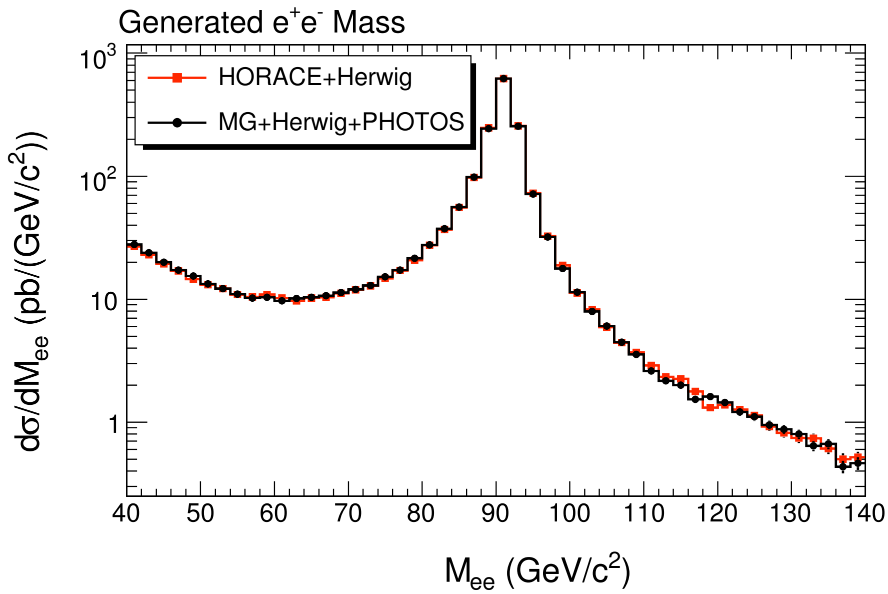

Figure 53: Comparison of e^+e^- invariant mass distributions for the process $Z/\gamma^* \rightarrow e^+e^-(n\gamma)$ in HORACE parton showered with Herwig (red squares) and Madgraph parton showered with Herwig plus PHOTOS (black circles).

multiplying the MC@NLO results with "k" factor computed by FEWZ. The results from the table 21 yield about 1% error on the acceptance from not having NNLO QCD correction.

	$\sigma(M_Z > 40$ GeV$/c^2)$	σ (Cuts)	Acceptance
LO	1832 ± 2.0	477.59 ± 1.56	0.2607 ± 0.0006
MC@NLO	2331 ± 3.0	605.00 ± 2.00	0.2595 ± 0.0005
NLO	2239 ± 2.0	671.91 ± 0.67	0.3001 ± 0.0003
NNLO	2179 ± 20	660.30 ± 8.65	0.3030 ± 0.0012
NNLO x PS	2269 ± 30	594.55 ± 7.79	0.2620 ± 0.0010
$\Delta_{\mathrm{LO,MC@NLO}}$	0.2724 ± 0.0020	0.2668 ± 0.0054	-0.0044 ± 0.0030
$\Delta_{\mathrm{NLO,NNLO}}$	-0.0268 ± 0.0090	-0.0173 ± 0.0129	0.0098 ± 0.0041
$\Delta_{\mathrm{MC@NLO,NNLO+PS}}$	-0.0266 ± 0.0091	-0.0173 ± 0.0133	0.0096 ± 0.0043

Table 21: Calculation of the $Z/\gamma^* \rightarrow \ell^+\ell^-$ cross-section at LO using MadGraph [35] and at NLO and NNLO using FEWZ [34]. The PDF calculations are from MRST2002 and the cut region is defined by both electrons having $|\eta| < 2.5$ with $1.4442 < |\eta| < 1.560$ excluded, $p_T > 20$ GeV/c and $85 < M_{ee} < 95$ GeV/c^2.

The computational errors quoted in Table 21 are from MC errors in evaluating the cross sections, which are substantial in the NNLO calculations, due to the length of the calculations and slow convergence of the high-dimensional numerical integration used in the evaluation.

10.1.3 Uncertainties due to the Parton Distribution function

Phenomenological parametrization of the PDFs are taken from a global fit to data. Therefore, uncertainties on the PDFs arising from diverse experimental and theoretical sources will propagate from the global analysis into the predictions for the W/Z cross sections. Figure 58 shows the results of the inclusive Z to di-lepton production cross-section using various CTEQ [27] and MRST [28] PDFs. The upward shift of about 7% (between CTEQ6.1 and 6.5 and MRST2004 and 2006) results from the inclusion of heavy quark effects in the latest PDF calculations. It is interesting to note the small variation in the acceptance due to the cuts using each of these PDFs shown in Fig 59. In addition the cross-section errors for different values of the kinematic cuts on the electrons are shown in Figs. 60 and 61.

The uncertainties in the PDFs arising from the experimental statistical and systematic uncertainties and the effect on

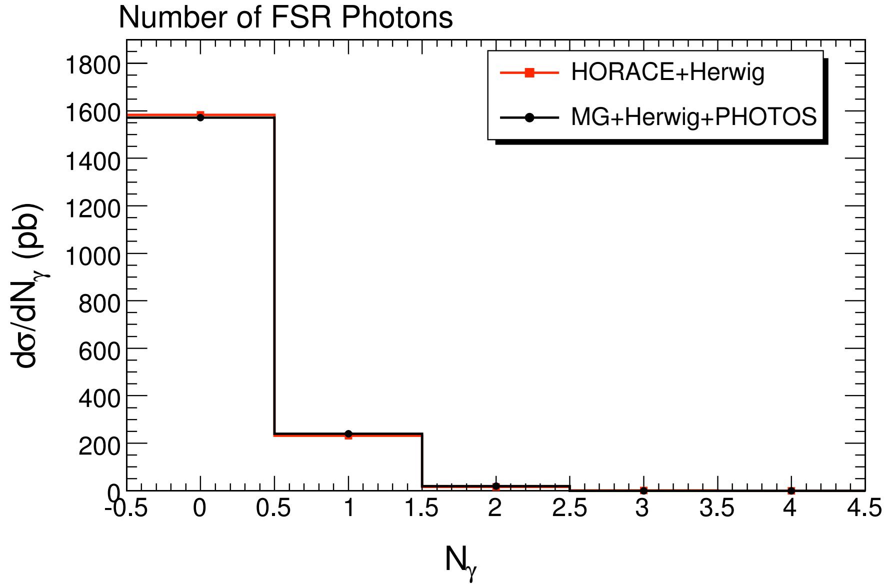

Figure 54: Comparison of $Z/\gamma^* \to e^+e^-(n\gamma)$ number of final state radiation (FSR) photons for HORACE parton showered with Herwig (red squares) and Madgraph parton showered with Herwig plus PHOTOS (black circles).

the production cross section of the Z boson has been studied using the standard methods proposed in [27, 20]. For the standard set of PDFs, corresponding to the minimum in the PDF parameter space, simultaneously a complete set of eigenvector PDF sets have been calculated, characterizing the region nearby the minimum of the standard set. From these sets we calculate the best estimate and the uncertainty for the Z cross section. The uncertainty for the cross section due to the PDF uncertainties is evaluated using the methods described in [27]. Fig. 58 list the results for the different pdfs and table 22 summarize the results of the latest CTEQ and MRST PDF sets. The difference of approximately a factor 2 between the results obtained from the CTEQ and MRST PDF sets is due to different assumptions made by the groups while creating the eigenvector PDF sets. The fractional error on the acceptance due to the PDFs using the suggested cut in this analysis using CTEQ6.5 is about 1.5% and using MRST2006 is about 1.3%

	$M_Z > 40$ GeV/c^2			Acceptance Region			Acceptance		
PDF Set	σ (pb)	$\Delta\sigma_+$	$\Delta\sigma_-$	σ (pb)	$\Delta\sigma_+$	$\Delta\sigma_-$	a	Δa_+	Δa_-
CTEQ6.5	2330	103	104	605.9	15.4	24.8	0.260	0.003	0.005
MRST2006	2333	42	40	610.8	11.3	13.1	0.262	0.003	0.004
CTEQ6.1	2155	123	109	559.3	25.0	21.6	0.260	0.003	0.005
MRST2004 (NNLO)	2193	41	45	572.0	12.4	10.9	0.261	0.005	0.002
MRST2004 (NLO)	2223	42	46	578.1	12.6	11.0	0.260	0.005	0.002

Table 22: Cross-sections and asymmetric Hessian uncertainties as calculated using several recent PDF sets. The results are also shown graphically in Fig. 58. The acceptance region is defined as both electrons having $|\eta| < 2.0$ with $1.4442 < |\eta| < 1.566$ excluded, $p_T > 20$ GeV/c and $85 < M_{ee} < 95$ GeV/c^2

In figures 60- 65 we demonstrate the sensitivity of the cross sections and acceptances to the uncertainties affecting the PDF sets. Figure 60 and Figure 61 show the systematic error on the production cross-sections as a function of the maximum η cut and minimum electron transverse momentum. The fractional uncertainties, shown in Figs. 62 and 63, demonstrate that the relative uncertainty in the cross-section is very flat as a function of the kinematic cuts, until the region of extreme cuts and low statistics in the MC are reached. The corresponding uncertainty on the acceptance and a function of the kinematic cuts is shown in Figs. 64 and 65. These show a similar dependence to the cross-section uncertainties.

10.1.4 Uncertainties in the acceptance due to the Shower

Shower effects at NLO have been studied by looking at the cross-section and acceptance of MC generated with MC@NLO for various values of the kinematic cuts. The results are shown in Figures 66 - 69. For the nominal

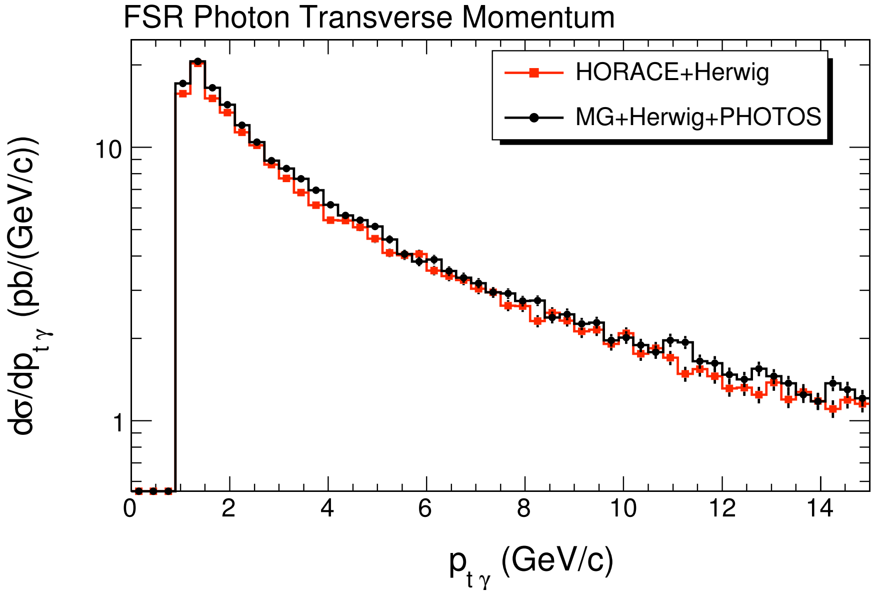

Figure 55: Comparison of $Z/\gamma^* \rightarrow e^+e^-(n\gamma)$ final state radiation (FSR) transverse momentum distributions for HORACE parton showered with Herwig (red squares) and Madgraph parton showered with Herwig plus PHOTOS (black circles).

cuts there is a difference of a ~4% between the showered and unshowered cross-sections and acceptances. As we would be using MC@NLO which contains the parton shower the contribution to the systematic uncertainty on the acceptance is a consequence of the lack of NNLO calculation matched to parton shower as is given in table 21

10.1.5 Scale dependence of the Acceptance

In a fixed order calculation matched to PDFs, a dependence on the factorization scale μ_F and renormalization scale μ_R appear in the final results. As is customary, we will choose these scales to be identical, and allow for scale uncertainty by varying them by a factor of 2 or 1/2 about a central value of $\mu_{F,R} = M_Z$, which is typical of the scales in our acceptance.

Table 23 shows the total cross sections for either di-lepton production calculated by FEWZ at three different renormalization and factorization scales $M_Z/2$, M_Z, and $2M_Z$. We present the results for the scale dependence of the kinematical cuts in Table 24. For a measure of the size of the scale dependence, the final column of each table shows the maximum difference between the three values divided by average, with an error calculated assuming the statistical errors in the three MC runs in each row are independent.

	$Z/\gamma^* \rightarrow l^+l^-$			
Order	$M_Z/2$	M_Z	$2M_Z$	$\Delta\sigma/\overline{\sigma}$
NLO	2178.3 ± 1.9	2240.7 ± 2.2	2300.0 ± 2.2	0.0545 ± 0.0038
NNLO	2164.6 ± 20.1	2175.5 ± 19.0	2193.9 ± 20.4	0.014 ± 0.013

Table 23: Scale dependence of the total cross sections for Z boson production with $M_{ee} > 40GeV$ calculated by the FEWZ program. The final column is a measure of scale dependence obtained by dividing the maximum spread by the average.

	$Z/\gamma^* \rightarrow e^+e^-$			
Order	$M_Z/2$	M_Z	$2M_Z$	$\Delta\sigma/\overline{\sigma}$
NLO	652.9 ± 0.6	671.9 ± 0.7	689.4 ± 0.7	0.0544 ± 0.0014
NNLO	629.1 ± 15.9	660.3 ± 8.7	679.5 ± 10.0	0.0768 ± 0.0286

Table 24: Scale dependence of cross sections using the analysis kinematical cuts calculated by the FEWZ program.

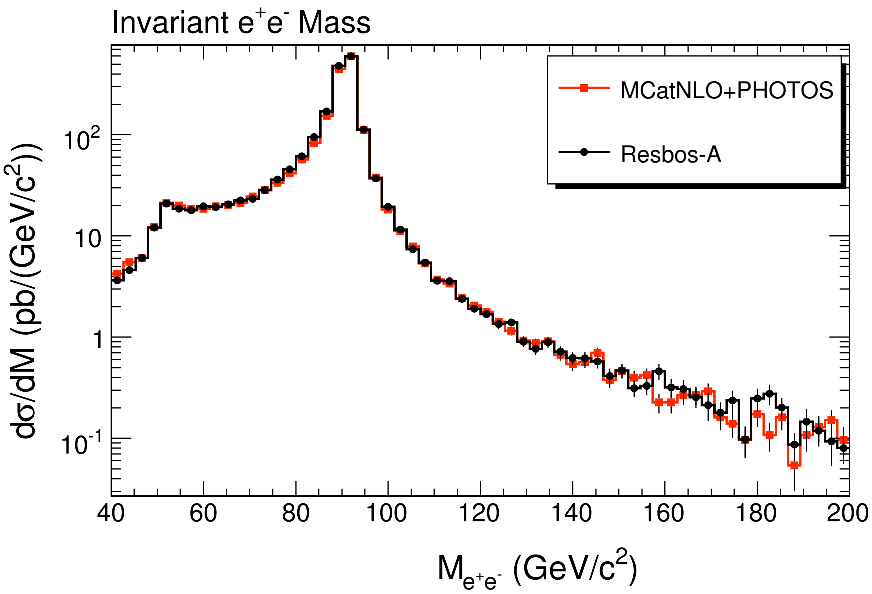

Figure 56: Comparison of e^+e^- invariant mass distributions for the process $Z/\gamma^* \to e^+e^-(n\gamma)$ in MC@NLO with PHOTOS (red squares) and Resbos-A (black circles).

We can see that the scale dependence at NLO is typically 5%. Adding NNLO reduces the scale dependence to $\mathcal{O}(1\%)$ for the total cross section. After applying the kinematical cuts, the scale dependence is not reduced as much at NNLO, it may have increased somewhat. It is difficult to draw firm conclusions in these cases, since the MC errors are relatively large at NNLO, but the very narrow invariant mass cuts on the electron could be leading to stronger scale dependence than is seen with more inclusive cuts. Further study is necessary to learn about the effect of a narrow invariant cut on the systematic uncertainty of the Z production cross section.

10.1.6 Conclusions on theoretical uncertainties on the acceptance

We conclude that the event generator MC@NLO interfaced to PHOTOS should be sufficient to guarantee an overall theoretical uncertainty on the acceptance of Z production cross section due to higher order calculation, PDFs, renormalization scale and electroweak correction at the level less than $\approx 1 - X\%$ Once the luminosity increases, large statistic will further improve the Systematic uncertainties due to PDFs the Z production cross section will provide a tool to test QCD and measure the luminosity.

11 Results

11.1 Efficiency for $\mathrm{W} \to \mathrm{e}\nu$

According to the proposed selection for the $\mathrm{W} \to \mathrm{e}\nu$, the event efficiency could be written as

$$\varepsilon_{total} = \varepsilon_{offline} \times \varepsilon_{trigger} \tag{8}$$

where the $\varepsilon_{offline}$ is the electron's efficiency to pass the offline selection defined as the following product:

$$\varepsilon_{offline} = \varepsilon_{preselection} \times \varepsilon_{isolation} \times \varepsilon_{eleID} \tag{9}$$

The $\varepsilon_{trigger}$ is the event efficiency to pass the 'single isolated electron' trigger.

It must be underlined that the selection efficiencies are measured with the above predefined order using the tag and probe method on a sample of $\gamma^*/\mathrm{Z} \to \mathrm{e}^+\mathrm{e}^-$ events. The fact that all efficiencies are measured with a well defined order removes any concerns over correlations between the various efficiencies.

[1] Further study has to be done to evaluate the NLO EWK and scale dependence to derive the combined error from theory - the study is still in progress

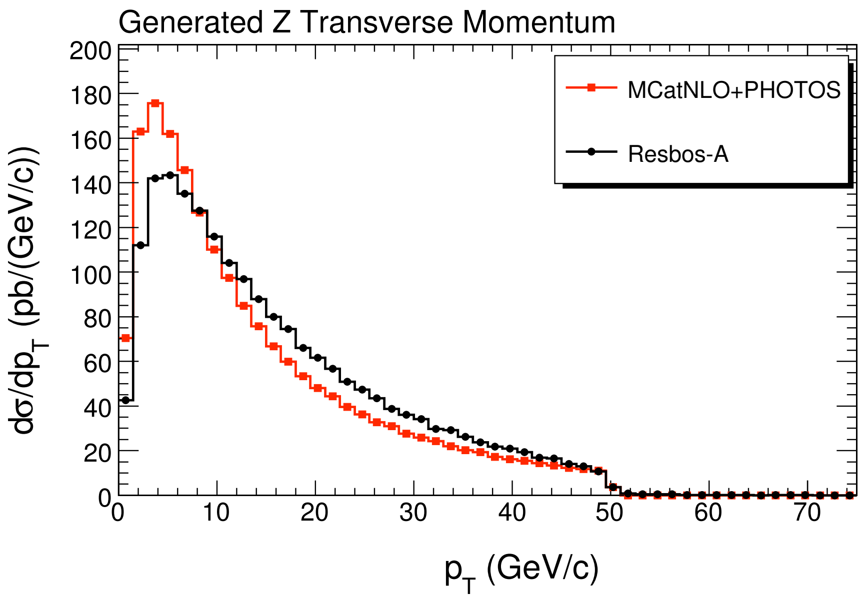

Figure 57: Comparison of the Z boson p_T distributions for the process $Z/\gamma^* \to e^+e^-(n\gamma)$ in MC@NLO with PHOTOS (red squares) and Resbos-A (black circles). The effects of the NNLO resummation at low p_T.

In order to apply, in an unbiased fashion, the electron reconstruction and selection efficiencies measured from $Z \to ee$ to the $W \to e\nu$ sample, those efficiencies must be binned with respect to any variables for which both (1) the efficiencies exhibit significant dependence and (2) the distribution differs significantly between W and Z samples. If the appropriately binned efficiency measurements are given by $\epsilon_i \pm \delta\epsilon_i$, for some index i, then the cross section is given by

$$\sigma_W \times BR(W \to e\nu) = \frac{N_W^{pass} - N_W^{bkgd}}{A_W \times \sum_i f_i\epsilon_i \times \epsilon(\not{E}_T) \times \int Ldt} \tag{10}$$

where f_i is the relative abundance of events which have an electron in the acceptance and are detected in the ith bin,

$$f_i \equiv \frac{\mathcal{A}_i}{\mathcal{A}}$$

where $\mathcal{A}_i$ is the acceptance in the i^{th} (η, E_T) bin. The f_i are determined from W $\to$ ev simulated samples.

The uncertainty induced by the $\delta\epsilon_i$ is then

$$(\delta\sigma_W/\sigma)^2 = \sum_i f_i^2 \frac{\delta\epsilon_i^2}{\epsilon^2} \tag{11}$$

where

$$\epsilon = \sum_i f_i\epsilon_i \tag{12}$$

The $\epsilon(\not{E}_T)$ is the efficiency for signal events with selected electrons to satisfy the $\not{E}_T$ requirements. The matrix method provides directly the number of background subtracted signal events before the $\not{E}_T$cut and this is the number that we will use in the cross section calculation. For completeness the estimated efficiency of the $\not{E}_T$cut was found to be $\epsilon(\not{E}_T)$ =89.7%.

Table 25 gives a summary of the results. The uncertainties quoted in the Table are of statistical nature only.

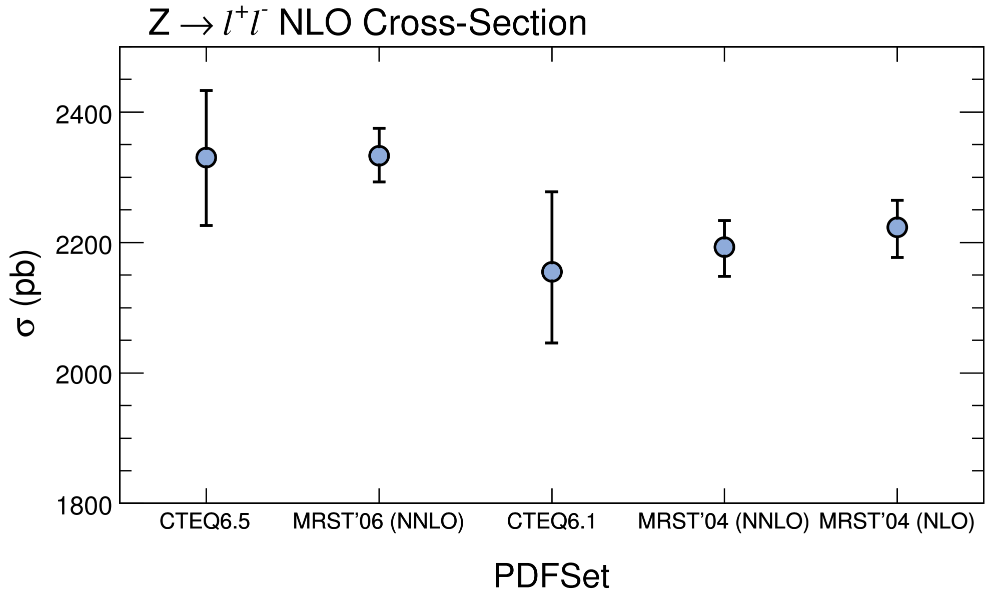

Figure 58: Comparison of $Z/\gamma^* \to \ell^+\ell^-$ cross-sections for $M_{Z/\gamma^*} > 40$ GeV/c^2 for several recent PDF calculations.

Table 25: Results for the W $\to$ ev cross section measurement

$N_{selected} - N_{bkgd}$	67954 $\pm$ 674
Tag&Probe $\varepsilon_{offline}$	84.8 $\pm$ 0.4 %
Tag&Probe $\varepsilon_{trigger}$	76.8 $\pm$ 0.5 %
Tag&Probe $\varepsilon_{offline \times trigger}$	65.1 $\pm$ 0.5 %
Acceptance	52.3 $\pm$ 0.2 %
Int. Luminosity	10 pb^{-1}
$\sigma_W \times BR(\mathrm{W} \to \mathrm{ev})$	19.97 $\pm$ 0.25 nb
cross section used	19.78 nb

11.2 Efficiency for $\mathrm{Z} \to \mathrm{e^+e^-}$

According to the proposed selection for the $\mathrm{Z} \to \mathrm{e^+e^-}$ selection, the event efficiency could be written as

$$\varepsilon_{total} = \varepsilon^2_{offline} \times \varepsilon_{trigger} \tag{13}$$

where the $\varepsilon_{offline}$ is the electron's efficiency to pass the offline selection defined as the following product:

$$\varepsilon_{offline} = \varepsilon_{gsfele} \times \varepsilon_{isolation} \times \varepsilon_{eleID} \tag{14}$$

The $\varepsilon_{clustering}$ was neglected since it is included in the acceptance calculation. The $\varepsilon_{offline}$ efficiency is squared in order to get the event efficiency since we demand two electrons in the final state.

The $\varepsilon_{trigger}$ is the event efficiency to pass the 'single isolated electron' trigger. This trigger can be fired by one or both electrons, so the trigger efficiency is practically one minus the probability both electrons to fail the 'single isolated electron' trigger. So,

$$\varepsilon_{trigger} = 1 - (1 - \varepsilon_{online})^2 \tag{15}$$

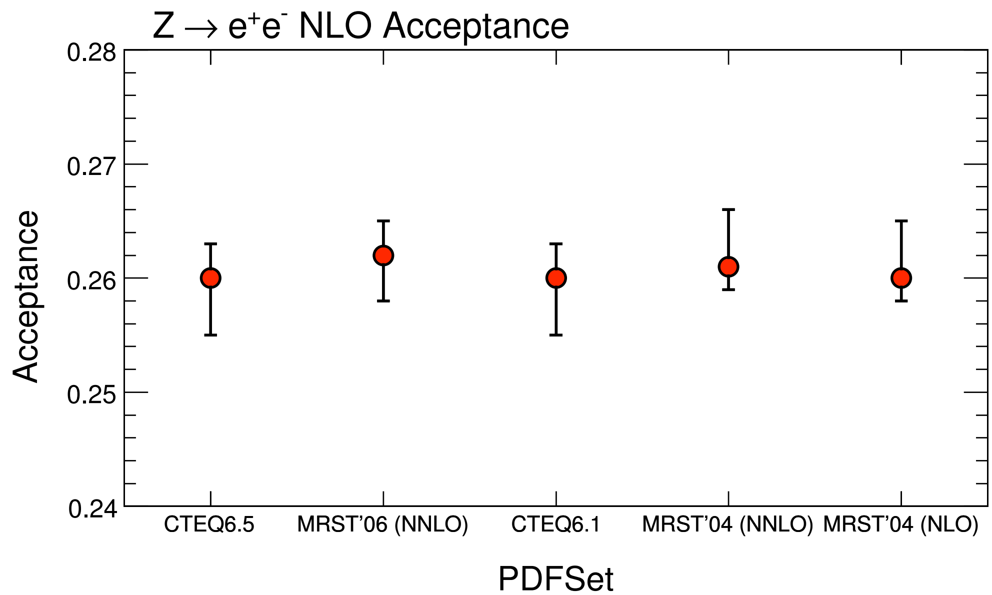

Figure 59: Comparison of $Z/\gamma^* \rightarrow e^+e^-$ acceptances for the region defined by both electrons having $|\eta| < 2.5$ but not in $1.4442 < |\eta| < 1.566$, $p_T > 20$ GeV/c and $85 < M_{ee} < 95$ GeV/c^2 with several recent PDF calculations.

where ε_{online} is the efficiency an electron that have already passed the offline selection, to fire the 'single isolated electron' trigger.

Table 26 shows a summary of the results for the $\gamma^*/\mathrm{Z} \rightarrow \mathrm{e}^+\mathrm{e}^-$ cross section measurement. As can be seen, the estimated $\gamma^*/\mathrm{Z} \rightarrow \mathrm{e}^+\mathrm{e}^-$ cross section agrees within the errors with the expected one. This is a positive sign that the selection efficiencies are correctly estimated with the tag and probe method and they don't add biases in the cross section measurement. The uncertainties quoted in the Table are of statistical nature only.

Table 26: Results for the $\gamma^*/\mathrm{Z} \rightarrow \mathrm{e}^+\mathrm{e}^-$ cross section measurement

$N_{selected}$	3914 ± 63
N_{bkgd}	assumed 0.0
Tag&Probe $\varepsilon_{offline}$	84.8 ± 0.4 %
Tag&Probe $\varepsilon_{trigger}$	94.6 ± 0.2 %
Tag&Probe ε_{total}	68.1 ± 0.6 %
Acceptance	32.39 ± 0.18 %
Int. Luminosity	10 pb^{-1}
$\sigma_{Z/\gamma^*} \times BR(Z/\gamma^* \rightarrow e^+e^-)$	1775 ± 34 pb
cross section used	1787 pb

References

[1] A. Abulencia et al., The CDF Collaboration, *Measurements of Inclusive W and Z Cross Sections in p anti-p Collisions at* $\sqrt{s} = 1.96$ *TeV*, J. Phys. G: Nucl. Part. Phys. (2007) 2457-2544.

Measurement of W and Z boson production cross sections (Run Ia)., Phys. Rev. D. 60 052003 1999 PDF (Copyright by the APS), FERMILAB PUB-99/015-E, hep-ex/9901040

[2] CMS Collaboration, Physics TDR Vol I. Detector Performance and Software, CERN/LHCC 2006-001.

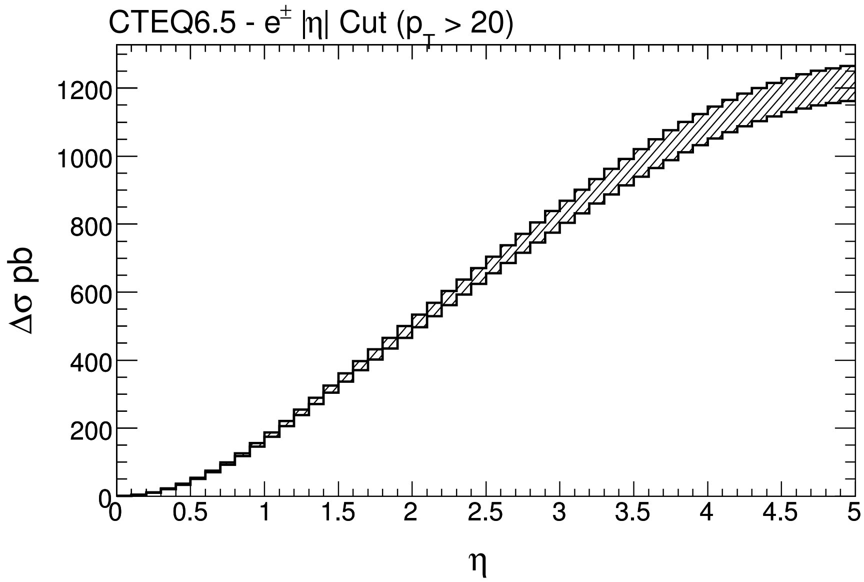

Figure 60: Error on the $Z/\gamma^* \rightarrow e^+e^-$ cross-section due to PDFs for different values of the electron $|\eta|$ cut. The momentum cut for both electrons is fixed at $p_T > 20$ GeV/c in the mass range $85 < M_{ee} < 95$ GeV/c^2.

[3] Hadron Collider Physics Symposium 2007 La Biodola, Isaola d'Elba (Italy). May 20-26,2007 https://indico.pi.infn.it/conferenceDisplay.py?confId=0

[4] S.D.Drell and T.M.Yan, Phys. Rev. Lett. **25**, 316 (1970).

[5] A.D.Martin et al., *Parton Distributions and the LHC: W and Z Production*, **hep-ph/9907231**.

[6] A. Tricoli, *Uncertainties on W and Z production at the LHC HERA - LHC Workshop Proceedings*, **hep-ex/0509002**.

[7] C. Anastasiou et al., *High-precision QCD at hadron Colliders: electroweak gauge boson rapidity distribution at NNLO*, **hep-ph/0312266**.

[8] Particle Data Book

[9] CMS Collaboration, The Level-1 Trigger, TDR, CERN/LHCC 2000-038.

[10] CMS Collaboration, Data Acquisition & High-Level Trigger , TDR, CERN/LHCC 2002-26.

[11] S. Baffioni et. al., *Electron reconstruction in CMS*, **CMS NOTE-2006/040**.

[12] CMS Collaboration, Preprint CERN/LHCC 2007-021.

[13] S. Esen et al., *"$\not{E}_T$ Performance in CMS"* **CMS AN-2007/041**.

[14] G.Daskalakis et al., *Measuring Electron Efficiencies at CMS with Early Data*, **CMS AN-2007/019**.

[15] Tag and Probe in CDF

[16] Tag and Probe in D0

[17] CTEQ pdfs: J. Pumplin et al., JHEP 0207:012 and arXiv:hep-ph/0201195 (2002).

[18] MRST pdfs: R.S. Thorne et al., Acta Phys.Polon. B33 (2002) 2927-2932 and arXiv:hep-ph/0207067 (2002)

[19] FEWZ K. Melnikov, F. Petriello Phys.Rev. D74 (2006) 114017

[20] A.D. Martin et al., arXiv:hep-ph/0211080 (2002)

[21] CDF Coll., D. Acosta *et al.*, Phys. Rev. Lett. 94, 091803 (2005); D0 Coll., D0 Notes 4573 and 4750 (2005).

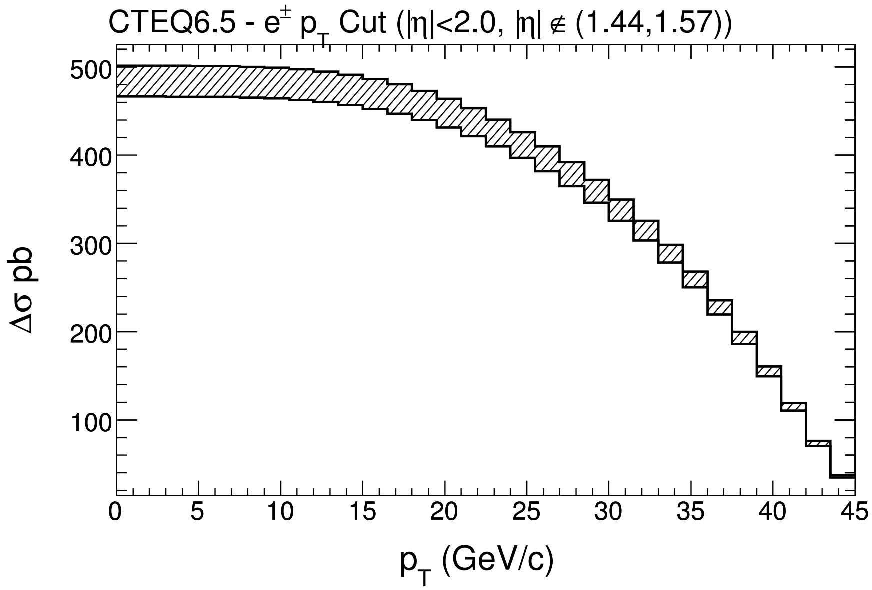

Figure 61: Error on the $Z/\gamma^* \rightarrow e^+e^-$ cross-section due to PDFs for different values of the electron p_T cut. The pseudorapidity cut for both electrons is fixed at $|\eta| < 2.0$ with $1.4442 < |\eta| < 1.560$ excluded, in the mass range $85 < M_{ee} < 95$ GeV/c^2.

[22] M. Dittmar, F. Pauss and D. Zurcher, Phys. Rev. D56, 7284-7290 (1997).

[23] S. Frixione and M.L. Mangano, JHEP 0405:056 (2004)

[24] T. Sjöstrand, L. Lönnblad and S. Mrenna, “PYTHIA 6.2: Physics and manual”, arXiv:hep-ph/0108264.

[25] S. Frixione and B.R. Webber, “The MC@NLO 3.2 Event Generator”, CERN-PH-TH/2006-012 (2006).

[26] HERWIG Home page: http://hepwww.rl.ac.uk/theory/seymour/herwig/, version 6.510 is used

[27] CTEQ pdfs: J. Pumplin *et al.*, JHEP 0207:012 and arXiv:hep-ph/0201195 (2002).

[28] MRST pdfs: R.S. Thorne *et al.*, Acta Phys.Polon. B33 (2002) 2927-2932 and arXiv:hep-ph/0207067 (2002)

[29] Les Houches Accord PDF Interface: http://hepforge.cedar.ac.uk/lhapdf

[30] RESBOS: C. Balazs, C.P. Yuan, Phys. Rev. D56 (1997) 5558-5583

[31] HORACE: C.M. Carloni Calame *et al.*, Phys.Rev. D69 (2004) 037301

[32] C. Anastasiou *et al.*, Phys.Rev. D69 (2004) 094008

[33] A.D. Martin *et al.*, Eur.Phys.J. C18 (2000) 117-126

[34] FEWZ K. Melnikov, F. Petriello Phys.Rev. D74 (2006) 114017

[35] MadGraph/MadEvent v4: The New Web Generation Johan Alwall, Pavel Demin, Simon de Visscher, Rikkert Frederix, Michel Herquet, Fabio Maltoni, Tilman Plehn, David L. Rainwater and Tim Stelzer JHEP 0709:028,2007, arXiv:0706.2334

MadEvent: Automatic event generation with MadGraph F. Maltoni and T. Stelzer, JHEP 0302:027, 2003 hep-ph/0208156 JHEP02(2003)027

[36] ”PHOTOS Monte Carlo: A Precision tool for QED corrections in Z and W decays.” Piotr Golonka, Zbigniew Was (CERN & Cracow, INP) . IFJPAN-V-05-01, CERN-PH-TH-2005-091, Jun 2005. 28pp. Published in Eur.Phys.J.C45:97-107,2006. e-Print: hep-ph/0506026

PHOTOS: A Universal Monte Carlo for QED radiative corrections. Version 2.0. Elisabetta Barberio (CERN & Siegen U.) , Zbigniew Was (CERN & Cracow, INP) . CERN-TH-7033-93, Oct 1993. 22pp. Published in Comput.Phys.Commun.79:291-308,1994.

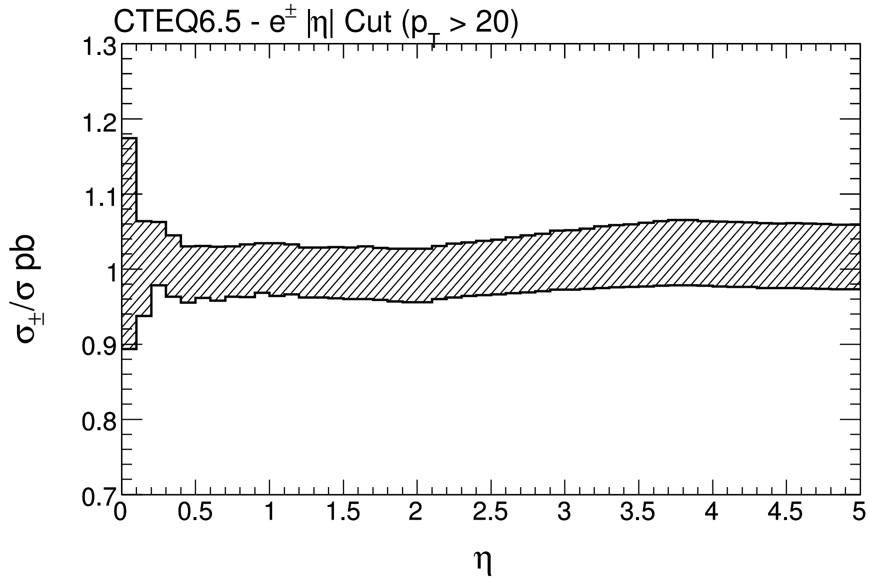

Figure 62: Fractional error on the $Z/\gamma^* \to e^+e^-$ cross-section due to PDFs for different values of the electron $|\eta|$ cut. The momentum cut for both electrons is fixed at $p_T > 20$ GeV/c in the mass range $85 < M_{ee} < 95$ GeV/c^2.

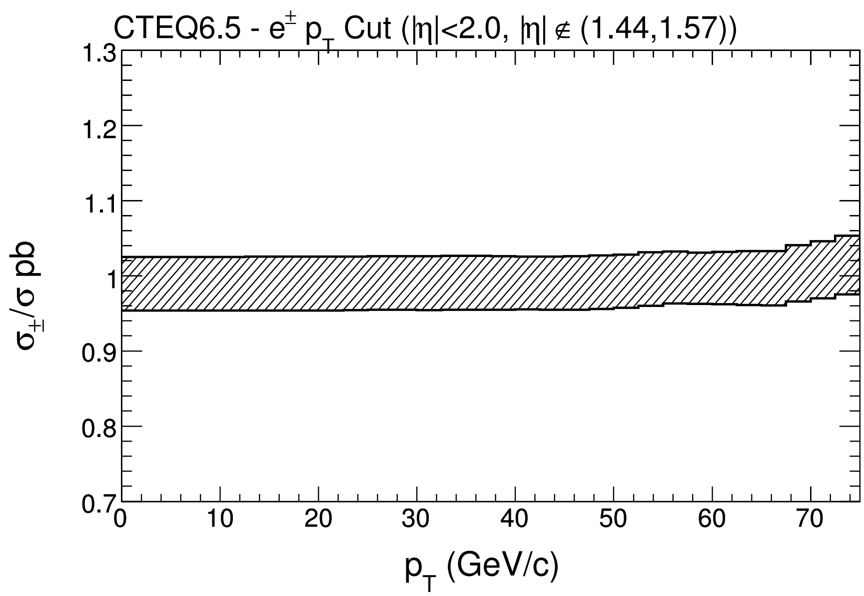

Figure 63: Fractional error on the $Z/\gamma^* \to e^+e^-$ cross-section due to PDFs for different values of the electron p_T cut. The pseudorapidity cut for both electrons is fixed at $|\eta| < 2.0$ with $1.4442 < |\eta| < 1.566$ excluded, in the mass range $85 < M_{ee} < 95$ GeV/c^2.

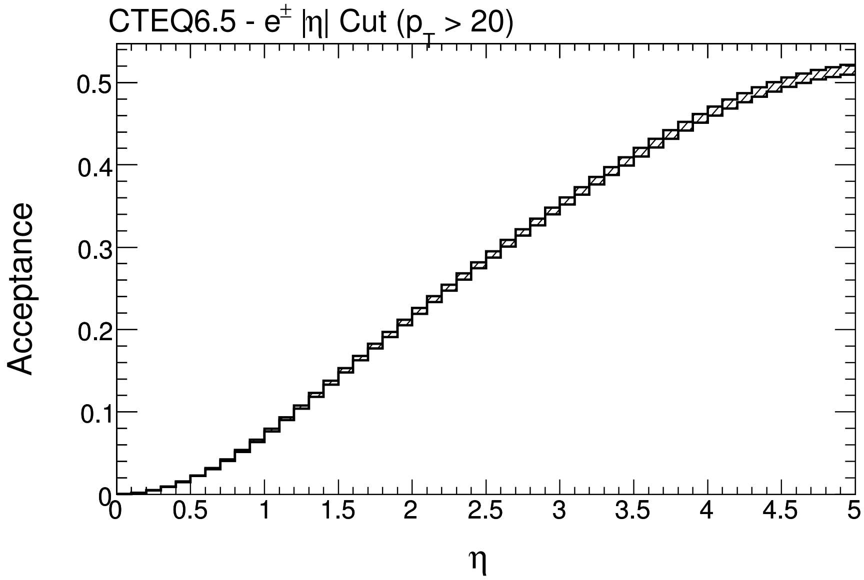

Figure 64: Error on the $Z/\gamma^* \to e^+e^-$ acceptance due to PDFs for different values of the electron $|\eta|$ cut. The momentum cut for both electrons is fixed at $p_T > 20$ GeV/c in the mass range $85 < M_{ee} < 95$ GeV/c^2.

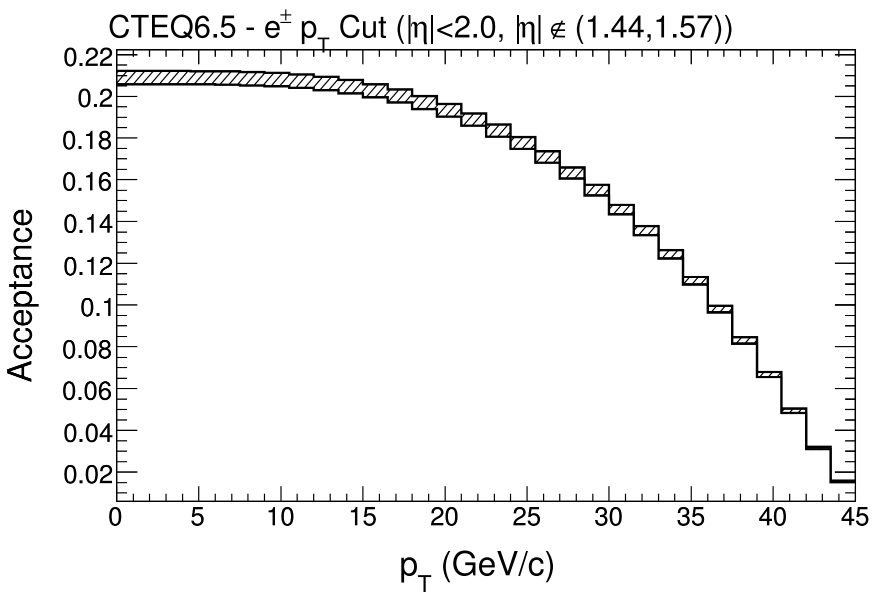

Figure 65: Error on the $Z/\gamma^* \to e^+e^-$ acceptance due to PDFs for different values of the electron p_T cut. The pseudorapidity cut for both electrons is fixed at $|\eta| < 2.0$ with $1.4442 < |\eta| < 1.566$ excluded, in the mass range $85 < M_{ee} < 95$ GeV/c^2.

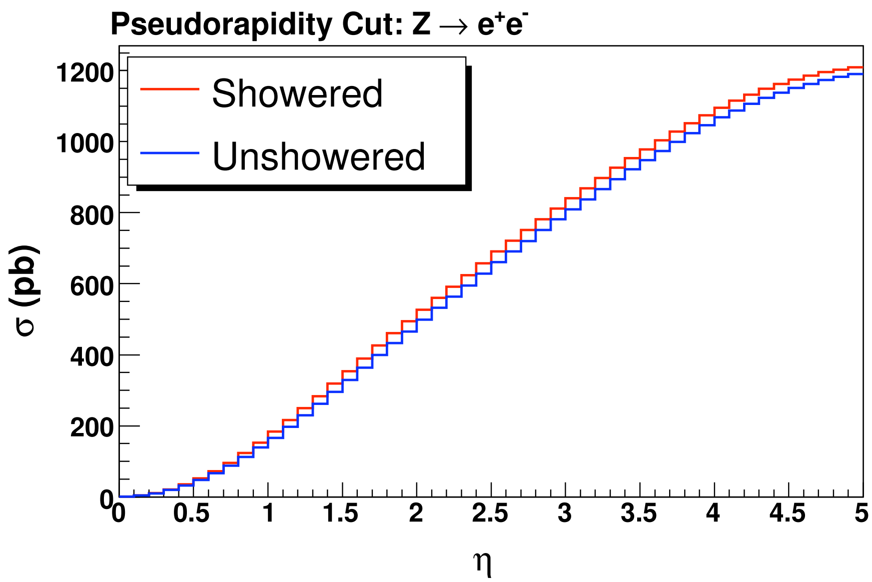

Figure 66: The $Z/\gamma^* \to e^+e^-$ cross-section at NLO for different values of the electron $|\eta|$ cut. The momentum cut for both electrons is fixed at $p_T > 20$ GeV/c in the mass range $85 < M_{ee} < 95$ GeV/c^2. The blue histogram gives the value before parton showering (with Herwig) and the red histogram gives the value after showering.

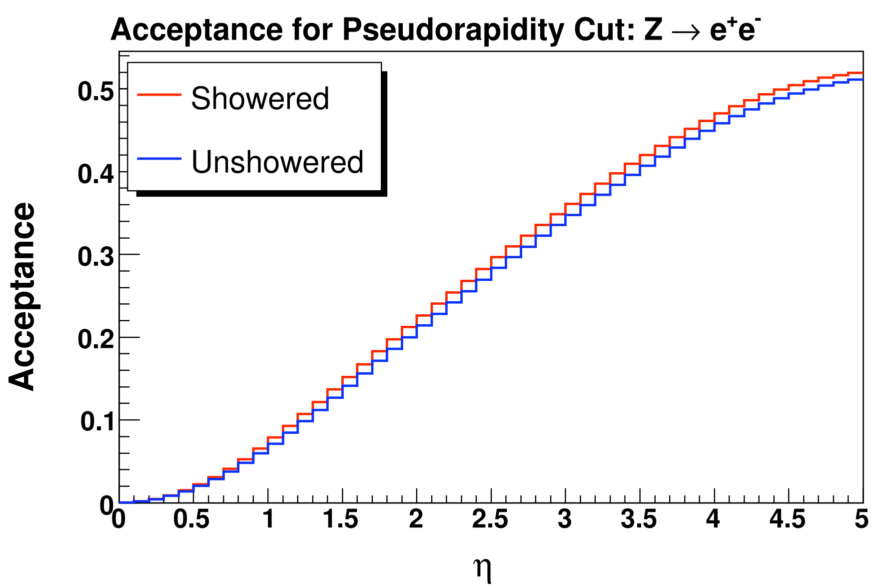

Figure 67: The $Z/\gamma^* \to e^+e^-$ acceptance (fraction of total cross-section above $M_{ee} = 40$ GeV/c^2 passing the cuts) at NLO for different values of the electron $|\eta|$ cut. The momentum cut for both electrons is fixed at $p_T > 20$ GeV/c in the mass range $85 < M_{ee} < 95$ GeV/c^2. The blue histogram gives the value before parton showering (with Herwig) and the red histogram gives the value after showering.

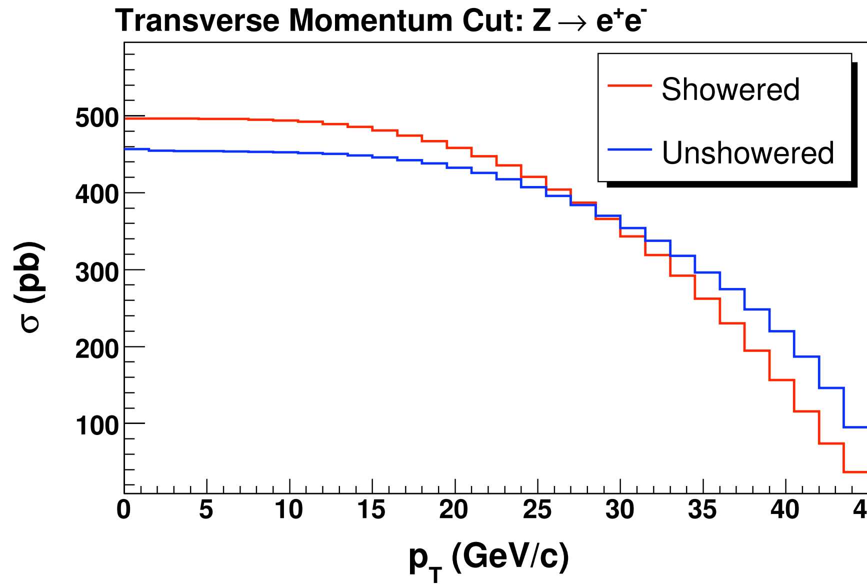

Figure 68: The $Z/\gamma^* \rightarrow e^+e^-$ cross-section at NLO for different values of the electron p_T cut. The pseudorapidity cut for both electrons is fixed at $|\eta| < 2.0$ with $1.4442 < |\eta| < 1.566$ excluded, in the mass range $85 < M_{ee} < 95$ GeV/c^2. The blue histogram gives the value before parton showering (with Herwig) and the red histogram gives the value after showering.

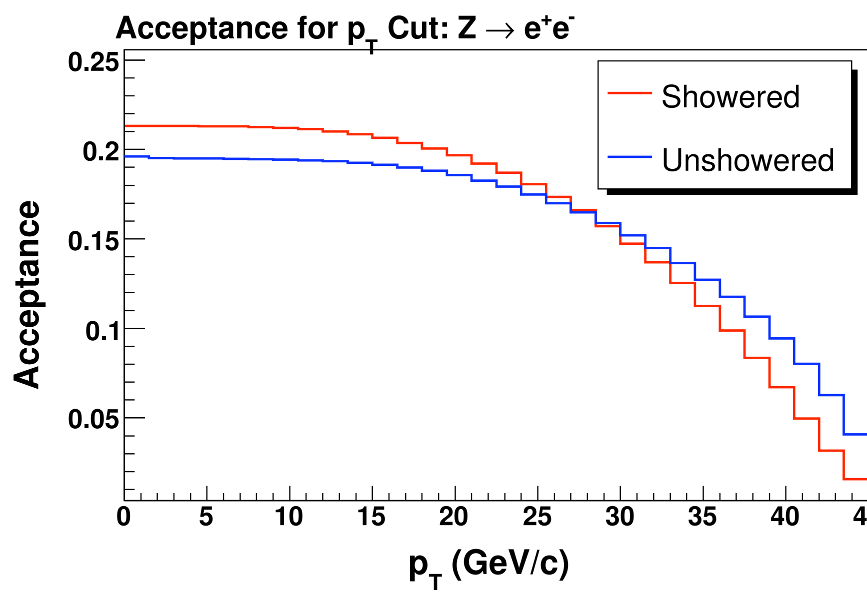

Figure 69: The $Z/\gamma^* \rightarrow e^+e^-$ acceptance (fraction of total cross-section above $M_{ee} = 40$ GeV/c^2 passing the cuts) at NLO for different values of the electron p_T cut. The pseudorapidity cut for both electrons is fixed at $|\eta| < 2.0$ with $1.4442 < |\eta| < 1.566$ excluded, in the mass range $85 < M_{ee} < 95$ GeV/c^2. The blue histogram gives the value before parton showering (with Herwig) and the red histogram gives the value after showering.

A $\mathrm{W} \to \mathrm{e}\nu$ Missing Transverse Energy Template from $\gamma^*/\mathrm{Z} \to \mathrm{e}^+\mathrm{e}^-$ Events.

As described in Section 9.2.1, the background to $\mathrm{W} \to \mathrm{e}\nu$ can be estimated using the "template" method, with $\not\!\!E_T$ as the discriminating variable. A preliminary study has been made of obtaining the $\not\!\!E_T$ template of $\mathrm{W} \to \mathrm{e}\nu$ from $\gamma^*/\mathrm{Z} \to \mathrm{e}^+\mathrm{e}^-$ events. $\gamma^*/\mathrm{Z} \to \mathrm{e}^+\mathrm{e}^-$ has a much lower background than $\mathrm{W} \to \mathrm{e}\nu$, but a cross-section that is approximately 10 times smaller. The kinematics of leptons from W and Z bosons are similar, but not identical, so corrections need to be made to account for this.

To obtain the $\mathrm{W} \to \mathrm{e}\nu$ $\not\!\!E_T$ template, we ensure that one of the electrons in the $\gamma^*/\mathrm{Z} \to \mathrm{e}^+\mathrm{e}^-$ events will satisfy the conditions imposed on the electron in the $\mathrm{W} \to \mathrm{e}\nu$ selection. The neutrino is then emulated by making the vector sum over the calorimeter towers, but excluding those within a cone of $\Delta R < 0.1$ around the second electron. The distribution of missing transverse energy obtained is shown in Figure 70.

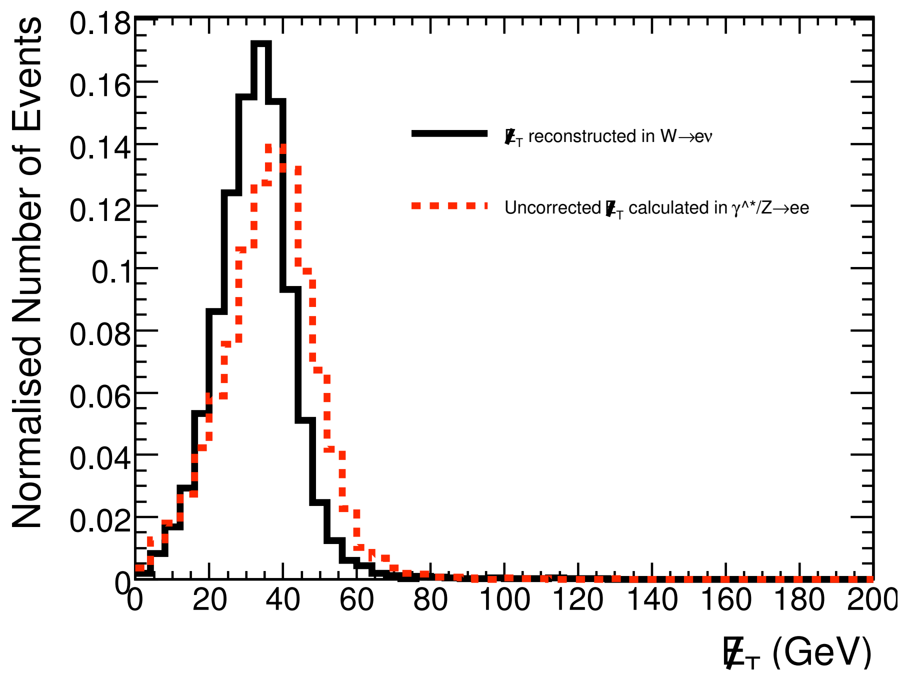

Figure 70: Missing transverse energy as reconstructed in $\mathrm{W} \to \mathrm{e}\nu$ (shown as solid black line), compared with the missing transverse energy calculated by excluding calorimeter towers within $\Delta R < 0.1$ of an electron in $\gamma^*/\mathrm{Z} \to \mathrm{e}^+\mathrm{e}^-$ (shown as dashed red line).

In order to account for the difference in kinematics between $\mathrm{W} \to \mathrm{e}\nu$ and $\gamma^*/\mathrm{Z} \to \mathrm{e}^+\mathrm{e}^-$ events, the transverse momentum of the γ^*/Z (calculated from the PixelMatchGsfElectrons) is subtracted from the 'ersatz' $\not\!\!E_T$, which is then scaled by M_W/M_Z before the γ^*/Z p_T is added back on. To correct for the different distribution of the leptons over the whole event sample, $\not\!\!E_T$ distributions are made for bins of electron p_T and η. Calculation of the $\not\!\!E_T$ distribution of $\mathrm{W} \to \mathrm{e}\nu$ events is then performed by sampling from the 'ersatz' $\not\!\!E_T$ distribution that corresponds to the electron p_T and η for each $\mathrm{W} \to \mathrm{e}\nu$ event.

The resulting missing transverse energy is shown in Figure 71 in red. It matches the $\not\!\!E_T$ that is actually reconstructed in the same $\mathrm{W} \to \mathrm{e}\nu$ events (shown in black) quite well. It should be noted that the number of $\gamma^*/\mathrm{Z} \to \mathrm{e}^+\mathrm{e}^-$ events used is equivalent to only $5pb^{-1}$ of integrated luminosity. It is expected that the correspondance would be enhanced with more data. Several improvements are foreseen, including a more sophisticated scheme for removing energy from $\gamma^*/\mathrm{Z} \to \mathrm{e}^+\mathrm{e}^-$ events to improve the missing energy emulation. Another improvement would be to remove energy using superclusters rather than electrons. This would remove inefficiencies caused by demanding electron reconstruction, as well as extend the η range of emulated neutrinos up to $|\eta| < 3$.

The effect of background on the determination of $\not\!\!E_T$ template of $\mathrm{W} \to \mathrm{e}\nu$ using this method has not been evaluated. While the $\gamma^*/\mathrm{Z} \to \mathrm{e}^+\mathrm{e}^-$ events will be relatively background free, the (p_T, η) distribution of single electrons passing the $\mathrm{W} \to \mathrm{e}\nu$ selection criteria is then used. This distribution will be contaminated by background events that might affect the $\not\!\!E_T$ template of $\mathrm{W} \to \mathrm{e}\nu$.

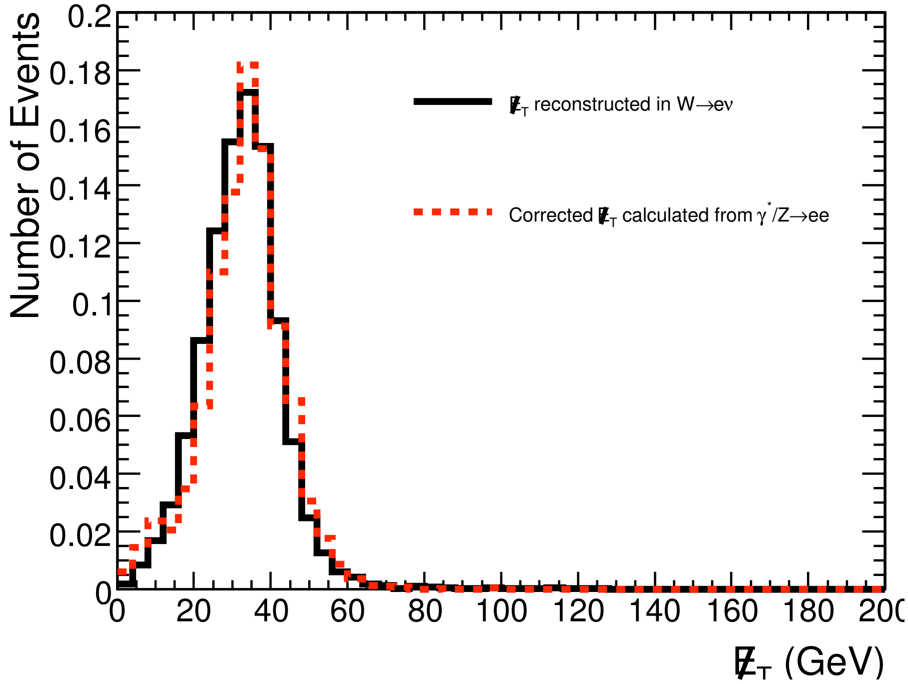

Figure 71: Missing transverse energy as reconstructed in $\mathrm{W} \rightarrow \mathrm{e}\nu$ (shown as solid black line), compared with the missing transverse energy calculated by excluding calorimeter towers within $\Delta R < 0.1$ of an electron in $\gamma^*/\mathrm{Z} \rightarrow \mathrm{e}^+\mathrm{e}^-$ (shown as dashed red line), after corrections for the kinematics of leptons from the decay.

B Same sign charge correlation in background samples.

In this section we report preliminary results from a study of the di-electron charge correlation found in important background channels like di-jets, Wjets and ttbar.

The two electrons used in the study are selected as follows: They are the two highest E_T PixelMatchGsfElectrons which

- fall inside the fiducial volume of the ECAL.
- have E_T >10.0 GeV

As shown in Figs. 72,73 the ratio of the opposite sign and same sign electron charges for the di-jet events is around 1.0 and doesn't depend on the $M_{e,e}$ of the two electrons.

For the Wjets events (Figs. 74,75) the ratio is around 1.4 showing significant correlation of the electron charges. This ratio is stable versus the $M_{e,e}$ of the two electrons.

Situation is different for the ttbar events (Figs. 76,77) in which the ratio increases as a function of the $M_{e,e}$ of the two electrons. This reflects the fact that heavier invariant masses correspond to more energetic electrons that have a higher probability to come from W $\rightarrow$ ev decays revealing thus a higher degree of correlation as the $M_{e,e}$ increases.

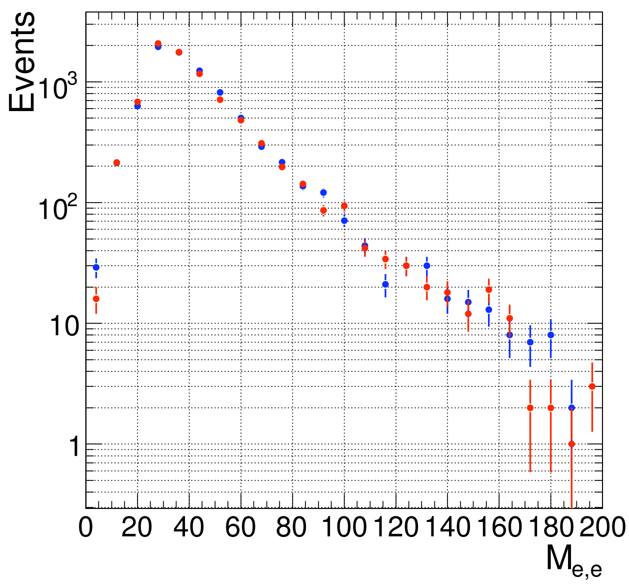

Figure 72: Distributions of $M_{e,e}$ for opposite sign charge electrons (blue dots) and same sign charge electrons (red dots) for the di-jet sample (50< $\hat{p}_t$ <80) listed in Table 1.

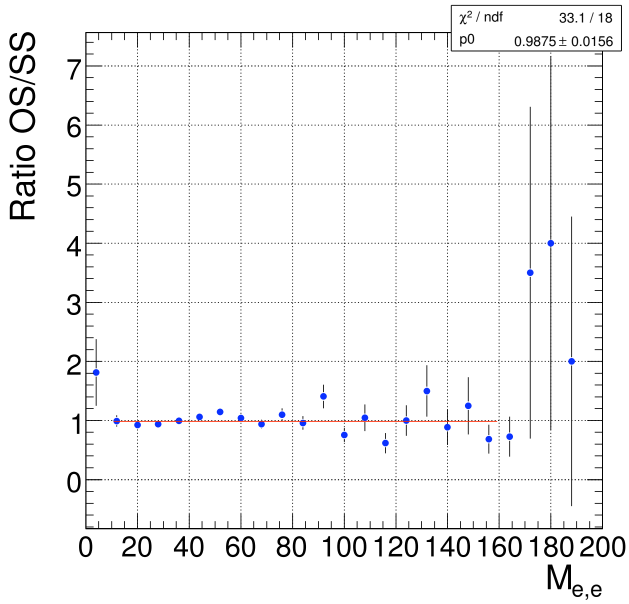

Figure 73: Ratio of the opposite sign charge electrons and same sign charge electrons versus their invariant mass ($M_{e,e}$) for the di-jet sample (50< $\hat{p}_t$ <80) listed in Table 1.

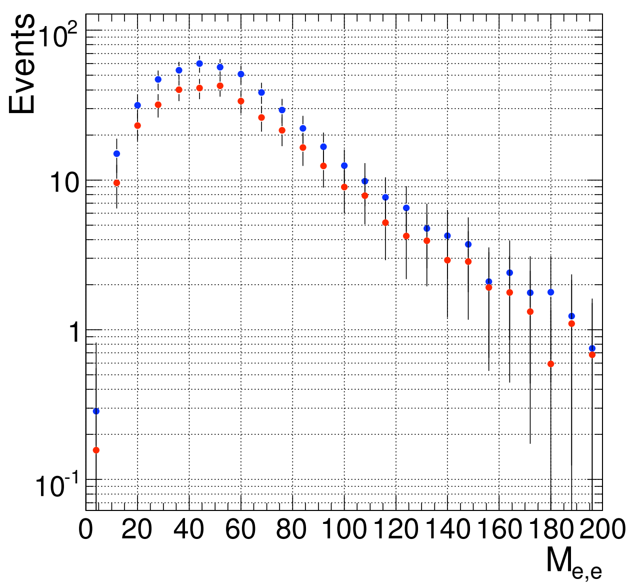

Figure 74: Distributions of $M_{e,e}$ for opposite sign charge electrons (blue dots) and same sign charge electrons (red dots) for the Wjets samples listed in Table 1.

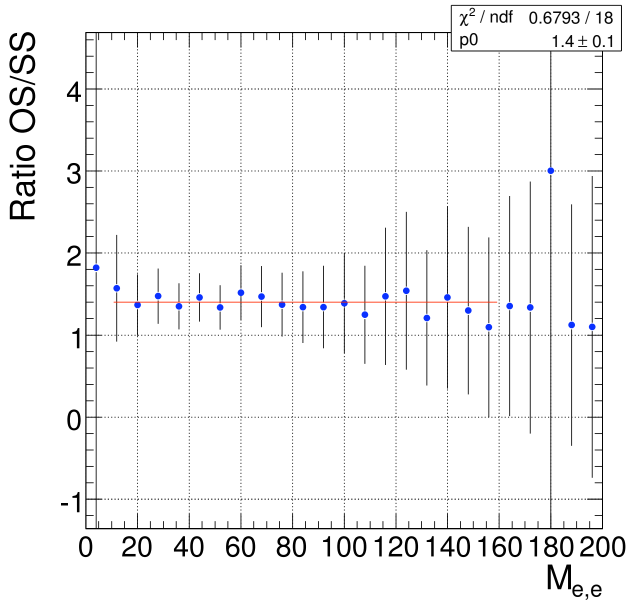

Figure 75: Ratio of the opposite sign charge electrons and same sign charge electrons versus their invariant mass ($M_{e,e}$) for the Wjets samples listed in Table 1.

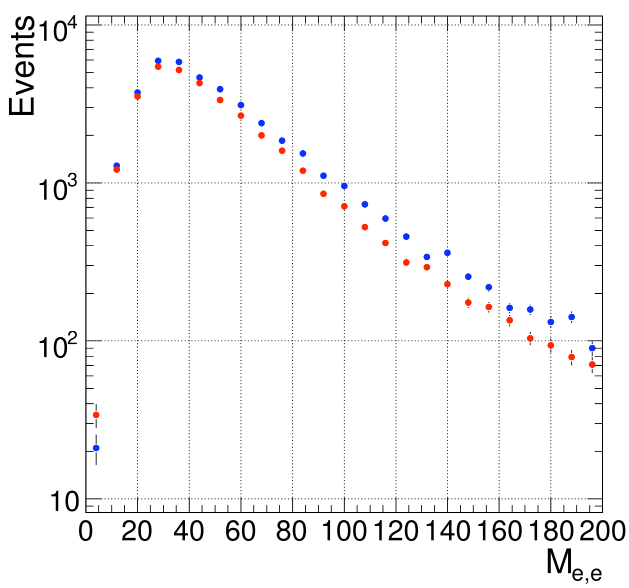

Figure 76: Distributions of $M_{e,e}$ for opposite sign charge electrons (blue dots) and same sign charge electrons (red dots) for the ttbar sample listed in Table 1.

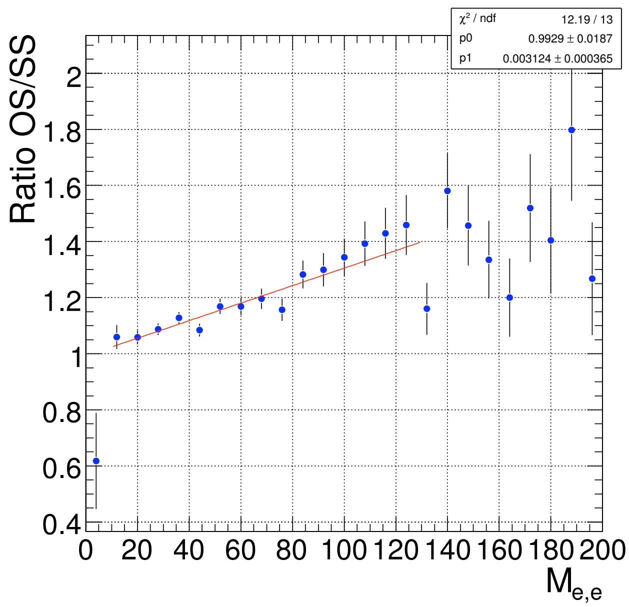

Figure 77: Ratio of the opposite sign charge electrons and same sign charge electrons versus their invariant mass ($M_{e,e}$) for the ttbar sample listed in Table 1.

C Correlated statistical uncertainty in the Z cross section measurement

In the case of $Z \to ee$, the samples used to estimate the signal yield are strongly overlapping, if not identical, to the samples used to determine efficiency. This introduces an anti-correlation between that signal yield and its efficiency, which violates the common assumption that they are uncorrelated statistically. This effect, and an estimate of its size can be demonstrated as follows.

Suppose the average efficiency is measured via a single-bin, single step, tag-and-probe method, where P events have both leptons passing the electron selection, and F events have only the tag electron passing. Suppose also, for simplicity, that the probe lepton selection and the single lepton trigger efficiencies are 100%. Then the mean electron selection efficiency ϵ is given by

$$\epsilon = \frac{2P}{2P+F},$$

and the signal yield is P. The cross section σ is given by

$$\begin{aligned}
\sigma &= \frac{N}{\int \mathcal{L} \cdot A \cdot \epsilon^2} \\
&= \frac{1}{\int \mathcal{L} \cdot A} \cdot \frac{P}{4P^2/(2P+F)^2} \\
&= \frac{1}{\int \mathcal{L} \cdot A} \cdot P(1+F/2P)^2
\end{aligned}$$

Assuming that P and F are uncorrelated Poisson statistics, standard error propagation applied to this formula gives

$$\delta\sigma^2_{corr} = \frac{1}{\int \mathcal{L}^2 \cdot A^2} \cdot P(1 + \frac{F}{P} + \frac{1}{2}(\frac{F}{P})^2 + \frac{1}{4}(\frac{F}{P})^3 + \frac{1}{16}(\frac{F}{P})^4)$$

Alternatively, if the correlation between N and ϵ is ignored, then

$$\begin{aligned}
\delta\sigma^2_{uncorr} &= \frac{1}{\int \mathcal{L}^2 \cdot A^2} \cdot (\frac{1}{\epsilon^4}N + \frac{4N^2}{\epsilon^6}\delta\epsilon^2) \\
&= \frac{1}{\int \mathcal{L}^2 \cdot A^2} \cdot (\frac{1}{\epsilon^4}N + \frac{4N^2}{\epsilon^6}\frac{4PF(P+F)}{(2P+F)^4}) \\
&= \frac{1}{\int \mathcal{L}^2 \cdot A^2} \cdot (\frac{P(2P+F)^4}{16P^4} + \frac{4P^2(2P+F)^6}{64P^6}\frac{4PF(P+F)}{(2P+F)^4}) \\
&= \frac{1}{\int \mathcal{L}^2 \cdot A^2} \cdot P(1 + 3\frac{F}{P} + \frac{7}{2}(\frac{F}{P})^2 + \frac{7}{4}(\frac{F}{P})^3 + \frac{5}{16}(\frac{F}{P})^4)
\end{aligned}$$

Clearly $\delta\sigma_{corr} < \delta\sigma_{uncorr}$, and the lower the lepton efficiency, the larger this difference becomes. If $P = 1000$ and $\epsilon = 0.9$, then $(\delta\sigma_{uncorr} - \delta\sigma_{corr})/\delta\sigma_{corr} = +22\%$; but if $\epsilon = 0.5$, this difference grows to an overestimate of +124%.

This correlation effect can be dealt with in at least four ways, which are described below.

Firstly, it can simply be ignored, in which case the cross section uncertainty is overestimated, but undercoverage is still avoided. This is a simple and conservative solution, but a non-optimal use of the statistics of the sample. If that statistical uncertainty is not the dominant factor in the total uncertainty (ignoring luminosity, this is probably true for $N \simeq 10^4$), it is of little consequence to ignore it.

Secondly, it could be computed analytically, by rewriting the cross section formula in terms of uncorrelated variables and recomputing the total uncertainty. This is simple enough for a one-step, single-bin efficiency measurement, but quickly becomes more complicated as more steps (and backgrounds) are introduced.

Thirdly, it could be computed numerically by including the signal yield estimation in a combined unbinned likelihood fit with the sample used for efficiency estimation.

Fourthly, it could be de-correlated by explicitly separating the data sample into two parts, one for the efficiency measurement and the other for the signal yield estimation. This is simple and correct, however it is a very non-optimal use of the available statistics.

D Efficiencies binned in η and E_T

In this section we give the two dimensional efficiencies in E_T and η parameter space. Each column represents a different bin in E_T while each line represents a different η bin.

Table 27: gsf electron efficiency results

	$0-10$	$10-20$	$20-30$	$30-40$	$40-50$	$50-60$	$60-70$	$70-80$	$80-90$	$90-100$
$0-0.3$	0^{1}_{0}	0^{1}_{0}	$0.92^{0.022}_{0.026}$	$0.95^{0.0097}_{0.011}$	$0.95^{0.0079}_{0.0088}$	$0.95^{0.016}_{0.019}$	$0.97^{0.017}_{0.026}$	$0.84^{0.063}_{0.08}$	$0.9^{0.068}_{0.12}$	$0.25^{0.21}_{0.15}$
$0.3-0.6$	0^{1}_{0}	0^{1}_{0}	$0.94^{0.017}_{0.021}$	$0.93^{0.012}_{0.013}$	$0.93^{0.01}_{0.011}$	$0.93^{0.019}_{0.022}$	$0.95^{0.026}_{0.037}$	$0.95^{0.042}_{0.065}$	$0.83^{0.086}_{0.12}$	$1^{0}_{0.13}$
$0.6-0.9$	0^{1}_{0}	0^{1}_{0}	$0.93^{0.019}_{0.023}$	$0.94^{0.016}_{0.0089}$	$0.94^{0.0092}_{0.01}$	$0.96^{0.014}_{0.018}$	$0.96^{0.021}_{0.034}$	$0.96^{0.028}_{0.055}$	$1^{0}_{0.099}$	$1^{0}_{0.21}$
$0.9-1.2$	0^{1}_{0}	0^{1}_{0}	$0.92^{0.019}_{0.023}$	$0.91^{0.012}_{0.013}$	$0.93^{0.011}_{0.012}$	$0.95^{0.016}_{0.021}$	$0.93^{0.032}_{0.046}$	$0.8^{0.14}_{0.11}$	$0.94^{0.044}_{0.081}$	$1^{0}_{0.25}$
$1.2-1.5$	0^{1}_{0}	0^{1}_{0}	$0.87^{0.025}_{0.028}$	$0.89^{0.016}_{0.017}$	$0.9^{0.016}_{0.018}$	$0.85^{0.035}_{0.04}$	$0.93^{0.04}_{0.061}$	$0.8^{0.086}_{0.11}$	$1^{0}_{0.12}$	$0.75^{0.15}_{0.21}$
$1.5-1.8$	0^{1}_{0}	0^{1}_{0}	$0.89^{0.022}_{0.025}$	$0.91^{0.016}_{0.018}$	$0.91^{0.016}_{0.018}$	$0.92^{0.025}_{0.031}$	$1^{0}_{0.065}$	$0.9^{0.068}_{0.12}$	$1^{0}_{0.32}$	$1^{0}_{0.25}$
$1.8-2.1$	0^{1}_{0}	0^{1}_{0}	$0.89^{0.021}_{0.023}$	$0.93^{0.013}_{0.015}$	$0.93^{0.014}_{0.016}$	$0.99^{0.0087}_{0.018}$	$0.86^{0.061}_{0.082}$	$0.88^{0.066}_{0.096}$	$1^{0}_{0.25}$	$0.5^{0.25}_{0.25}$
$2.1-2.4$	0^{1}_{0}	0^{1}_{0}	$0.8^{0.026}_{0.027}$	$0.8^{0.023}_{0.025}$	$0.83^{0.022}_{0.023}$	$0.84^{0.048}_{0.058}$	$0.86^{0.064}_{0.085}$	$0.88^{0.084}_{0.14}$	$0.83^{0.11}_{0.17}$	$1^{0}_{0.25}$
$2.4-2.7$	0^{1}_{0}	0^{1}_{0}	$0.63^{0.06}_{0.063}$	$0.64^{0.054}_{0.057}$	$0.71^{0.05}_{0.054}$	$0.72^{0.093}_{0.11}$	$0.64^{0.13}_{0.14}$	$0.8^{0.13}_{0.19}$	$0.5^{0.25}_{0.25}$	0^{1}_{0}
$2.7-3$	0^{1}_{0}	0^{1}_{0}	0^{1}_{0}	0^{1}_{0}	0^{1}_{0}	0^{1}_{0}	0^{1}_{0}	0^{1}_{0}	0^{1}_{0}	0^{1}_{0}

Table 28: isolation efficiency results

	$0-10$	$10-20$	$20-30$	$30-40$	$40-50$	$50-60$	$60-70$	$70-80$	$80-90$	$90-100$
$0-0.3$	0^{1}_{0}	0^{1}_{0}	$0.89^{0.026}_{0.03}$	$0.96^{0.009}_{0.01}$	$0.98^{0.0058}_{0.0068}$	$0.99^{0.0071}_{0.012}$	$0.98^{0.011}_{0.022}$	$1^{0}_{0.051}$	$1^{0}_{0.11}$	$1^{0}_{0.44}$
$0.3-0.6$	0^{1}_{0}	0^{1}_{0}	$0.88^{0.025}_{0.028}$	$0.96^{0.0094}_{0.011}$	$0.97^{0.0065}_{0.0077}$	$0.99^{0.005}_{0.01}$	$1^{0}_{0.021}$	$1^{0}_{0.059}$	$1^{0}_{0.099}$	$1^{0}_{0.13}$
$0.6-0.9$	0^{1}_{0}	0^{1}_{0}	$0.9^{0.023}_{0.027}$	$0.95^{0.01}_{0.012}$	$0.98^{0.0057}_{0.0069}$	$0.99^{0.0055}_{0.011}$	$0.98^{0.014}_{0.029}$	$1^{0}_{0.045}$	$1^{0}_{0.099}$	$1^{0}_{0.21}$
$0.9-1.2$	0^{1}_{0}	0^{1}_{0}	$0.89^{0.024}_{0.027}$	$0.95^{0.0093}_{0.011}$	$0.97^{0.0069}_{0.0084}$	$0.99^{0.0059}_{0.012}$	$1^{0}_{0.028}$	$0.88^{0.084}_{0.14}$	$1^{0}_{0.069}$	$1^{0}_{0.25}$
$1.2-1.5$	0^{1}_{0}	0^{1}_{0}	$0.88^{0.026}_{0.03}$	$0.94^{0.012}_{0.014}$	$0.98^{0.0075}_{0.0097}$	$0.97^{0.014}_{0.023}$	$1^{0}_{0.043}$	$1^{0}_{0.085}$	$1^{0}_{0.12}$	$1^{0}_{0.25}$
$1.5-1.8$	0^{1}_{0}	0^{1}_{0}	$0.88^{0.025}_{0.028}$	$0.94^{0.014}_{0.016}$	$0.97^{0.0094}_{0.012}$	$1^{0}_{0.013}$	$1^{0}_{0.065}$	$1^{0}_{0.11}$	$0.5^{0.25}_{0.25}$	$1^{0}_{0.25}$
$1.8-2.1$	0^{1}_{0}	0^{1}_{0}	$0.79^{0.029}_{0.031}$	$0.86^{0.019}_{0.021}$	$0.9^{0.017}_{0.019}$	$0.89^{0.031}_{0.038}$	$0.74^{0.089}_{0.1}$	$0.79^{0.092}_{0.12}$	$1^{0}_{0.25}$	$1^{0}_{0.44}$
$2.1-2.4$	0^{1}_{0}	0^{1}_{0}	$0.83^{0.027}_{0.029}$	$0.82^{0.024}_{0.026}$	$0.8^{0.026}_{0.028}$	$0.82^{0.056}_{0.067}$	$0.83^{0.073}_{0.097}$	$1^{0}_{0.13}$	$0.6^{0.18}_{0.2}$	$0.67^{0.19}_{0.24}$
$2.4-2.7$	0^{1}_{0}	0^{1}_{0}	$0.89^{0.043}_{0.056}$	$0.85^{0.046}_{0.056}$	$0.85^{0.044}_{0.053}$	$0.92^{0.053}_{0.096}$	$0.71^{0.14}_{0.17}$	$1^{0}_{0.21}$	$1^{0}_{0.44}$	0^{1}_{0}
$2.7-3$	0^{1}_{0}	0^{1}_{0}	0^{1}_{0}	0^{1}_{0}	0^{1}_{0}	0^{1}_{0}	0^{1}_{0}	0^{1}_{0}	0^{1}_{0}	0^{1}_{0}

Table 29: robust electron ID efficiency results

	$0-10$	$10-20$	$20-30$	$30-40$	$40-50$	$50-60$	$60-70$	$70-80$	$80-90$	$90-100$
$0-0.3$	0^{1}_{0}	0^{1}_{0}	$1^{0}_{0.01}$	$1^{0}_{0.0028}$	$0.99^{0.0029}_{0.004}$	$1^{0}_{0.0073}$	$1^{0}_{0.018}$	$1^{0}_{0.051}$	$1^{0}_{0.11}$	$1^{0}_{0.44}$
$0.3-0.6$	0^{1}_{0}	0^{1}_{0}	$0.99^{0.0055}_{0.011}$	$1^{0.0028}_{0.0046}$	$0.99^{0.0028}_{0.0041}$	$0.99^{0.0051}_{0.01}$	$1^{0}_{0.021}$	$1^{0}_{0.059}$	$1^{0}_{0.099}$	$1^{0}_{0.13}$
$0.6-0.9$	0^{1}_{0}	0^{1}_{0}	$1^{0}_{0.0089}$	$1^{0.0018}_{0.0037}$	$1^{0}_{0.0022}$	$1^{0}_{0.0086}$	$1^{0}_{0.023}$	$1^{0}_{0.045}$	$1^{0}_{0.099}$	$1^{0}_{0.21}$
$0.9-1.2$	0^{1}_{0}	0^{1}_{0}	$1^{0}_{0.0084}$	$1^{0.0017}_{0.0036}$	$1^{0}_{0.0027}$	$0.99^{0.0059}_{0.012}$	$1^{0}_{0.028}$	$1^{0}_{0.13}$	$1^{0}_{0.069}$	$1^{0}_{0.25}$
$1.2-1.5$	0^{1}_{0}	0^{1}_{0}	$1^{0}_{0.0095}$	$1^{0.0024}_{0.0049}$	$1^{0.0026}_{0.0053}$	$1^{0}_{0.015}$	$1^{0}_{0.043}$	$1^{0}_{0.085}$	$1^{0}_{0.12}$	$1^{0}_{0.25}$
$1.5-1.8$	0^{1}_{0}	0^{1}_{0}	$0.99^{0.0084}_{0.014}$	$1^{0}_{0.0047}$	$0.99^{0.0047}_{0.0076}$	$1^{0}_{0.013}$	$1^{0}_{0.065}$	$1^{0}_{0.11}$	$1^{0}_{0.44}$	$1^{0}_{0.25}$
$1.8-2.1$	0^{1}_{0}	0^{1}_{0}	$1^{0}_{0.008}$	$1^{0.0028}_{0.0058}$	$1^{0.003}_{0.006}$	$1^{0}_{0.015}$	$1^{0}_{0.074}$	$1^{0}_{0.091}$	$1^{0}_{0.25}$	$1^{0}_{0.44}$
$2.1-2.4$	0^{1}_{0}	0^{1}_{0}	$1^{0}_{0.0075}$	$1^{0}_{0.0062}$	$1^{0}_{0.0063}$	$1^{0}_{0.035}$	$1^{0}_{0.069}$	$1^{0}_{0.13}$	$1^{0}_{0.25}$	$1^{0}_{0.32}$
$2.4-2.7$	0^{1}_{0}	0^{1}_{0}	$1^{0}_{0.032}$	$0.97^{0.018}_{0.035}$	$1^{0}_{0.025}$	$1^{0}_{0.085}$	$1^{0}_{0.17}$	$1^{0}_{0.21}$	$1^{0}_{0.44}$	0^{1}_{0}
$2.7-3$	0^{1}_{0}	0^{1}_{0}	0^{1}_{0}	0^{1}_{0}	0^{1}_{0}	0^{1}_{0}	0^{1}_{0}	0^{1}_{0}	0^{1}_{0}	0^{1}_{0}

Table 30: trigger efficiency results

	$0-10$	$10-20$	$20-30$	$30-40$	$40-50$	$50-60$	$60-70$	$70-80$	$80-90$	$90-100$
$0-0.3$	0_{0}^{1}	0_{0}^{1}	$0.81_{0.039}^{0.035}$	$0.86_{0.018}^{0.017}$	$0.86_{0.015}^{0.014}$	$0.79_{0.033}^{0.031}$	$0.8_{0.053}^{0.047}$	$0.86_{0.085}^{0.064}$	$0.78_{0.15}^{0.11}$	0_{0}^{1}
$0.3-0.6$	0_{0}^{1}	0_{0}^{1}	$0.86_{0.032}^{0.028}$	$0.83_{0.019}^{0.018}$	$0.79_{0.018}^{0.017}$	$0.81_{0.034}^{0.031}$	$0.9_{0.046}^{0.036}$	$0.67_{0.11}^{0.1}$	$0.6_{0.15}^{0.14}$	$0.86_{0.15}^{0.094}$
$0.6-0.9$	0_{0}^{1}	0_{0}^{1}	$0.8_{0.037}^{0.034}$	$0.83_{0.019}^{0.018}$	$0.8_{0.018}^{0.017}$	$0.86_{0.032}^{0.029}$	$0.8_{0.061}^{0.053}$	$0.88_{0.076}^{0.056}$	$0.5_{0.14}^{0.14}$	$0.75_{0.21}^{0.15}$
$0.9-1.2$	0_{0}^{1}	0_{0}^{1}	$0.71_{0.04}^{0.038}$	$0.74_{0.022}^{0.021}$	$0.77_{0.021}^{0.02}$	$0.8_{0.038}^{0.035}$	$0.7_{0.074}^{0.068}$	$0.86_{0.15}^{0.094}$	$0.67_{0.12}^{0.11}$	$1_{0.25}^{0}$
$1.2-1.5$	0_{0}^{1}	0_{0}^{1}	$0.64_{0.044}^{0.043}$	$0.59_{0.028}^{0.028}$	$0.57_{0.03}^{0.029}$	$0.58_{0.057}^{0.055}$	$0.56_{0.097}^{0.094}$	$0.5_{0.13}^{0.13}$	$0.38_{0.14}^{0.16}$	$0.33_{0.19}^{0.24}$
$1.5-1.8$	0_{0}^{1}	0_{0}^{1}	$0.72_{0.04}^{0.038}$	$0.77_{0.028}^{0.026}$	$0.69_{0.03}^{0.029}$	$0.72_{0.05}^{0.047}$	$0.63_{0.12}^{0.11}$	$0.56_{0.15}^{0.15}$	$1_{0.44}^{0}$	$0.33_{0.19}^{0.24}$
$1.8-2.1$	0_{0}^{1}	0_{0}^{1}	$0.8_{0.035}^{0.032}$	$0.77_{0.027}^{0.026}$	$0.78_{0.027}^{0.025}$	$0.74_{0.053}^{0.049}$	$0.86_{0.11}^{0.074}$	$0.91_{0.11}^{0.062}$	$1_{0.25}^{0}$	$1_{0.44}^{0}$
$2.1-2.4$	0_{0}^{1}	0_{0}^{1}	$0.75_{0.036}^{0.034}$	$0.8_{0.031}^{0.029}$	$0.71_{0.02}^{0.062}$	$0.74_{0.051}^{0.14}$	$0.6_{0.12}^{0.12}$	$0.43_{0.16}^{0.17}$	$0.67_{0.24}^{0.19}$	$0.5_{0.25}^{0.25}$
$2.4-2.7$	0_{0}^{1}	0_{0}^{1}	$0.71_{0.08}^{0.072}$	$0.82_{0.066}^{0.055}$	$0.71_{0.069}^{0.063}$	$0.67_{0.13}^{0.12}$	$0.4_{0.18}^{0.19}$	$0.75_{0.21}^{0.15}$	0_{0}^{1}	0_{0}^{1}
$2.7-3$	0_{0}^{1}	0_{0}^{1}	0_{0}^{1}	0_{0}^{1}	0_{0}^{1}	0_{0}^{1}	0_{0}^{1}	0_{0}^{1}	0_{0}^{1}	0_{0}^{1}